UNIVERSITY OF CALIFORNIA,
IRVINE

Velocity-space resolved fast-ion measurements in the DIII-D tokamak

DISSERTATION

submitted in partial satisfaction of the requirements
for the degree of

DOCTOR OF PHILOSOPHY

in Physics

by

Christopher Michael Muscatello

Dissertation Committee:
Professor William W. Heidbrink, Chair
Professor Roger D. McWilliams
Professor Liu Chen

2012

DEDICATION

To

my parents and friends

for always believing in me

TABLE OF CONTENTS

LIST OF FIGURES

emission at 650nm is from OV. The smaller-amplitude line emission at 651.5nm is from CII. The thickness of the spectral curves denotes the error. The spectra are cutoff at lower wavelengths in the R=170cm and R=181cm channels due to the instrumental setup. The visible bremsstrahlung emission (VBE) is plotted in red and is relatively constant over the bandwidth presented.

Figure 1.11. a) Spectral response due to stray light within the s-FIDA system. The black curve is a true dark frame with the calibrated light sphere off. The red, green, and blue curves represent the response of a passive channel to the illumination of the remaining 5 channels (for luminance values of 100ftL, 200ftL, and 300ftL, respectively). b) Wavelength-integrated response of the passive channel (light leakage) to the wavelength-integrated signal on the illuminated channels (total illumination).

Figure 1.12. Sensitivity of FIDAsim spectra on toroidally-displaced chord separation for shot 146088. Spectra in blue use the design value of 10cm separation at the midplane between the central-most chord and each of adjacent chords on either side. Spectra in black use a hypothetical separation of 5cm.

Figure 1.13. Effect on the spectra due to finite spot correction. Spectra are presented for 9 different major radii at the midplane. The blue curves are uncorrected spectra from the FIDAsim code. Green dashed curves are spectra corrected for a 4cm diameter spot size. Orange spectra are corrected considering an 8cm diameter spot size.

Figure 1.14. Charge-exchange Dα emissivity profile in the midplane (Z=0). X axis is parallel to the axis of the neutral beam. Y axis is horizontal transverse axis. Green diamonds are intersections of oblique sightlines with the midplane. Chords at equivalent radii are along diagonals; for example, the 3 spots connected by the diagonal line comprise the R=191cm radial channel. Linear color scale is proportional to the emissivity.

Figure 1.15. Modifications to the spectra due to instrumental broadening. The original FIDA spectrum predicted by the FIDAsim code is in blue. The spectra including $\sigma = 0.3$nm Gaussian instrument function (dashed green) is virtually indistinguishable from the original spectra. Spectra with $\sigma = 1.0$nm Gaussian instrument function (orange) shows significant broadening compared to the original spectrum.

Figure 1.16. Volume-averaged beam-ion distribution function for shot 146088 at t=1385ms. Linear color scale indicates number of beam ions.

Figure 1.17. Comparison of FIDAsim spectra and measurements from the oblique system. Simulated spectra are solid orange. Dashed orange spectra are simulated spectra normalized to experimental spectra (in black with error bars) to show the excellent shape agreement. The bump in the experimental spectrum at 650nm for the R=223cm channel is a result of imperfect subtraction of the oxygen-V impurity line.

Figure 1.18. Comparison of predicted and measured FIDA emission spatial profiles from the oblique system. Simulated profile post-processed to include finite spot size and instrumental broadening is in orange. Unprocessed simulated profile is dashed. Measured data (with error

LIST OF TABLES

LIST OF SYMBOLS

D – deuterium
v or v – velocity
$v_{\|}$ – component of fast-ion velocity parallel to the magnetic field
$v_{\perp}$ – component of fast-ion velocity perpendicular to the magnetic field
v_{rot} – plasma toroidal rotation velocity
B – total magnetic field
Bt – toroidal magnetic field
Bo – magnetic field at the magnetic axis
n_f – fast-ion density
n_0, n_n – neutral density
n_e – electron density
n_{imp} – impurity density
n_c – carbon impurity density
σ – atomic cross-section; spectral resolution; standard deviation
n – atomic excitation level (chapter 1); toroidal mode number (elsewhere)
P_ζ – toroidal canonical momentum
ψ – poloidal flux function
F – poloidal current function
Ωi – ion cyclotron frequency
m – poloidal mode number
M – mass
e – electric charge
q – safety factor
Φ – scalar potential
E – total fast-ion energy; electric field
E_{crit} – critical energy for flux attachment (redistribution boundary)
μ – magnetic moment
χ – cosine of the pitch angle ($v_{\|}/v$)
R – major radius (variable)
R_{axis} – major radius of magnetic axis
r – minor radius (variable)
a – minor radius of the plasma (constant)
z – vertical elevation from midplane
Ip – plasma current
t – time
Te – electron temperature
Ti – ion temperature
λ – wavelength
λo – Dα wavelength (656.1nm)
$\Delta\lambda = |\lambda - \lambda o|$ – measured Doppler shift
E_λ – energy associated with measured Doppler shift

ρ – square root of normalized toroidal flux; Larmor radius
β – plasma beta
σ_a – standard deviation of active FIDA signal
σ_t – standard deviation of active + passive (total) signal
σ_p – standard deviation of passive signal
f – distribution function (chapter 1); fractional change (chapter 2)
$\Lambda = \mu B_o / E$ – constant-of-motion pitch parameter
Δr_b – orbit width
r_{mix} – sawtooth mixing radius
ω – mode angular frequency
f – mode frequency ($2\pi f = \omega$)
k – wavevector
ω_{pr} – toroidal precession frequency
ω_b – trapped (passing) bounce (poloidal transit) frequency
φ – third adiabatic invariant
τ_{pr} – toroidal precession period
τ_Ψ – period around perturbed flux surface
τ_{cr} – crash duration
ζ – toroidal angular coordinate
θ – poloidal angular coordinate
H – Hamiltonian
P_T – canonical momentum variable
X – canonical spatial variable

ACKNOWLEDGMENTS

I owe my gratitude to a number of people who have made this thesis possible. First and foremost, my graduate adviser and dissertation committee chair W.W. Heidbrink deserves the biggest thanks. His encouragement and support in both professional and personal aspects of my life made him an extremely valuable teacher and mentor.

Much of the knowledge I gained in the early stages of my thesis regarding FIDA and DIII-D is thanks to Y. Luo and D. Liu.

Installing a new diagnostic on DIII-D was a challenging process, from both a technical and organizational standpoint. The success of its implementation is due to the tireless efforts of many DIII-D scientists, engineers, and staff: D. Ayala , R. Boivin, K.H. Burrell, W. Carrig, S. Celle, J. Chavez, D. Kaplan, J. Kulchar, N.A. Pablant, M. Podesta, D. Taussig.

Data analysis, experimental planning, and collaborative work were major aspects of this thesis, and I am indebted to all of my colleagues: R.K. Fisher, R.W. Harvey, Y.I. Kolesnichenko, R.J. La Haye, E.A. Lazarus, V.V. Lutsenko, D.C. Pace, C.C. Petty, E. Ruskov, A.D. Turnbull, M.A. Van Zeeland, Y.V. Yakovenko, Y. Zhu.

Finally, I would like to extend my appreciation to my dissertation committee, R. McWilliams and L. Chen, for their instructive feedback on this work.

CURRICULUM VITAE

Christopher Michael Muscatello

EDUCATION

2012 Ph.D. in Physics, University of California, Irvine

2008 M.S. in Physics, University of California, Irvine

2006 B.A. in Physics, Case Western Reserve University

PUBLICATIONS

Measurements of fast-ion transport by mode-particle resonances on DIII-D (invited), Muscatello C.M., Grierson B.A., Harvey R.W., Heidbrink, W.W., Pace D.C., Van Zeeland M.A. (submitted to Nucl. Fusion).

Velocity-space studies of fast-ion transport at a sawtooth crash in neutral-beam heated plasmas, Muscatello C.M., Heidbrink W.W., Kolesnichenko Ya.I., Lutsenko V.V., Van Zeeland M.A., Yakovenko Yu.V., Plasma Phys. Control. Fusion **54**, 025006 (2012).

Extended fast-ion D-alpha diagnostic on DIII-D, Muscatello C.M., Heidbrink W.W., Taussig D., Burrell K.H., Rev. Sci. Instrum. **81**, 10D316 (2010).

Characterization of off-axis fishbones, Heidbrink W.W., Austin M.E., Fisher R.K., Garcia-Munoz M., Matsunaga G., McKee G.R., Moyer R.A., Muscatello C.M., Okabayashi M., Pace D.C., Shinohara K., Solomon W.M., Strait E.J., Van Zeeland M.A., Zhu Y., Plasma Phys. Control. Fusion **53,** 085028 (2011).

Transport of energetic ions due to sawteeth, Alfvén eigenmodes and microturbulence, Pace D.C., Fisher R.K., García-Muňoz M., Heidbrink W.W., McKee G.R., Murakami M., Muscatello C.M., Nazikian R.., Park J.M., Petty C.C., Rhodes T.L., Staebler G.M., Van Zeeland M.A., Waltz R.E., White R.B., Yu J.H., Zhu Y.B., Nucl. Fusion **51,** 043012 (2011).

On the application of electron cyclotron emission imaging to the validation of theoretical models of magnetohydrodynamic activity, Tobias B.J., Boivin R.L., Boom J.E., Classen I.G.J., Domier C.W., Donné A.J.H., Heidbrink W.W., Luhmann N.C., Munsat T., Muscatello C.M., Nazikian R., Park H.K., Spong D.A., Turnbull A.D., Van Zeeland M.A., Yun G.S., Phys. Plasmas **18,** 056107 (2011).

Modeling the response of a fast ion loss detector using orbit tracing techniques in a neutral beam prompt-loss study on the DIII-D tokamak, Pace D. C., Fisher R. K., Garcia-Munoz M., Darrow D. S., Heidbrink W. W., Muscatello C. M., Nazikian R., Van Zeeland M. A., Zhu Y. B.,

Rev. Sci. Instrum. **81**, 10D305 (2010).

Scintillator-based diagnostic for fast ion loss measurements on DIII-D, Fisher R. K., Pace D. C., Garcia-Munoz M., Heidbrink W. W., Muscatello C. M., Van Zeeland M. A., Zhu Y. B., Rev. Sci. Instrum. **81**, 10D307 (2010).

Imaging key aspects of fast ion physics in the DIII-D tokamak, Van Zeeland M. A., Yu J. H., Heidbrink W. W., Brooks N. H., Burrell K. H., Chu M. S., Hyatt A. W., Muscatello C.M., Nazikian R., Pablant N. A., Nucl. Fusion, **50**, 084002 (2010).

Central flattening of the fast-ion profile in reversed-shear DIII-D discharges, Heidbrink W. W., Van Zeeland M. A., Austin M. E., Burrell K. H., Gorelenkov N. N., Kramer G. J., Luo Y., Makowski M. A., McKee G. R., Muscatello C.M., Nazikian R., Ruskov E., Solomon W.M., White R.B., Zhu Y., Nucl. Fusion, 48, 084001 (2008).

A new fast-ion D-alpha diagnostic for DIII-D, Heidbrink W. W., Luo Y., Muscatello C. M., Zhu Y., Burrell K. H., Rev. Sci. Instrum. **79**, 10E520 (2008).

ABSTRACT OF THE DISSERTATION

Velocity-space resolved fast-ion measurements in the DIII-D tokamak

By

Christopher Michael Muscatello

Doctor of Philosophy in Physics

University of California, Irvine, 2012

Professor William W. Heidbrink, Chair

Superthermal ions in tokamak plasmas play a critical role in heating and current drive, and their confinement within the core of the plasma is crucial for obtaining ignition and sustaining burn in future reactors. At the DIII-D tokamak, a suite of fast-ion measurements is available to diagnose various properties of the superthermal population. This thesis work involves a contribution to DIII-D's fast-ion diagnostic collection: the 2nd generation fast-ion deuterium alpha (2G FIDA) detector. FIDA works on the principle of measuring the light that is emitted from neutralized fast ions that undergo charge exchange events with injected neutral atoms. 2G FIDA complements the other FIDA installations on DIII-D with its unique velocity-space sampling volume. Output from a synthetic diagnostic code (FIDAsim) that predicts FIDA emission levels is compared with measurements from 2G FIDA. We find that, while the predicted and measured shapes of the FIDA spectra agree well, the absolute magnitude of the spectral amplitudes are inconsistent. Results from various FIDAsim trials are presented adjusting several parameters, and it is hypothesized that mischaracterization of the diagnostic neutral beams is a major source of error. Instabilities in tokamaks can cause fast-ion transport. The sawtooth instability is

particularly important because the crash phase has been observed to cause reductions up to 50% in the central fast-ion density. Passing ions of all energies are redistributed, but only low energy trapped ions suffer redistribution. The observations are consistent with transport by flux-attachment. Comparisons with theory suggest that the intensity of sawtooth-induced transport depends on the magnitude of toroidal drift. Instabilities characterized by toroidal and poloidal mode numbers and real frequency can coherently interact with energetic particles through mode-particle resonances. During a sawtooth crash, even fast ions whose energies are above the threshold for flux-attachment can experience transport if their orbits satisfy the bounce-precessional resonance condition. On DIII-D, a spatially localized population of beam ions accelerated above the injection energy by ion-cyclotron radio frequency (ICRF) heating is diminished at a sawtooth crash. Furthermore, fast-ion losses concurrent with sawtooth crashes are observed. Calculations show that mode-particle resonances could be responsible. Transport of energetic particles by resonant interactions pertains to many types of instabilities; other examples besides sawteeth will also be presented. Analysis shows that large amplitude modes cause significant resonant transport of fast particles. Even small amplitude modes can resonantly drive transport if multiple harmonics exist.

PREFACE

To meet the world's energy demand, smart, clean, and efficient power sources must be harnessed. Energy sources alternative to fossil fuels and nuclear fission that are suitable for delivering power to the grid are particularly challenging. Envisaged alternatives (such as solar power, wind power, and nuclear fusion) are challenged with low net energy yield; many research and development efforts are focusing on scientific and engineering issues related to increasing energy production. Nuclear fusion is a process that has very promising implications but has proven to be difficult to control terrestrially.

One such scheme is controlled fusion by magnetic confinement, whereby strong magnetic fields are used to contain a hot plasma inside a toroidal device called a tokamak. Tokamaks are externally equipped with conductive coils that generate toroidal (azimuthal) and poloidal (polar) magnetic fields. The ultimate goal is to confine the hot plasma in an equilibrium state and extract the energy generated through fusion reactions (mainly through the released neutrons). However issues range from complications generating steady-state plasmas, to controlling particle and energy transport, to sufficiently heating the plasma. The interested reader is referred to ref. [1] for a comprehensive treatment of tokamaks and their current research challenges. Current envisaged heating schemes include neutral-beam injection (NBI) and launching waves at radio frequencies (RF). The NBI method involves directly injecting high-energy neutral atoms into the plasma. The neutrals ionize upon entry into the plasma and become confined within the magnetic fields. The high-energy ions transfer their energy to the plasma, heating it mainly through collisions with electrons. Waves launched at RF can resonate with harmonics of charged-particles' gyro-motion. Ion-cyclotron resonance heating (ICRH) involves launching RF waves

with the frequency (or integer multiples) of the ion cyclotron frequency. Ions can resonate with the wave and gain energy, subsequently transferring their energy to the bulk plasma through collisions.

In both cases (NBI and ICRH), a non-Maxwellian distribution of superthermal ions is generated. These fast ions must be confined within the plasma long enough to undergo a sufficient number of collisions with the thermal particles. If redistribution or loss of a significant fraction of the energetic-ion population takes place, heating efficiency is compromised. Transport of fast ions can be caused, for instance, by plasma instabilities or externally imposed magnetic perturbations which can lead to asymmetries in the magnetic fields and can break adiabatic invariants. One major area of active research toward the success of magnetically-confined fusion is the study of energetic-ion interactions with magnetohydrodynamic (MHD) instabilities. To accomplish this, instruments to measure the fast-ion population must be implemented.

At the DIII-D tokamak, a diverse suite of diagnostics are available, including an extensive collection of fast-ion measurements. One such measurement technique (fast-ion deuterium-alpha or FIDA) involves the detection of photons emitted from re-neutralized energetic ions undergoing charge-exchange as they pass through a neutral beam. The light collected is spectroscopically analyzed to infer the energy and spatial distribution of the fast ions. A single FIDA optical installation is typically comprised of several viewing chords which all intersect the magnetic field lines with roughly the same angle. The FIDA diagnostic is sensitive to a well-defined region of velocity space, determined in part by the geometry of its sightlines. Thus the availability of multiple optical installations with different sightline geometries provide different coverage in velocity space, allowing for discrimination of various orbit types.

Energetic-ion populations are not typically distributed isotropically in energy and pitch angle, so a diagnostic that can distinguish different regions of velocity space is a useful tool. The details and capabilities of FIDA (with emphasis on the 2nd generation 2009 installation) are found in chapter 1 of this thesis.

FIDA measurements are best utilized to measure the confined energetic deuterium population. Many classes of instabilities can detrimentally affect the core confined population of fast ions, redistributing a significant fraction and effectively reducing their heating efficiency. One such instability, which has been a topic of investigation for several decades, is the sawtooth which causes a rearrangement of the internal current profile and magnetic structure of the plasma. The effect is often observed as a sharp drop in the core electron temperature followed by a slow recovery. The sharp crashes in the electron temperature typically happen periodically, hence the instability's name. Not long after the discovery of the instability, measurements of fast-ion transport during sawtooth crash events were observed. Since then, virtually every major tokamak capable of detecting superthermal ions has made similar observations during sawteeth. Earlier investigations proposed that transport of fast ions at the sawtooth crash depends upon the characteristics of the orbit. In chapter 2, data from sawtooth experiments on the DIII-D tokamak is presented, and FIDA data is consistent with the theoretical prediction that transport during the crash is driven by particles attached to the evolving magnetic flux surfaces. The degree of transport, however, depends on the velocity-space parameters characterizing an orbit.

Many instabilities are characterized by a toroidal mode number (n) and can *resonantly* drive fast-ion transport. For low-frequency (~1kHz) low-n modes (e.g. sawtooth internal kink), resonances between the drift and bounce motions of a particle can lead to broadened orbits. For medium-frequency (~20kHz) low-n modes (e.g. fishbones), resonances between the mode

frequency and drift frequency can cause secular motion in a particle's orbit. The mode amplitude of a fishbone can be as much as 1% of the equilibrium field leading to large kicks in a resonant particle's orbit. The presence of high-frequency waves, such as Alfvén eigenmodes (AEs), introduces various possible resonances between drift and bounce motions and the mode frequency. Typically, the perturbation amplitude of AEs are much less than 1% of the equilibrium field, so interactions with individual resonances minimally effect a particle's orbit. However, where high concentrations of resonances exist, particles can encounter multiple kicks, collectively leading to significant secular orbit modifications and strong radial transport. In chapter 3, the interactions between instabilities and fast ions through mode-particle resonances will be discussed using scenarios from DIII-D.

CHAPTER 1. Introduction to fast-ion diagnostics and the fast-ion deuterium-alpha (FIDA) technique

Section 1.1. Survey of various fast-ion diagnostic techniques

To achieve burning plasmas in future tokamak reactors, substantial heating power will be required. Neutral beam injection and wave heating at radio frequencies are the two most promising methods. Both mechanisms often produce an anisotropic non-Maxwellian superthermal ion population. The heating efficiency is strongly dependent on how well the energetic ion population deposits its energy to the core bulk plasma. Plasma instabilities and externally imposed magnetic perturbations can lead to a redistribution or loss of fast ions, thereby impairing heating efficiency in the core. Furthermore, an intense population of energetic particles can provide the driving mechanism for some instabilities, which in turn can modify the fast-ion distribution function. Therefore, the need for careful diagnosis of the fast-ion distribution function becomes ever more important as we approach reactor-relevant scenarios.

Perhaps the most traditional method by which to measure energetic-ion populations in tokamaks is by detection of fusion products. Through the measurement of fusion products, one can make inferences about the fusion reactants. The fuels most commonly employed in tokamak experiments are deuterium (D) or a deutrium-tritium (DT) mixture . The corresponding fusion reactions are

$$D + D \rightarrow T\ (1.01MeV) + p(3.02MeV) \quad (1.1a)$$

$$D + D \rightarrow {}^{3}He(0.82MeV) + n(2.45MeV) \quad (1.1b)$$

$$D + T \rightarrow {}^{4}He\ (3.5MeV) + n\ (14.1MeV) \quad (1.2)$$

where the 2 branches of the DD reaction occur nearly equally. It is standard to distinguish among three different types of fusion reactions [2]: thermonuclear (thermal reactants), beam-target (energetic and thermal reactants), and beam-beam (energetic reactants). The fusion product emissivity s depends on the product of the density of the two reactants $n_1 n_2$ and the reactivity $\langle \sigma v \rangle$ (where v is the relative velocity between the reactants, σ is the cross-section for the fusion reaction, and the brackets indicate averaging over the distribution functions),

$$s \sim \langle \sigma v \rangle n_1 n_2 \quad (1.3)$$

In the presence of a significant beam-ion (energetic-ion) population, the total emissivity is typically dominated by beam-target or beam-beam reactions. The reason is that the probability for DT and DD fusion reactions peaks for high energies. If indeed beam-target or beam-beam reactions dominate, then reasonable inferences about the distribution of the energetic-ion population can be made based on the behavior of the detected fusion products.

Another common fast-ion measurement in tokamaks is achieved through the charge-exchange process. This process involves the exchange of electrons between ions and neutrals in

the plasma. The so-called *passive* measurement relies on charge-exchange between fast ions and the naturally existing neutrals. *Active* measurements require neutral beam injection (NBI), and fast ions that intersect the neutral beam can undergo a charge-exchange reaction with an injected neutral. The naturally existing neutral density is largest near the edge of the plasma and drops quickly inside the plasma. Conversely, the fast-ion density typically peaks near the axis. Since tokamak plasmas are optically thin, a collimated measurement integrates signal along its entire line-of-sight. A passive measurement is therefore dominated by charge-exchange reactions at the edges of the plasma. An active measurement, in addition to the passive signal, includes the contribution from the neutral beam. If the width of the collimated sightline is small compared to the width of the injected neutral beam, an active signal provides a core-localized (at the intersection of the sightline and neutral beam) measurement. Either passive or active, the probability for a charge-exchange reaction takes the same form as the probability for fusion reactivity (eq. 1.3), where $n_1 n_2$ is replaced by the product of the neutral density and the fast-ion density $n_0 n_f$. The factor that differentiates the two physical phenomena is the cross-section, σ. In a DD plasma, the fusion reaction rate peaks at very high deuterium energy (>1MeV) while the probability for charge-exchange dominates at relatively low fast-ion energies (~45keV). Therefore, beam-ions with a typical neutral injection energy ~100keV are readily diagnosed by charge-exchange diagnostics.

If the re-neutralized fast ion (fast re-neutral) escapes the plasma, it can be collected by detectors outside of the plasma. Neutral particle analyzers (NPA) can then discriminate the particle's mass and energy [2]. Unlike the detection of fusion products, NPA diagnostics provide a direct measurement of the fast-ion velocity. One major complication with NPA however is that fast re-neutrals can re-ionize before they exit the plasma, and the probability increases with

plasma density.

Another fast-ion diagnostic technique that exploits the charge-exchange process is fast-ion deuterium-alpha (FIDA) [3] [4]. A re-neutralized fast ion has the probability of becoming atomically excited either through the charge-exchange process or through collisions with the bulk plasma. An excited hydrogren atom that undergoes the atomic transition from n=3 → 2 will emit a photon at the familiar Balmer-α (or Dα in the case of deuterium) wavelength. The Dα wavelength of the emitted photon in the particle's frame-of-reference is λ_o=656.1nm. However, because of the superthermal velocity of the re-neutral, the wavelength of the emitted photon is Doppler-shifted in the lab frame. Consequently, the Dα spectral line is modified with a broad low-intensity feature in the presence of a fast deuterium population. This broad feature, consisting of blue- and red-shifted wings about the Dα line, is the subject of investigation for FIDA. One should then be able to measure the Dα spectrum and extract some information about the velocity distribution of the energetic deuterium population. In ideal conditions, the FIDA contribution is simply the difference between an active measurement (neutral beam on) and a passive measurement (neutral beam off). In practice however extraction of the fast-ion feature from the Dα spectrum can be difficult. Complications arise due to several variables, many of which result in low signal-to-noise ratios (SNR).

Section 1.2. Subtleties of the FIDA technique

Typically, FIDA is employed as an active charge-exchange diagnostic; that is, it results in internally localized measurements of the fast-ion distribution function. Core measurements are often sought after for information on the confined fast-ion population. For sufficiently high SNR, the injected neutral density along the beamline that the FIDA diagnostic monitors must be large

enough. The injected neutral density along the axis of the beam falls off approximately exponentially with distance. The 1/*e* folding distance depends on the plasma density n_e, where larger n_e leads to sharper fall-off. Another complication with high densities is the non-negligible contribution from bremsstrahlung radiation. Bremsstrahlung light has a broadband spectrum, and to a good approximation, its power per nanometer is relatively constant over the FIDA bandwidth. The intensity of bremsstrahlung increases with density as n_e^2. It has been observed empirically that line-averaged $n_e < 7\times10^{19}m^{-3}$ is optimal for extraction of FIDA from the Dα spectrum.

A second major complication comes from transient plasma events that cause changes to the background Dα spectrum. The most detrimental of these events are typically from edge-localized modes or ELMs. ELMs are associated with a burst of heat released at the edge of the plasma. One of the results is a sharp high-amplitude peak in a Dα time trace. When collected by the FIDA diagnostic, the bright burst scatters light into all detected wavelengths, resulting in a sharp increase of amplitude across the entire spectrum. If the ELM frequency is much lower than the diagnostic acquisition bandwidth, time slices including the ELM event are easily discarded.

A third complication with extracting FIDA from the raw spectrum involves impurity contaminants. Populations of non-hydrogenic impurities (such as B, C, and O) are present in the tokamak. When atomically excited they line-emit, and several lines are within the measured FIDA bandwidth. Some of the lines are excited by charge-exchange and are only present with the beam on. The rest are non-charge-exchange and are always present irrespective of the neutral beam. The non-charge-exchange lines are typically removed by the standard background subtraction technique (active signal – passive signal). However, instabilities and particle recycling at the edge can transiently alter the impurity density, leading to imperfect background

subtraction. Charge-exchange impurity lines must be removed by other means. Acceptable removal can be done by fitting the lines to an instrumental response curve (typically Gaussian).

Lastly, a fourth complication with measuring the FIDA spectrum comes from passive FIDA light. Fast ions that are expelled to the edge of the plasma, in the high neutral density region, can charge-exchange with the thermal neutrals. Prompt beam-ion losses as well as losses due to instabilities and non-axisymmetric perturbations can all contribute to the passive signal. If passive FIDA levels are significant and vary with time, the typical background subtraction technique would not completely eliminate the passive FIDA contribution. For example, one could imagine prompt losses of beam ions produced by the FIDA diagnostic beam at the edge of the plasma where the sightlines intersect. In this case, the passive FIDA contribution from the prompt losses would only be present when the diagnostic beam is on and would not get subtracted. However evidence of this has not yet been demonstrated on DIII-D. Although this remains an active area of research, for the cases studied in this thesis, the passive FIDA contribution is suspected to be negligible and always much less than the active FIDA contribution. A comprehensive discussion of the aforementioned subtleties regarding FIDA (with the exception of passive FIDA) can be found in [5] [6]. Once an experimental FIDA spectrum has been successfully extracted, an interpretation of it is often sought.

Section 1.3. Phase-space mapping

The population of energetic ions in a tokamak has a velocity distribution associated with it. One important question is: *what part of the distribution function dominates the measured signal?* The answer is quite complicated and depends on the measurement technique, but we can simplify the explanation with an elegant reduced-dimensional representation of phase space. A

full description of a particle in phase space at a particular instance in time depends on 6 independent variables, 3 spatial and 3 velocity. However, in conventional tokamaks toroidal axisymmetry is typically a good approximation, so the toroidal spatial coordinate is ignorable, and the toroidal canonical angular momentum $P_\zeta = \psi + Fv_{\|}/\Omega_i$ * is conserved. Furthermore, since the gyro-motion of a fast ion is typically much faster and smaller than characteristic temporal and spatial variations in the magnetic field, the particle's magnetic moment $\mu = \frac{1}{2}\, mv_\perp^2/B$** is well conserved. Furthermore, assuming conservation of particle energy $E = \frac{1}{2}\, mv^2 + q\Phi$***, we can describe a fast-ion orbit in terms of the three conserved quantities, P_ζ, μ, and E. The conservation of these quantities allows us to express the full distribution function $f(r_1,r_2,r_3,v_1,v_2,v_3)$ in a reduced-dimensional form e.g. $f(P_\zeta, \mu, E)$. However, the conserved quantities P_ζ and μ are often inconvenient variables to work with computationally, experimentally, and conceptually. Instead, we transform P_ζ and μ into real space and velocity variables $\chi \equiv v_{\|}/v$, R, and z, where R is the major radius of the torus and z is the vertical elevation from the midplane. In what follows, our phase-space maps are representations in (E, χ, R, z)-space, where we take slices along 2 dimensions (typically in R and z) to render a visual depiction of the the phase-space quantity (typically as a function of E and χ).

A discussion on the first-principles calculation of the fast-ion distribution function is beyond the scope of this work. The most common and comprehensive model that calculates the distribution function for neutral-beam-produced and fusion-produced fast ions is the NUBEAM [7] module of the TRANSP [8] transport code. The model calculates the guiding-center drift

---

* ψ is the poloidal magnetic flux, F is the poloidal current function, $v_{\|}$ is the velocity component parallel to B, and Ωi is the cyclotron frequency

** $v_\perp$ is the velocity component perpendicular to B

*** Φ is the scalar potential

orbit during the slowing-down process, handling various collisional and atomic physics. Among the outputs, the distribution function is calculated assuming toroidal axisymmetry. A sample velocity distribution of deuterium beam ions near the magnetic axis on DIII-D is shown in figure 1.1. The figure is presented merely to show a typical reduced representation of the distribution of beam ions. It is common to present the distribution as a function of total energy E and pitch $\chi \equiv v_{\|}/v$, where the sign of $v_{\|}$ depends on the direction with respect to the plasma current Ip (a negative value indicates $v_{\|}$ is opposite to the direction of Ip). The distribution function is sampled by a measurement which has an associated sensitivity in phase space. Naturally, a proper interpretation of a fast-ion diagnostic measurement requires knowledge of its sensitivity in phase space, i.e. its instrument function. Equipped with a sensible prediction of the distribution function and a measurement's instrument function, one can make convincing arguments regarding the evolution of the fast-ion population.

For a detailed explanation on the calculation of various fast-ion instrument functions, see the appendix of [9]. As mentioned earlier, many fast-ion measurements involve the detection of fusion products. Among them, neutron diagnostics are typically employed since their trajectories are uninfluenced by the electromagnetic fields. As discussed earlier and presented in eq. 1.3, the neutron rate depends on the relative velocity of the reactants. If beam-target or beam-beam reactions dominate the total neutron rate, a neutron measurement can be effective as a fast-ion diagnostic. With the velocity distribution of energetic ions and thermal ions, it is possible to estimate the probability for fusion reactivity (figure 1.2). We can then construct a velocity-space map that tells us the probability of fusion reactivity (and thus probability of neutron emission) for fast ions with a particular velocity. An example of such a map is shown in figure 1.3. The term “instrument function” will be used to represent the velocity-space sampling of a

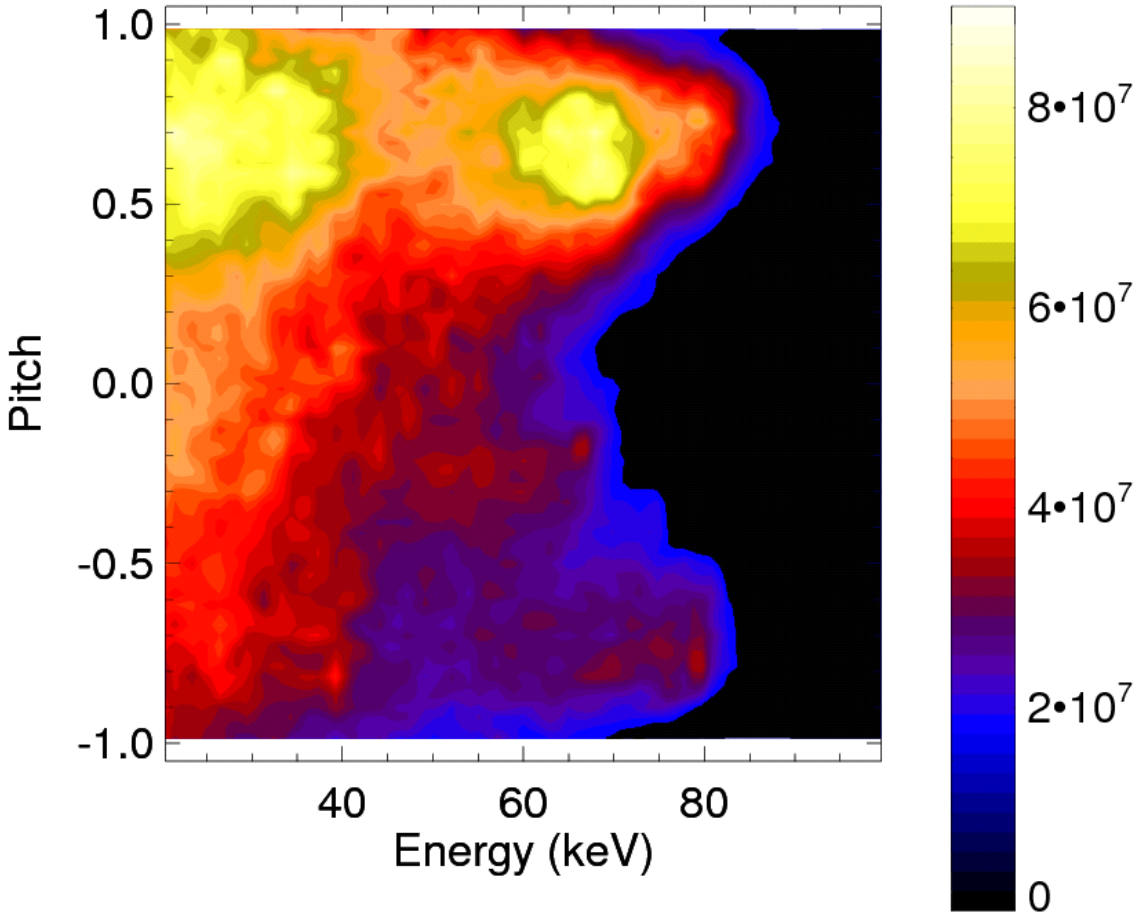

Figure 1.1.

measurement. Figure 1.2 is the neutron instrument function for the 2.45MeV DD neutron rate measured by a neutron counter located external to the DIII-D tokamak. As one can see, the fusion reaction rate increases with fast-ion energy, peaking well above the typical neutral deuteron injection energy of 80keV. The primary goal of figure 1.2 is to show that this neutron measurement volume-averages over a broad region of velocity space. If we convolve the neutron instrument function (figure 1.2) with the fast-ion distribution function (figure 1.1), the result is the "weight function" (figure 1.3). The term "weight function" refers to the fast-ion contribution to the measured signal; it is the combined response of the instrument function and the velocity-space distribution of fast ions. (As an aside, it should be mentioned that the definition of "weight

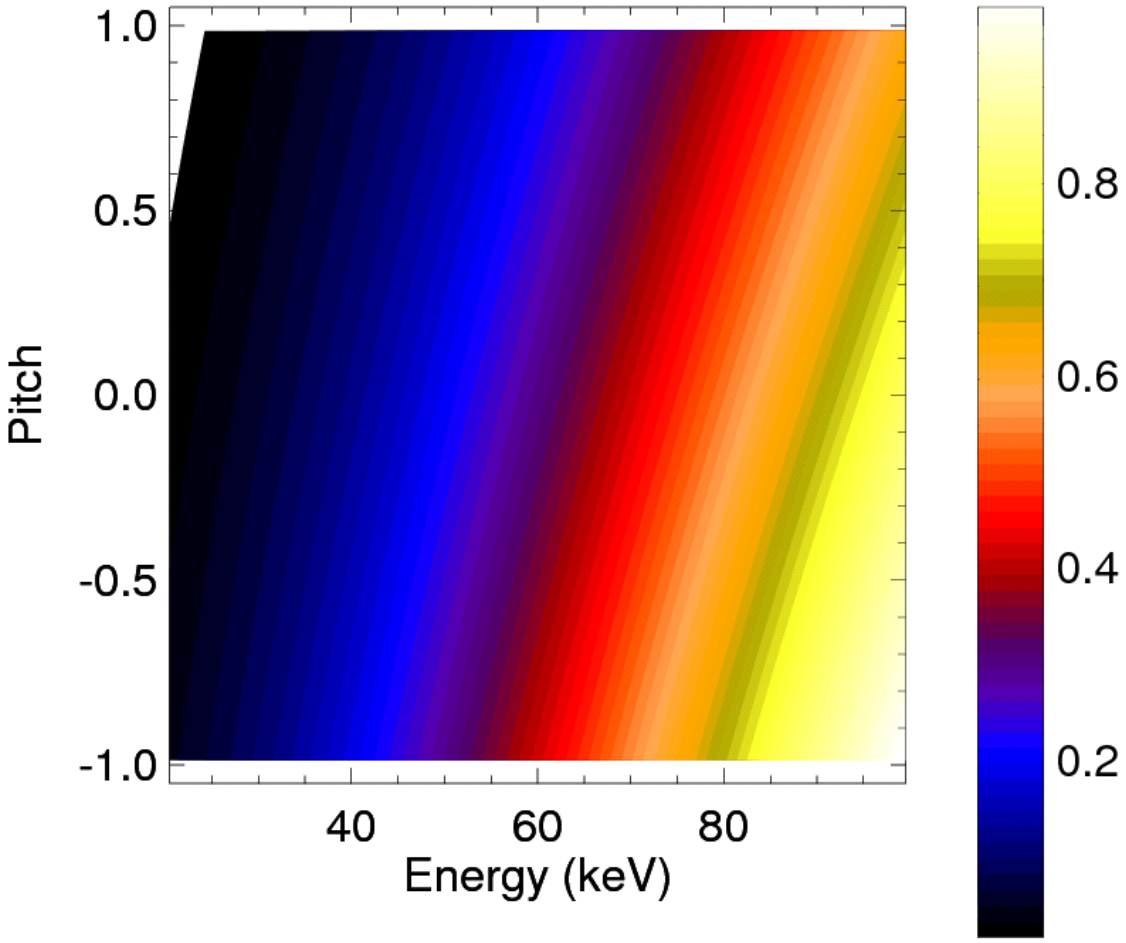

Figure 1.2.

function" used in this thesis differs from ref. [9] where the term "weight function" referred to what we call here the "instrument function." In the above reference, no name was given to the product of our instrument function and velocity-space distribution.) The neutron weight function approximately recovers the distribution function; thus a fusion-product type of diagnostic can provide a reasonable measurement of the *integrated* fast-ion distribution. Information on the collective behavior of the fast-ion population can be used, for example, to study heating, to determine the fast-ion slowing-down time, and to monitor effects of instabilities on fast-ion confinement.

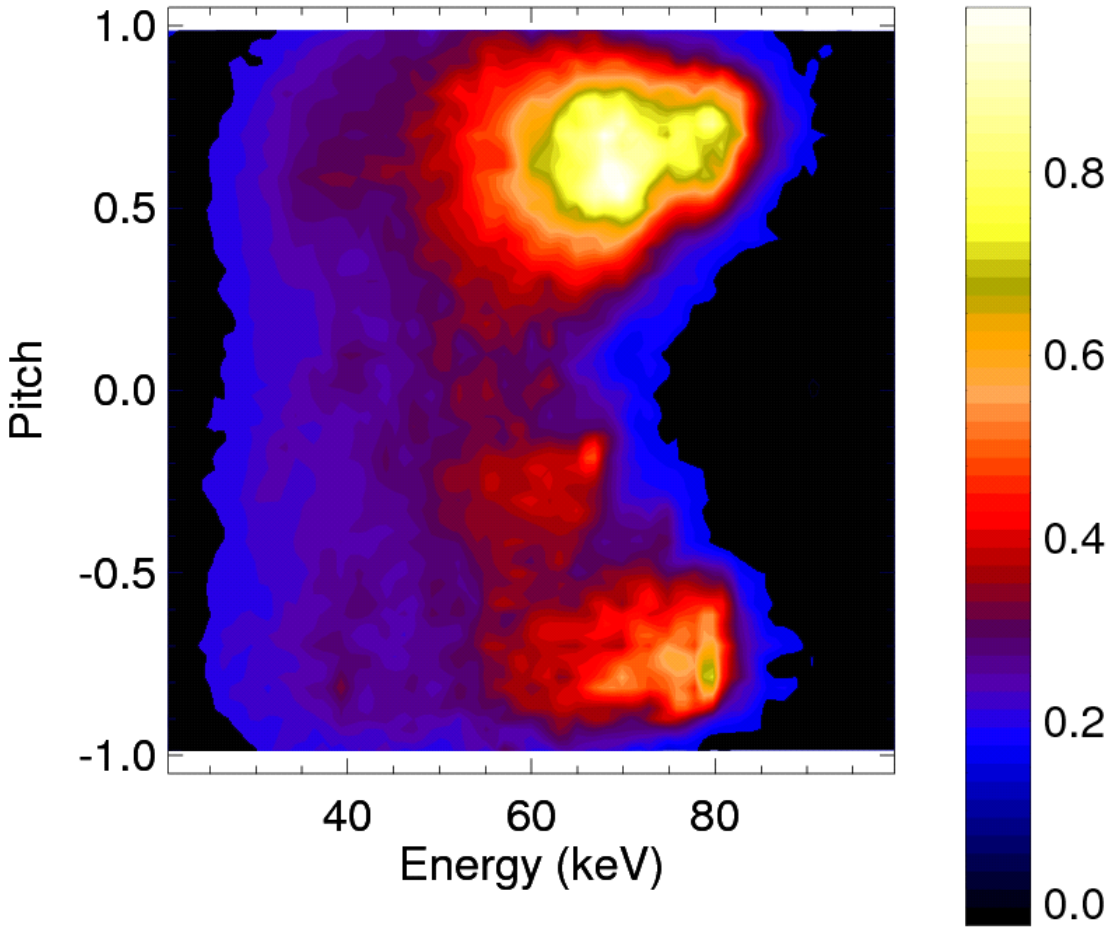

Figure 1.3.

Most modifications to the fast-ion distribution function occur anisotropically in phase space. For example, many instabilities interact with energetic particles that satisfy a wave-particle resonance condition. The condition involves a relationship between some characteristic orbit timescale and the frequency characterizing the wave, which can only be satisfied for certain types of orbits. Then we expect the resonant particle population to interact somehow with the wave (e.g. orbit modification leading to particle transport), modifying the resonant part of the distribution function. With a diagnostic integrating a broad region of velocity space (e.g. neutron detector), inferences about specific parts of the distribution function are often impossible.

However in theory, these velocity-space anisotropies should be detectable. Equipped with a diagnostic having an instrument function that is bounded in velocity space (in contrast to the above neutron example), we are restricted to conclude about fast ions in the detectable region. FIDA is such a diagnostic whose instrument function is relatively localized in velocity space and in real space. The spatial localization of FIDA is simply determined by the viewing sightline. The intersection of the sightline with large neutral density regions (plasma edges and neutral beam) govern the spatial collection volumes. Determination of the velocity-space localization is significantly more involved.

The FIDA instrument function in velocity space depends on the physical processes (charge-exchange and proper atomic excitation/transition) which ultimately generates the signal. Just like the probability for fusion reactivity determines the neutron instrument function, the probability for charge-exchange partially determines the FIDA instrument function. A sample probability distribution for D^+D^0 charge-exchange on DIII-D is shown in figure 1.4. As mentioned earlier, the cross-section peaks for relatively low fast-ion energy (~ 45keV). In addition to the probability for charge-exchange, the FIDA instrument function also includes orbit and instrumental considerations. FIDA is a relatively collimated diagnostic, and only photons emitted along the sightline are detected. The photons are then discriminated according to their energy by dispersing the light into a spectrum. Wings of the Dα spectrum are generated by Doppler-shifted photons from the re-neutralized fast ions. A particular Doppler shift $\Delta\lambda = |\lambda - \lambda_o|$ corresponds to the energy component of the fast re-neutral along the trajectory of the photon. Therefore, each wavelength of the FIDA spectrum can be characterized by a *measured* energy. This *measured* energy E_λ determines one component (the one parallel to the sightline) of the energy of the re-neutralized fast ion. At a particular Doppler shift, E_λ , the lowest energy particle

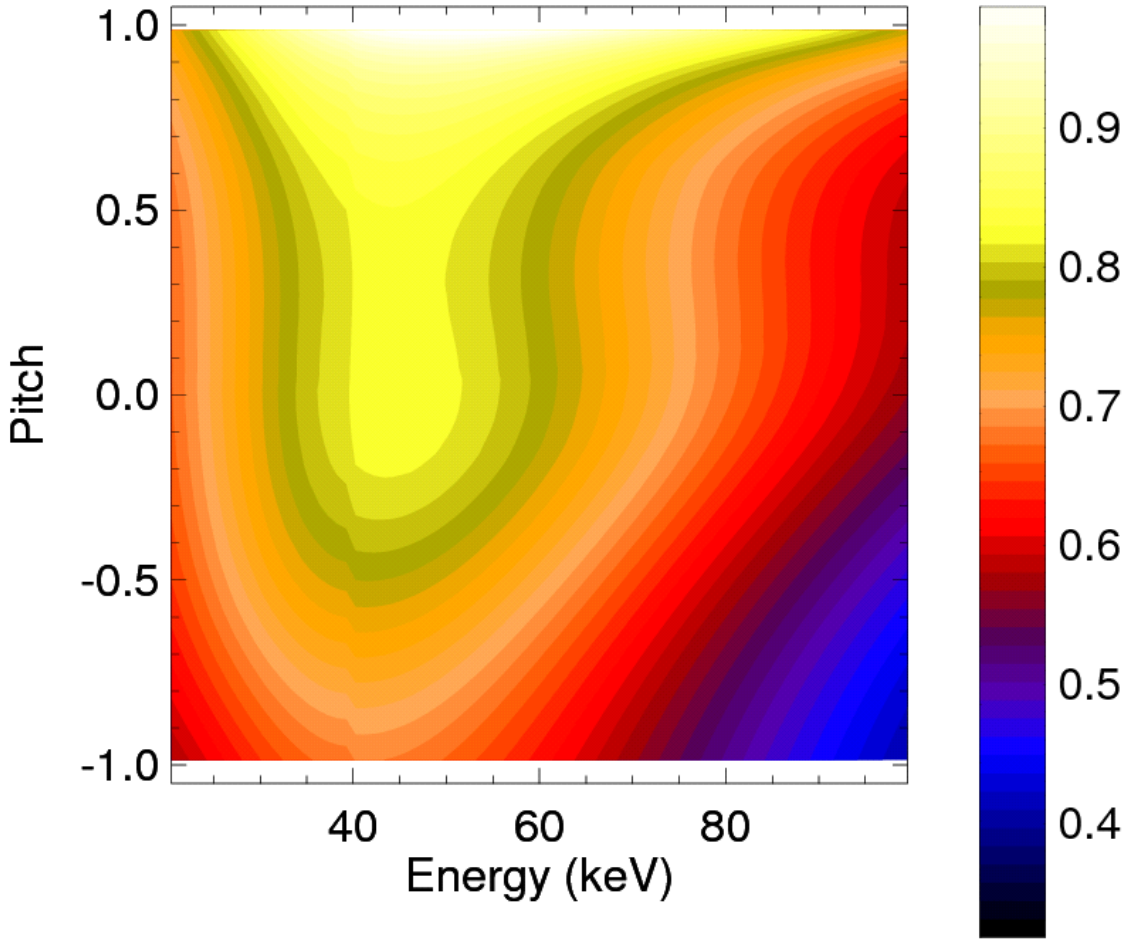

Figure 1.4.

that can contribute a photon to the spectrum is one that has total energy $E=E_\lambda$ and is traveling parallel or anti-parallel with respect to the detector sightline; this corresponds to a particle with unique values of E, pitch ($\chi \equiv v_{||}/v$), and gyroangle. Fast ions with energy $E>E_\lambda$ can also contribute a photon to the measured spectrum at E_λ , but they must have a different value of pitch χ or gyroangle. There is a minimum total energy curve $E(\chi)$ associated with every value of E_λ ; only particles traveling parallel or anti-parallel to the sightline will satisfy the minimum energy condition. This describes only 2 gyroangles for a given particle. Particles with gyroangles

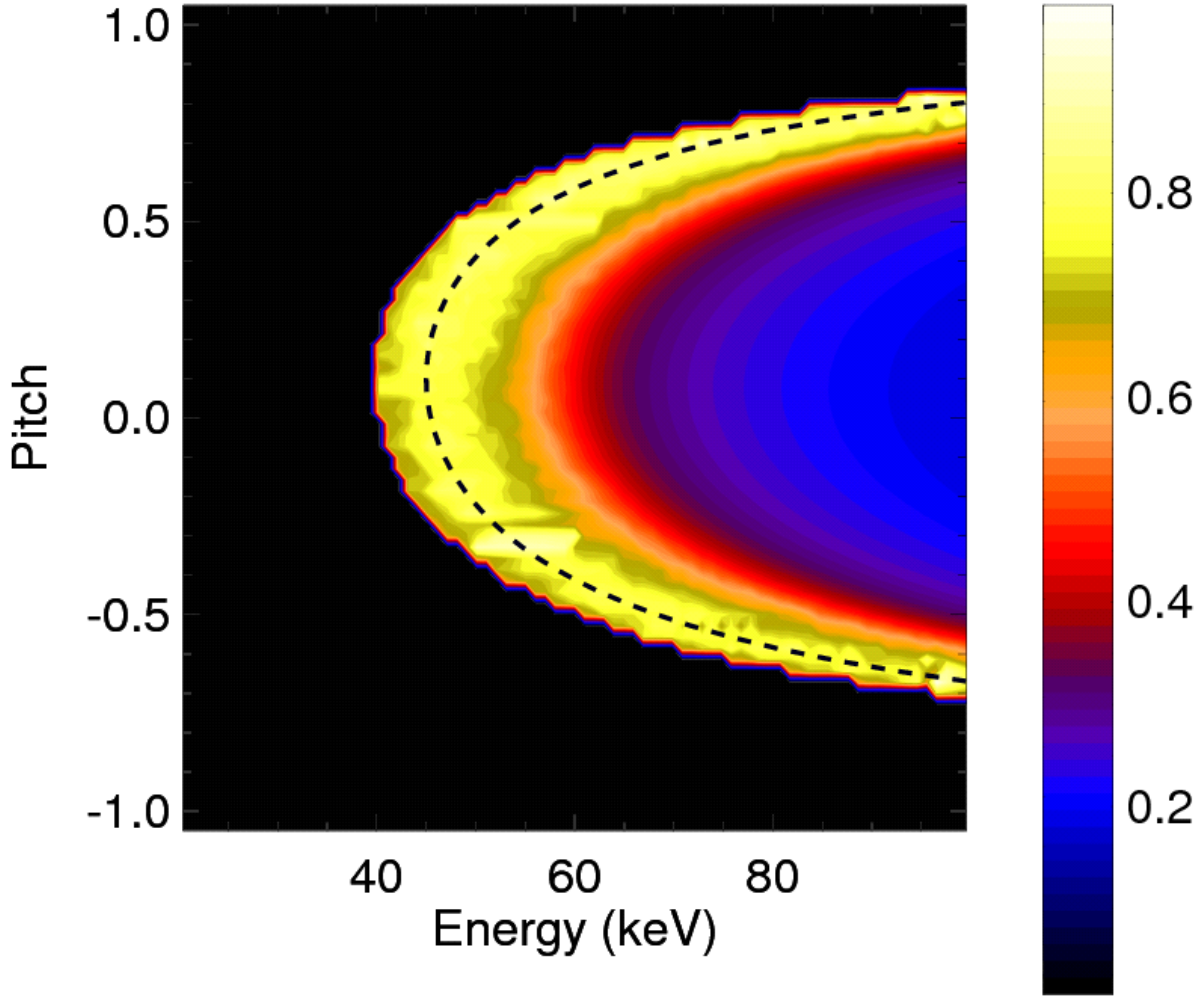

Figure 1.5.

intermediate to those producing the minimum energy curve can also emit a photon with the correct Doppler shift; their energy just has to be higher. A weighting function is calculated from these orbit considerations. The mathematical details can be found in [9], and a similar analysis applied to the fast-ion collective Thomson scattering system envisaged for ITER can be found in [10]. A sample orbit weighting function for a vertically viewing system is shown in figure 1.5. The minimum energy curve is overlaid in black. The colored contours are due to gyro-weighting, where the heaviest weight is from particles traveling directly toward or away from the detector.

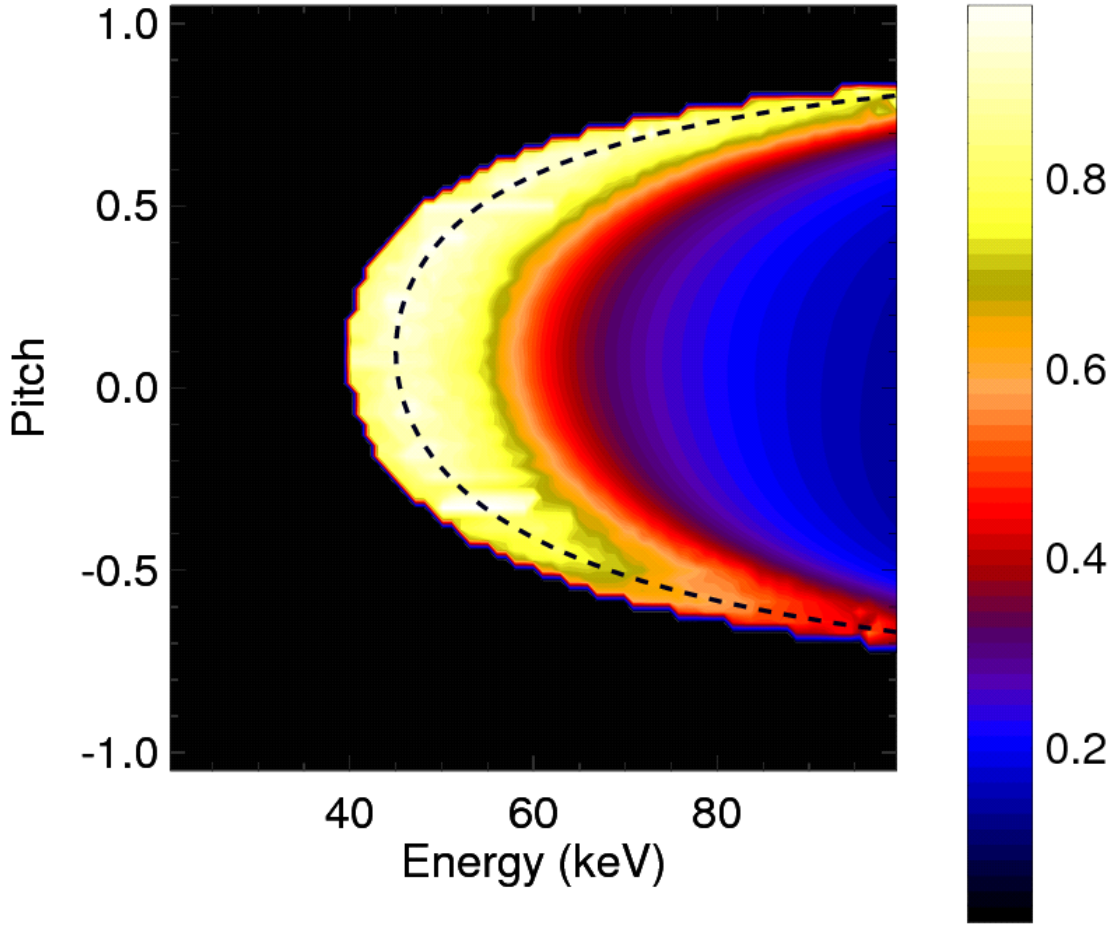

Figure 1.6.

An additional effect that modifies the instrument function is the intrinsic spectral broadening of the optical detection system. This effect is approximately Gaussian and leads to a contribution from a band of energies less than the minimum energy curve. In practice, a slit is utilized to obtain the desired spectral resolution. The resolution is naturally limited by ~1nm Stark splitting of the spectral components due to the electric field produced by the $\mathbf{v}\times\mathbf{B}$ motion of the bulk plasma. Thus, the slit width is chosen to achieve a spectral resolution of about 1.0nm or about 10keV spectral energy resolution.

The *total* FIDA instrument function (figure 1.6) is then the convolution of the charge-exchange probability distribution (figure 1.4) and the orbit weighting function (figure 1.5),

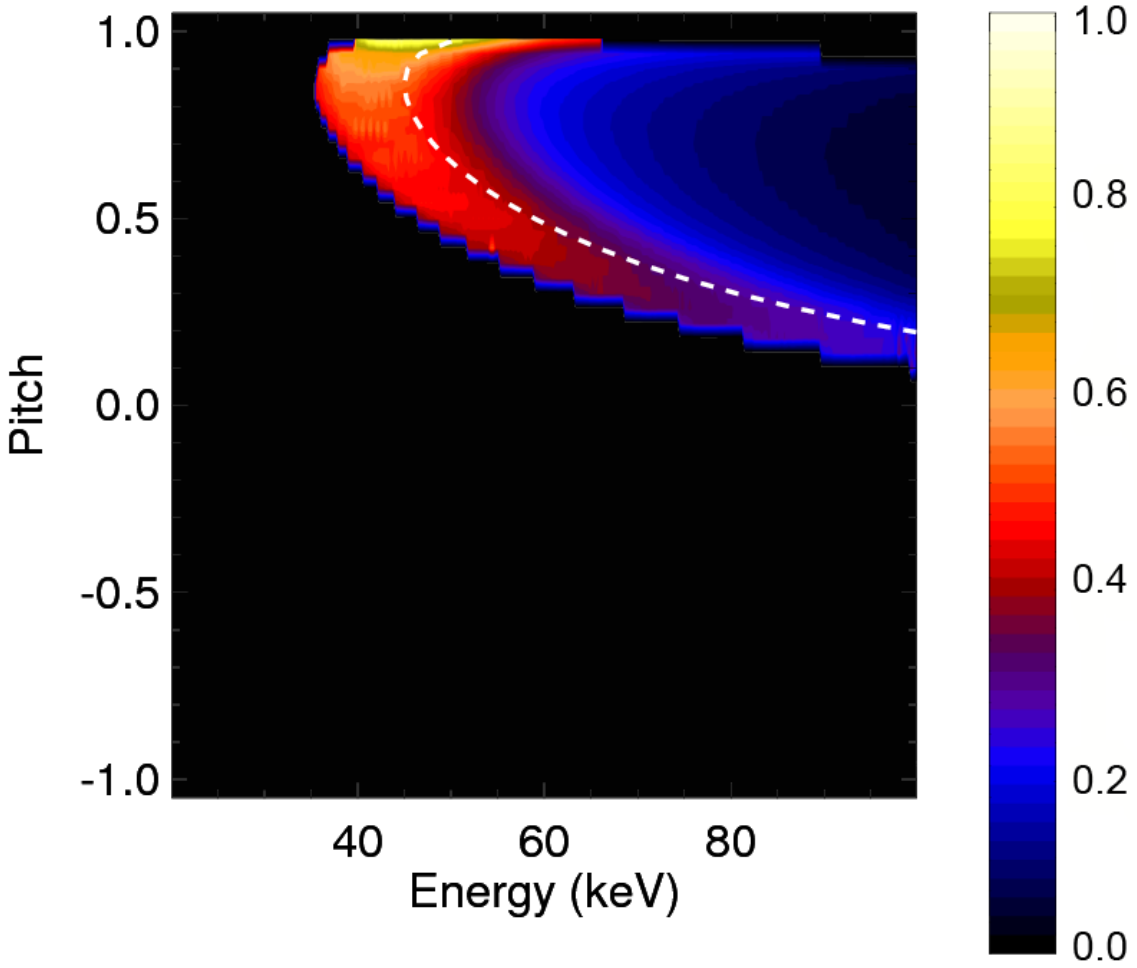

Figure 1.7.

corrected for spectral broadening. The example FIDA instrument function is presented for a sightline (unit vector **s**) that views a neutral beam nearly perpendicular to **B** (**s** ·**B** ≈ 0) and for E_λ = 45keV at r/a = 0.5. The shape of the instrument function is determined by the geometry of the FIDA sightline. For the vertical system on DIII-D which is nearly perpendicular to **B,** the shape is approximately a parabolic function of pitch χ with the minimum at $\chi \approx 0$ (corresponding to the pitch of the sightline). For sightlines with a component parallel to **B** (**s** ·**B** ≠ 0), the shape is skewed; the amount of skewness depends on the magnitude of (**s** ·**B**)/|**B**|. An example of the FIDA instrument function for an oblique sightline with parallel and perpendicular components to

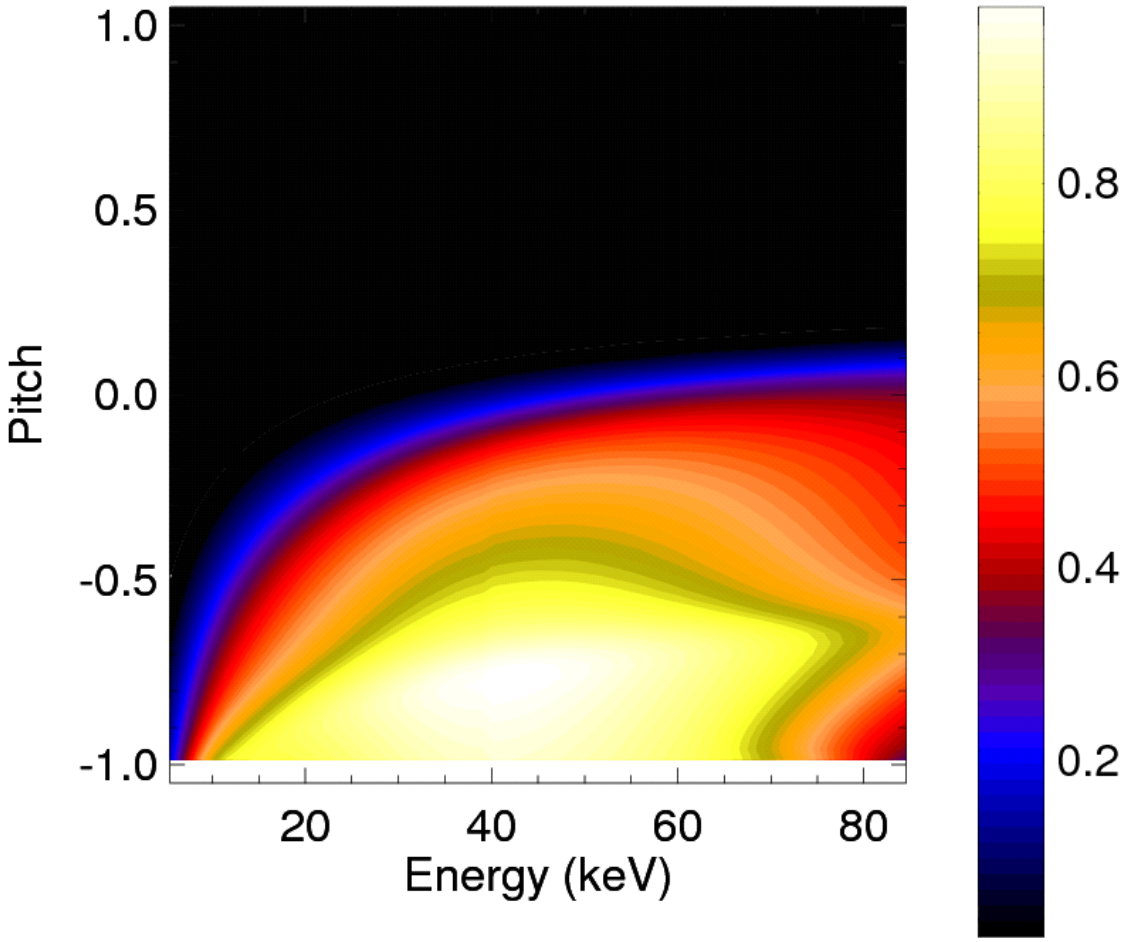

Figure 1.8.

B is shown in figure 1.7. This instrument function is presented for the same E_λ and r/a as the vertical FIDA instrument function in figure 1.6, but the sightline is a more tangential view of the field (comparable perpendicular and parallel components). Therefore, the minimum occurs for a pitch which is intermediate between a completely perpendicular view ($\chi = 0$) and a completely tangential view ($\chi = \pm 1$). An example of the instrument function for a tangentially viewing FIDA system on DIII-D is presented in figure 1.8. It views the neutral beam in the midplane, nearly parallel to **B** at the beam intersection. For this system, the minimum occurs at χ=-1. This tangentially-viewing system differs from the vertical and oblique systems in the details of the

light detection hardware. These details will be discussed in the next section. This tangentially-viewing detector images integrated bandpass filtered light, so spectral resolution is lost. The effective spectral bandpass corresponds to E_λ=10-80keV. It becomes clear that multiple FIDA systems with significant variations in their sightline geometries can provide the ability for velocity-space discrimination.

Section 1.4. FIDA on DIII-D

Data from the FIDA suite on DIII-D used in this thesis originates from 3 different optical installations. The projection of their sightlines in the DIII-D vessel are shown in figure 1.9. The vertical FIDA system consists of 2 dedicated viewing chords and 12 chords shared with the charge-exchange recombination (CER) system [11]. The spectra of the 2 dedicated vertical chords are monitored on every plasma shot by the 1st generation FIDA system [5], consisting of a spectrometer and charged-coupled device (CCD) camera. If the full vertical spatial profile is desired, the CER spectrometers (which typically monitor carbon spectral lines) are re-tuned to the blue wing of the Dα spectrum for FIDA measurements. All radial chords of the vertical system share a similar instrument function as the one presented in figure 1.6 for E_λ = 45keV. Another system which monitors FIDA is a fast-framing camera. When used in conjunction with a Dα narrowband filter, the imaging system provides 2-dimensional profiles of the FIDA emission [12]. The filter provides *in situ* bandpass integration of the collected light corresponding to spectral energies E_λ = 10-80keV. Recall the FIDA imaging instrument function for a typical sightline presented in figure 1.8. The vertical and imaging systems correspond to views that are perpendicular and tangential to **B**, respectively. Another system installed on DIII-D that has oblique sightlines, possessing comparable perpendicular and parallel components, will

be referred to for the remainder of this thesis as the oblique FIDA system. The design and construction of this system was a major portion of this thesis work and will be described in detail.

Due to the success of the original FIDA system and the potential for greater velocity-space and spatial coverage, a new FIDA installation (2nd generation FIDA or 2G FIDA) was commissioned on the DIII-D tokamak [13]. Many design aspects of this new diagnostic were adopted from the existing FIDA system on NSTX [14]. Furthermore, the array of hardware improvements and the addition of a fast-integrated PMT assembly substantially extend the capabilities of the DIII-D FIDA suite. Collection of visible photons is relatively straightforward using standard optical components. On the tokamak end of the diagnostic, a total of 42 fiber optics make up the viewing chord array. See Table 1.1 for the fiber optic specifications. Each radial chord consists of 3 toroidally displaced fiber views to increase the system's light gathering ability. When a chord is back-lit and projected on the midplane, the 3 spots are toroidally aligned with adjacent spots separated by 10cm center-to-center. The average spot diameter is ~4cm which is approximately double the intrinsic spatial resolution determined by the mean-free-path during the lifetime of the n=3 atomic state [6]. See figure 1.9 for a comparison of the geometries of the oblique and vertical views. As discussed earlier, their differing sightline geometries provide different weightings in fast-ion velocity space, making it possible to compare different fast-ion populations. The older vertical views intersect the magnetic field nearly perpendicularly, having a large vertical component and much smaller toroidal and radial components. These chords utilize one of DIII-D's co-Ip neutral beam sources (330L) which injects in the same direction as the plasma current Ip in a typical discharge. This geometry prevents contaminating light due to beam emission from entering the collection optics. The new views intersect the field

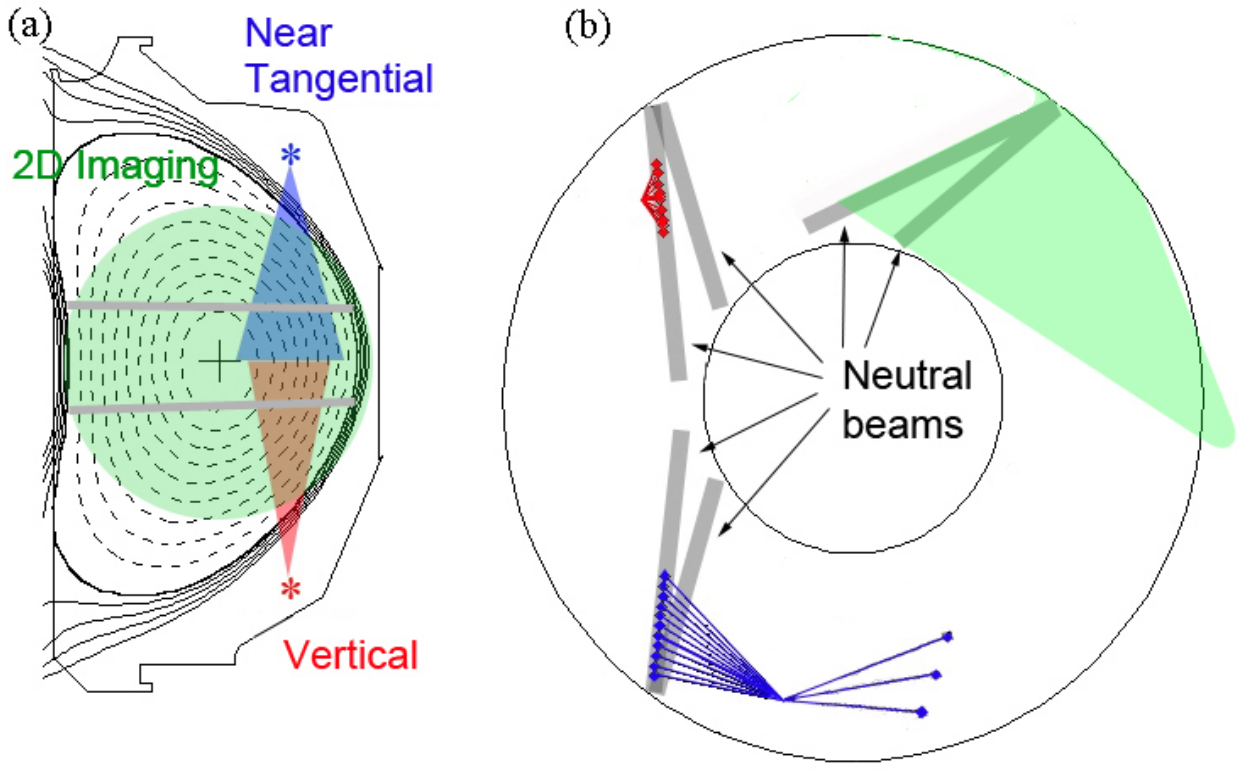

Figure 1.9.

more tangentially, possessing a large vertical *and* toroidal component. These chords view a neutral beam source which injects in the opposite direction of the typical plasma current on DIII-D (210R), a so-called counter-source. When viewing the beam from behind (as is the case for the oblique views), the light from beam emission is red-shifted. Therefore, we only concern ourselves with the blue wing of the spectrum, since it is not complicated by Stark components of the beam emission. The active signals (those viewing a neutral beam) consist of 11 chords spanning major radii of 170cm to 223cm (normalized toroidal flux coordinate $\rho \approx 0.00$ to 0.80, typically). The passive signals (displaced toroidally from the neutral beam and projecting onto a similar part of the tokamak floor as the active views) consist of 3 chords spanning major radii 170cm to 209cm. Since the sightlines integrate the light along the entire chord length, signal from all sources emitting at or near the Dα wavelength can contribute to the measured spectrum, including active FIDA, passive FIDA from charge exchange with cold edge neutrals,

bremsstrahlung radiation, and active and passive impurity radiation. Extraction of the active FIDA feature is the goal, so background subtraction techniques must be employed to remove the other contributions to the spectrum [5]. Beam modulation (where the diagnostic beam is switched on and off intermittently) is the conventional method to obtain active and background

Collection fibers 11 active chords 3 passive chords	Core mat'l	Num. Aper.	Core diam.	Max. trans.	Attenuation
	Silica	0.37	1500μm	>99.8% @ 650nm	3dB/km @ 650nm

Table 1.1.

signals during steady-state periods. 2G FIDA also employs this method of background subtraction, but the 3 passive views permit an additional level of background monitoring. Each method has its pros and cons: obtaining passive and active signals using beam modulation ensures toroidal equivalence but requires temporal constancy; the toroidally-displaced passive-viewing method ensures temporal equivalence but requires toroidal symmetry. For the FIDA data presented in this thesis, beam modulation was employed for background subtraction with the spectroscopic system (described below), while the 3 passive views were typically employed with 3 equivalent active views on the fast integrating system (described below).

D-alpha light enters the 2G FIDA collection lens after the rays reflect off a series of mirrors. The purpose of the mirrors is 2-fold: 1.) to redirect the oblique chords through a vertical port in the tokamak and 2.) to accommodate both active and passive chords with the same set of optics. For maximum reflectivity and to reduce scatter, the mirrors are ground to 65nm roughness and 3μm flatness and are coated with a highly reflective material called "Beral." After their last reflection, the rays pass vertically through a port aperture and sapphire window separating the collection lens from vacuum. The lens is a 40mm diameter, 60mm focal length Edmund Optics biconvex with antireflective coating yielding maximum transmission (>99%) at

~650nm. For greatest throughput, a lens aperture is fitted to match the fiber optics' f/# of 1.8. The lens focuses all 42 viewing lines onto a fiber optic array. A fiber optic mount is located at the lens's axial focal plane. Many chords have off-axis and oblique incidence as they pass through the lens resulting in a non-planar focal surface. Because of the spherical nature of the lens surface, the effect is an approximately spherical focal surface. To account for this, the surface of the fiber optic array is empirically fitted to the lens's focal surface, whose radius is ~30mm.

The light traverses about 50m of fiber optics, passing through a radiation shield wall, and is transmitted to the FIDA diagnostic lab. The fibers are arranged onto a patch panel allowing the user to choose which signals should be sent to each instrument. Three instruments are currently available: 1.) original FIDA spectrometer: Czerny-Turner spectrometer and CCD camera, 2.) s-FIDA: transmission grating spectrometer and CCD camera and, 3.) f-FIDA: fast integrating system with photomultiplier tube (PMT). The remainder of this section will focus only on the s-FIDA and f-FIDA systems. Information on the original FIDA system can be found in [15] [5].

Section 1.4.a. s-FIDA hardware

Similar to the original FIDA instrument, s-FIDA is a spectroscopic system with the goal of obtaining the Dα spectrum for several chords. The s-FIDA instrument is capable of recording data from 6 radial chords in a single discharge. A repeat shot is necessary to obtain the entire spatial range. The HoloSpec transmission grating spectrometer [16] is a very compact device with stigmatic imaging; when used in conjunction with our Newport bandpass filter [17], the spectrometer is designed to allow close positioning of fibers at the input focal plane with low crosstalk amongst neighboring channels. Three fibers composing a radial chord are stacked

vertically, arranged in a 2 × 3 channel array. Because it is a fast optical system (f /1.8), the spectrometer produces strong curvature at the output focal plane [18]. To correct for this curvature, instead of straight input slits, they are designed as arcs of a circle according to eq. 12 of Ref. [18]. Since the dispersion varies strongly across the transverse axis of the spectrometer, varying slit widths are chosen to keep the spectral (energy) resolution constant at ~0.5nm (~10keV). Stark splitting from motional $\mathbf{v}\times\mathbf{B}$ and from plasma electric fields causes ~1nm spread of the Dα emission, so the intrinsic spectral resolution of the diagnostic is limited to ~1nm. A 12-bit Sarnoff CAM1M100 CCD camera [19] captures the spectra on a 1024×1024-pixel chip. Since the vertical pixels for each channel are redundant, they are binned to achieve a readout rate of 1kHz. Neutrons escape the plasma and can activate materials producing gamma rays. The CCD chip is sensitive to gamma rays, so the diagnostic must be shielded from such radiation. The shield consists of 2 walls: the outer wall is a 4" thick wall of high-Z 5% boronated polyethylene to prevent neutron penetration and it surrounds a 4" thick wall of lead to block gamma rays. This design is highly successful and is utilized at DIII-D with most radiation-sensitive detectors.

Both random and systematic errors contribute to uncertainties in an s-FIDA measurement. The three dominant sources of random errors are readout noise, dark current (from thermal noise), and photon noise. To reduce the effects of dark current, the CCD is cooled to 273.5K via a chilled water line and thermoelectric controller. For a given frame, the dark current (independent of wavelength) dominates in the high-energy portion of the spectrum. Photon noise, on the other hand, dominates in the low-energy region, increasing as (# of photon counts)$^{1/2}$. In general, the signal-to-noise ratio (SNR) is better than unity for all relevant wavelengths except at very high Doppler shifts, typically corresponding to $\Delta\lambda>5$nm ($E_\lambda>55$keV).

Section 1.4.b. f-FIDA hardware

When time-averaged during steady conditions, s-FIDA provides the capability to reasonably infer the energy distribution of fast deuterium ions. If high time resolution of the FIDA signal is desired, the s-FIDA system described above will not suffice. Many instabilities such as neo-classical tearing modes (NTMs) and Alfvén eigenmodes occur at frequencies O(10-100kHz), which requires SNR>1 at diagnostic acquisition rates of at least twice the mode frequency to resolve the fluctuation. Because of its relatively low gain and the requirement to build charge to produce a sufficient SNR, CCDs are insufficient "fast" acquisition devices. Instead, the combined use of bandpass filtering and a photomultiplier tube (PMT) can satisfy this need. The goal of f-FIDA is to obtain wavelength-integrated signals on a timescale short enough to resolve high frequency macroscopic fluctuations. It is a compact design and has the capacity for accommodating signals from 8 radial chords. At the time of writing, 6 of the available 8 channels are currently in use. The 6 fiber bundles are mounted within a 2" diameter circle in order to collectively transmit the light signals through a single filter. An array of 8 aspheric lenses is positioned away from the fiber bundle by a distance equal to the lens's focal length; the lenses collimate the light for transmission through a bandpass filter centered at 653nm. Rays oblique to the surface of the filter cause a down-shift in the wavelength pass-band, and the amount of shift depends on the characteristics of the filter. Therefore, a high degree of collimation is required to achieve the designed bandpass. The maximum divergence of the collimated rays is ~2º resulting in a wavelength shift of ~0.2nm, much smaller than the 3nm bandwidth. After the light is filtered, the rays are refocused by another array of lenses, and the filtered signal is transmitted to the Hamamatsu H8711-20 PMT [20] by a set of jumper fibers. The multichannel PMT is designed as a 4×4 array, and the fibers are arranged in a checkerboard

configuration so that no two active channels are directly adjacent. This design reduces the electronic and photonic crosstalk by about 70%. To prevent stray light from entering the f-FIDA optics and contaminating the signals, a light-tight aluminum enclosure shields the diagnostic. Each active channel of the PMT generates a current signal, which is first amplified and then sent to a digitizer. Although the digitizer acquires at a 1MHz sampling rate, the diagnostic can resolve fluctuations up to ~200kHz. The upper bound of the bandwidth is limited by the number of photons; empirically, the SNR quickly approaches unity for fluctuations above 200kHz. Although the data from f-FIDA has been useful for a variety of studies, its role in subsequent chapters of this thesis is negligible. A brief demonstration of f-FIDA data during neoclassical tearing modes is presented in appendix B.

Section 1.4.c. Sample s-FIDA data

Figure 1.10 displays sample s-FIDA data from DIII-D shot 146088. Early in the discharge (t<1600ms), conditions are ideal for FIDA analysis; the first 1600ms provides a MHD-quiescent ELM-free period with low line-averaged density ($<3\times10^{19}m^{-3}$) and low neutral beam power (1.5MW). To generate the fast-ion population, one co-source fires continually at 60kV injection voltage. Three other sources are modulated at 10%, 5%, and 5% duty cycle for FIDA and diagnostic purposes. The electron temperature peaks on-axis at about 2keV, and $\beta\equiv\langle p\rangle/2\mu_o B^2$ (where $\langle p\rangle$ is the mean plasma pressure) is steady at 0.14%. The plasma current (Ip) and toroidal field (Bt) are steady at 1.1MA and 2.1T, respectively. The spectra in figure 1.10 are obtained from the oblique viewing chords intersecting the beam at the midplane for major radii R=170, 181, 191, 203, 214, and 223cm (normalized minor radii r/a=0.0, 0.18, 0.34, 0.54, 0.72, 0.87). Spectra are generated by averaging over t=1370-1390ms. Background subtraction is

performed using the beam modulation technique where the average passive spectra (t=1370-1380ms) are subtracted from the average total spectra (t=1380ms-1390ms). The difference between the average total spectra (blue) for a beam-on pulse of 10ms and the average passive spectra (green) during beam-off duration of 10ms results in the active FIDA spectra (black). Uncertainty about the mean arises due to fluctuations in the signal. The error bars are calculated from the standard deviation of the ensemble. The random errors in the active FIDA spectrum σ_a are calculated by adding in quadrature the standard deviations of the average passive spectrum (σ_p) and the average total spectrum (σ_t),

$$\sigma_a = (\sigma_t^2 + \sigma_p^2)^{1/2} \quad (1.4)$$

This is valid as long as the ensemble of total and passive spectra are normally distributed. This is the fluctuation error associated with deviations of the experimental spectrum about the mean. Besides fluctuations associated with changing plasma parameters, fluctuations can arise due to instrumental uncertainties: photon noise (counting statistics), dark (thermal) noise, and readout noise. Dark noise and readout noise are wavelength independent while photon noise (equal to the square root of the number of photons) depends on the intensity of the spectrum. Analysis shows that the measured error σ_a and the calculated error from photon noise are typically comparable when the plasma conditions are steady, implying that photon noise is likely the dominant contributor to the measured variation. When plasma conditions vary significantly over the time integration window of the data, σ_a is larger than instrumental uncertainties. Time variations in numerous plasma parameters can cause the additional fluctuations in FIDA signals; the most obvious is the fast-ion density profile. Two other important ones are the electron density profile

(affects the fast-ion slowing-down time, neutral-beam deposition, charge-exchange probability) and electron temperature profile (affects the slowing down time). Throughout the thesis, error bars on FIDA spectra denote measured errors (σ_a) unless otherwise noted.

Also plotted in figure 1.10 is the predicted visible bremsstrahlung emission (VBE) spectrum (calcuated by the FIDA synthetic diagnostic described below) integrated along the FIDA sightlines. The VBE is calculated using experimentally determined plasma profiles and EFIT reconstructions of the plasma equilibrium. VBE determines the spectral baseline. At modest Doppler shifts (typically $\Delta\lambda > 3$nm), the contributions from the cold edge neutrals to the passive Dα spectrum are negligible. Therefore, except for impurity line emission, the spectrum should drop to the VBE level. Similarly for the total Dα spectrum, at Doppler shifts larger than the those corresponding to the highest-energy fast ions (typically $\Delta\lambda > 6$nm), the spectrum should converge to the VBE level. We see in figure 1.10 that this is not the case for the passive and total spectra measured by the oblique FIDA system. The measurement has an extra offset, leading to a factor of ~2 difference between the calculated VBE and the average baseline of the passive spectra (average of spectra over large Doppler shifts after removal of large oxygen-V line at 650nm). Scattered light within the Holospec spectrometer and cross-talk amongst neighboring channels on the CCD chip are plausible culprits. Tests were performed to measure the scatter and cross-talk. The fibers of 5 of the 6 channels on the CCD are illuminated uniformly by a calibrated light sphere, and the signal on the remaining dark channel is measured; this is repeated three times for each channel, where each iteration corresponds to setting a different luminance value emitted by the light sphere. Changes in the signal compared to a true dark frame (light sphere off) signify some sort of stray light. If the contaminating light signal possesses the bandpass spectral response, the source is likely cross-talk amongst vertically-stacked channels on

the CCD chip (due to unfocused or misaligned camera). If the contaminating signal is broadband, essentially adding an offset to the noise level, the source is likely due to scattered light within the spectrometer. Figure 1.11 is data from a representative channel. Figure 1.11a is a spectral plot of the dark channel during the illumination iterations. The black curve is a true dark frame with the light sphere turned off. The red, green, and blue curves are the signals on the dark channel when the fibers of the remaining 5 channels are illuminated (corresponding to luminance values of 100ftL, 200ftL, and 300ftL, respectively). Since the bandpass response is absent during the illumination, scattered light within the spectrometer is likely the source of the stray light. We can see from figure 1.11b that the response is linear. The ordinate is the summed CCD counts from the dark channel while the abscissa is the summed CCD counts from the remaining 5 illuminated channels. The four points correspond to the true dark frame and 3 iterations with different luminance values. It is likely that scattered light is contributing to the offset of the total and passive spectra compared to the VBE in figure 1.10. However, when taking the difference between the total and passive spectra to obtain the FIDA spectra, the offset due to the scattered light is mostly subtracted out. Any residual effects would be present as nonzero signal in the FIDA spectra at large Doppler shifts ($\Delta\lambda$>5nm). For the data presented here, the effect is negligible.

To compare experimental FIDA signals with fast-ion distributions predicted by codes such as TRANSP, the FIDAsim code [21] is employed. The code is a synthetic diagnostic which predicts the active Dα emission, treating all relevant atomic physics, such as charge-exchange and atomic excitation processes. It requires an equilibrium reconstruction of the plasma along with electron density (n_e), electron temperature (Te), ion temperature (Ti), impurity density (n_{imp}), and toriodal rotation velocity (v_{rot}) profiles. The profiles inputted are typically spline fits to

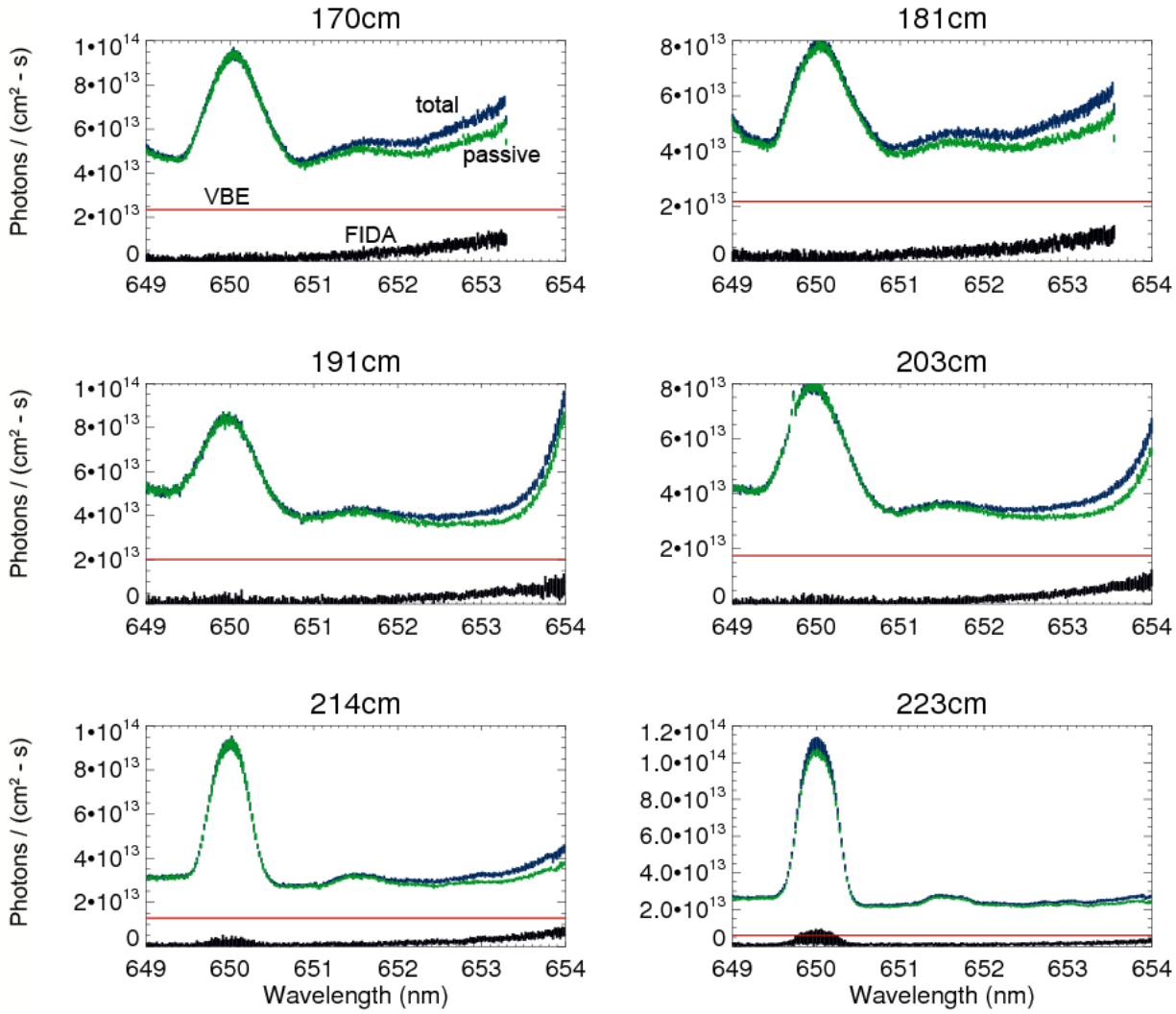

Figure 1.10.

experimental data for these quantities. Neutral beam parameters and the predicted fast-ion distribution function are also required for modeling. A typical FIDA/FIDAsim comparison first requires the calculation of the beam-ion distribution function from TRANSP with all instability and anomalous diffusion options turned off. With these options turned off, the resulting beam distribution function is a so-called "classical" distribution, i.e. a distribution of fast ions that slow-down and scatter through Coulomb collisions alone. The distribution is then used as input to the FIDAsim code which predicts the active Dα emission under the "classical" conditions free

of instabilities and anomalous diffusion. An extensive analysis of the 1st generation vertical FIDA signals during such conditions and comparisons with the predicted FIDA emission levels from the synthetic diagnostic can be found in [4]. Before proceeding to a similar analysis with the oblique system, a few considerations must be accounted for when comparing measured spectra with those predicted by the synthetic diagnostic code FIDAsim.

The first that will be discussed here is the modeling of the multiple chords that comprise a radial channel. Discussed in appendix A, the post-processing procedure of radiometric intensity calibrations of s-FIDA is sketched. One of the key differences between s-FIDA and its predecessor is that the former uses 3 fibers to collect signal at each radial location in the tokamak. Each of the 3 chords were designed to intersect the midplane at the same major radius, and the toroidal separation between adjacent chords is nominally 10cm. Unfortunately, at the time of writing, only spatial calibrations of the central-most view chords are available (due to constraints on the calibration equipment). So, for now, the spatial positions of the neighboring chords used in conjunction with FIDAsim are design values. As discussed earlier, the 3 fibers of each radial channel are vertically stacked at the focal plane of the spectrometer, and the signal from the 3 chords is binned vertically on the CCD chip. Binning consists of a summation of the CCD counts over each column of pixels, so each column is read-out as a single value of counts. When the radiometric calibration is applied to the raw CCD signal, the result is a single spectrum for each radial channel, which is the sum of the radiance collected by the 3 constituent chords. The same procedure must be applied to the synthetic diagnostic. Since FIDAsim outputs the active spectral radiance for each modeled view chord, the spectra are simply summed over the chords for each radial channel. The emissivity varies with position so accurate modeling of the geometry of all chords is necessary. The spatial positions of the central view chords are well

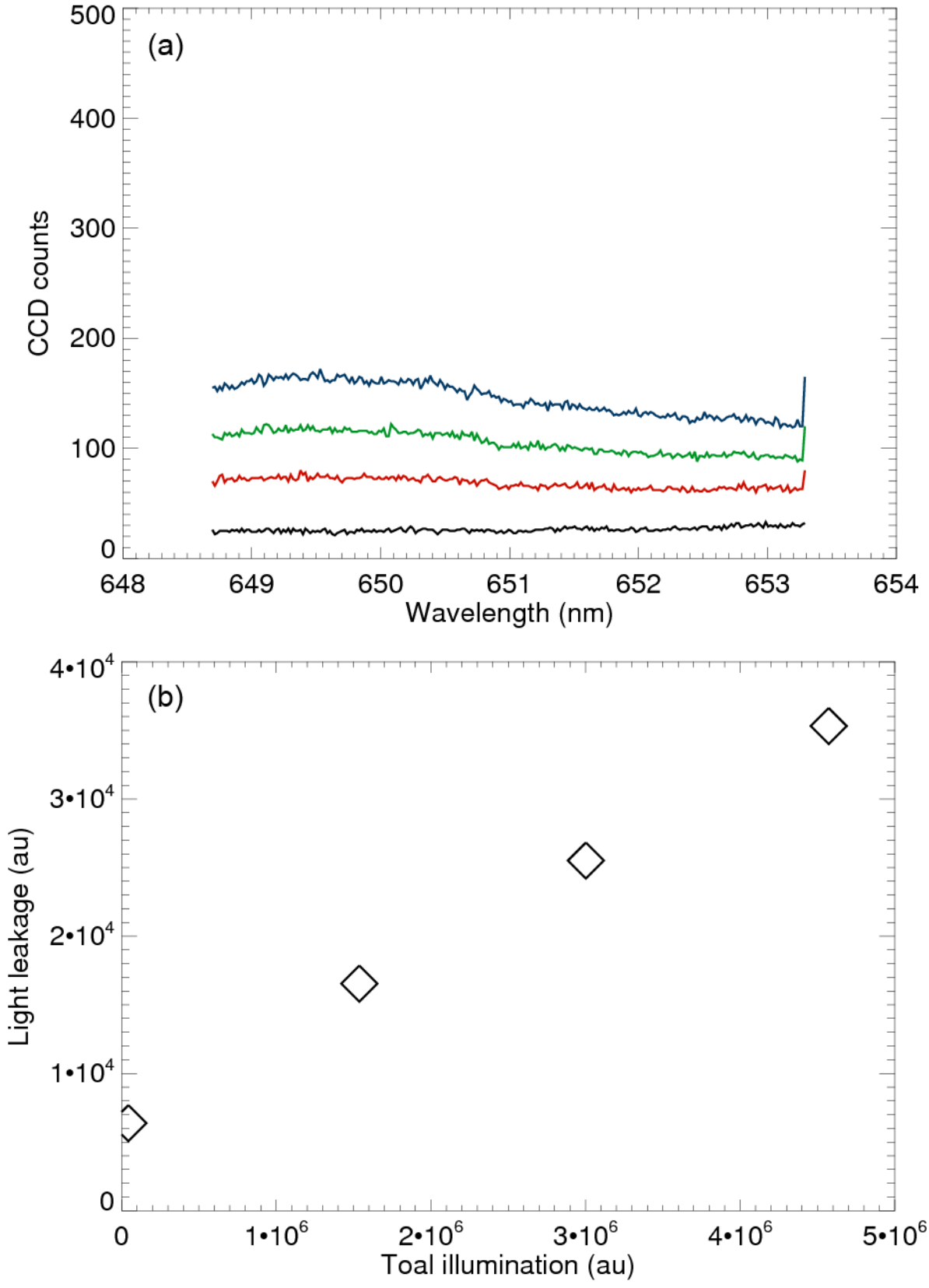
(a)
CCD counts
500
400
300
200
100
0
648
649
650
651
652
653
654
Wavelength (nm)
(b)
Light leakage (au)
4•10^4
3•10^4
2•10^4
1•10^4
0
0
1•10^6
2•10^6
3•10^6
4•10^6
5•10^6
Toal illumination (au)

Figure 1.11.

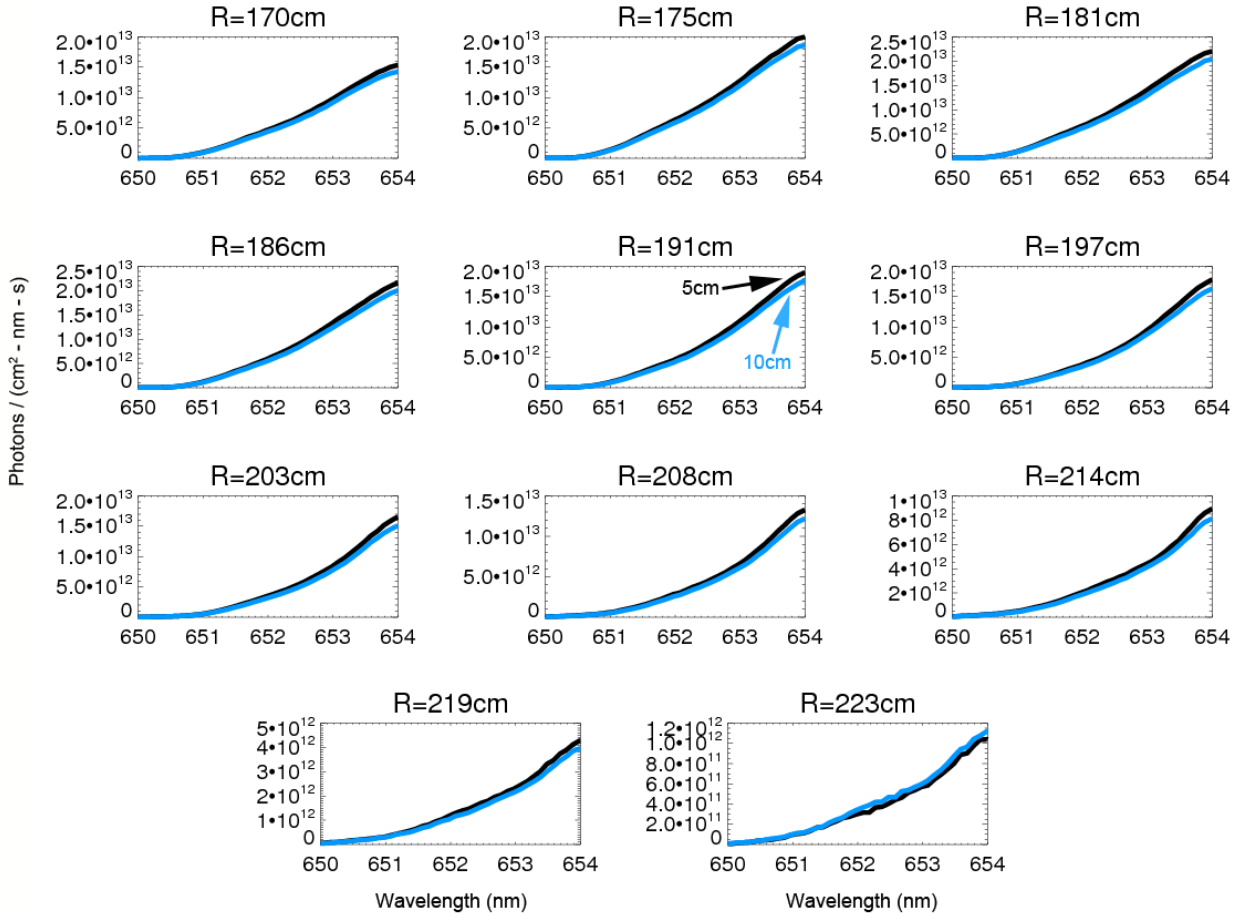

Figure 1.12.

known, but it is useful to test the sensitivity of the spectra on the position of the outer view chords. Comparative FIDAsim runs are presented in figure 1.12. The two cases incorporate different spatial separations between the central chords and the toroidally-displaced ones (5cm in black and 10cm in blue). Larger chord separation leads to a decrease in the spectral amplitude because of the finite width of the neutral beam; the emissivity falls off roughly Gaussian-like across the transverse axis of the beam. The 10% difference between the two spectra at each radial channel shown figure 1.12 motivates the necessity for improved spatial calibrations of all view chords. In the next part, we consider instrumental artifacts of the measured spectra that must be applied to the synthetic spectra for realistic comparisons.

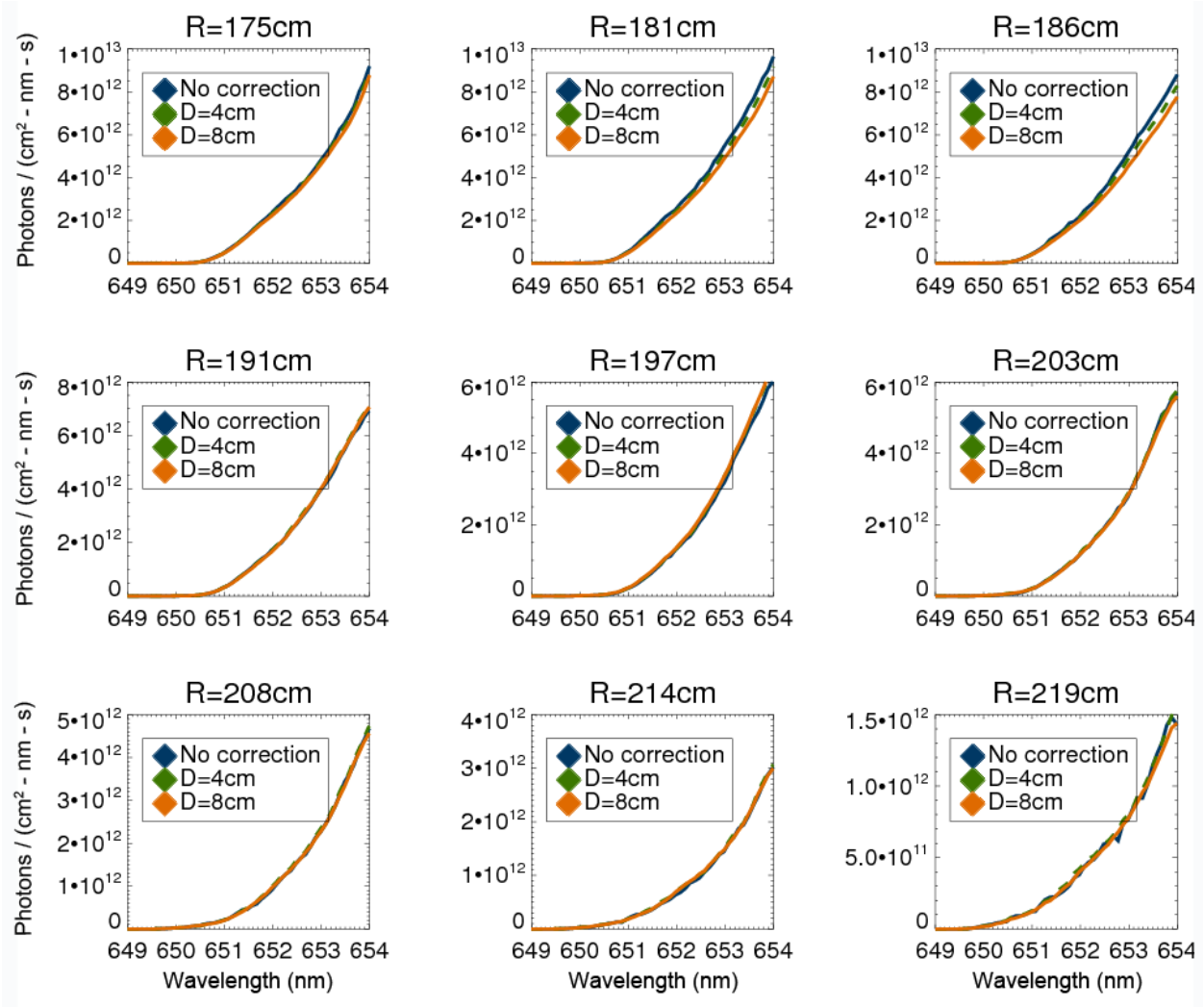

Figure 1.13.

Section 1.4.d. Instrumental corrections of synthetic FIDA spectra

FIDAsim models the active Dα emissivity and integrates the emissivity along each of the FIDA sightlines to yield spectra for direct comparison with measurements. However, during a standard calculation of the FIDA spectra, the FIDAsim code does not produce artifacts in the spectra due to instrumental effects. A true apples-to-apples comparison requires the simulated spectra to possess the same instrumental effects as the experimental ones. Two effects are

studied and presented here: 1.) modeling the finite size of the sightline and 2.) modeling the point-spread function of the detector. The first point addresses the issue of a finite collection volume. FIDAsim predicts the Dα emission (as a function of wavelength) on a 3D spatial grid encompassing the region of a neutral beam where the FIDA sightlines intersect. To determine the predicted measured Dα spectrum, a sightline is treated as a pencil ray and a line integral over the emissivity is performed through the grid along the trajectory of the sightline. The line-integrated Dα emission is binned into its various wavelength components, yielding the spectrum. However, a line integral is only an approximation to the actual extent of the viewing volume. The inclusion of the oblique viewing chords with midplane spot diameters of ~ 4cm prompted the question: how does the predicted spectrum change with collection volume size? One might expect that the measured spectra can vary depending on the spot size if spatial gradients exist in the emissivity profile. A post-processing routine is developed to investigate this. In the case of a line-integrated signal, the intersected grid elements are assigned weights according to the length of the line through the element. This weight will be referred to as the longitudinal weight; the weight assigned along the path of the light. Perhaps obviously, this longitudinal weight ensures that only light along the sightline contributes to the measured signal. With a finite spot size, if the active collection volume at the midplane is far from the lens and the spot size is not too big, the sightline can be modeled as a cylinder. The cylinder can be thought of as many pencil rays filling the cylinder's volume. The same procedure is followed by line-integrating along each pencil ray and calculating the longitudinal weight associated with the length of the line through each grid element. An additional factor must also be considered: conservation of etendue i.e. conservation of phase space. No matter what shape we use to model the finite-volume sightline, although the flux *density* of light rays (number of rays per volume element) may change along the axis of the

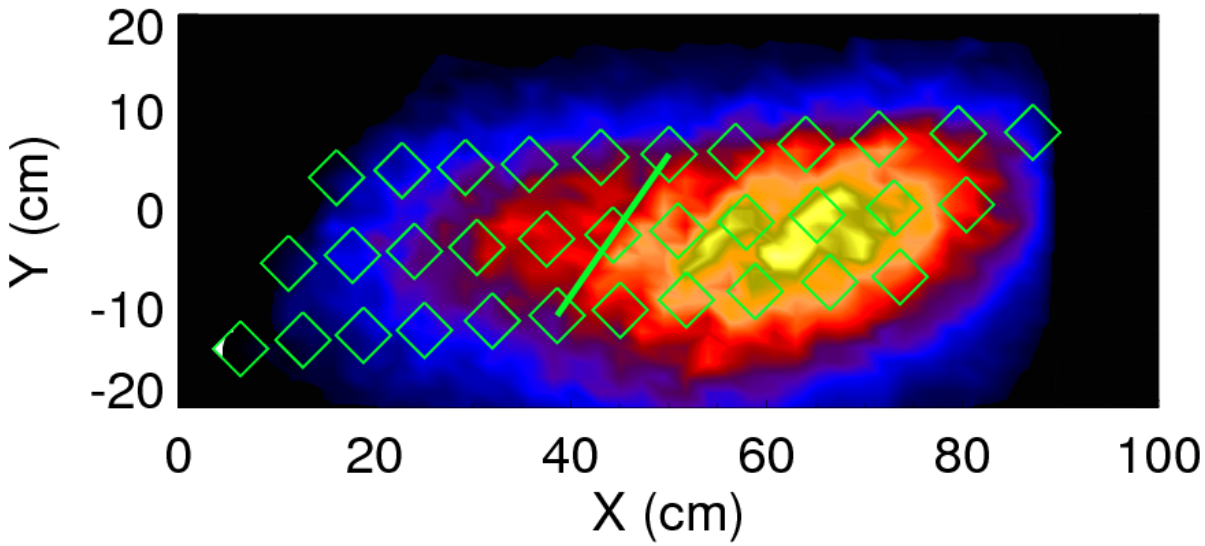

Figure 1.14.

sightline, the *total* flux (summed number of light rays through a cross section of the viewing cone) must remain constant. With a cylinder this is automatically achieved if the pencil rays are launched parallel to the axis of the sightline. The effect of the finite viewing volume on the spectra is shown in figure 1.13 for spot diameters of 4cm and 8cm. A comparison of the original line-integrated spectra (blue) and the corrected spectra for a 4cm spot diameter (dashed green) and unrealistically large 8cm spot diameter (orange) are shown for 9 radial channels. Clearly, for the example presented here, the finite spot correction leads to negligible modifications of the original spectra, even for the 8cm spot size which is twice the measured value for the oblique viewing system; apparently,spatial gradients in the emissivity profile are weak where the sightlines intersect the neutral beam. This is corroborated by the FIDAsim calculation of the emissivity. Figure 1.14 is a plot of the emissivity at the midplane predicted by FIDAsim. The origin corresponds to a point on the axis of the beam outside the last closed flux surface. The abscissa is the longitudinal distance along the beam's axis, and the ordinate is the horizontal transverse distance. The overlaid green diamonds indicate the spatial locations and approximate

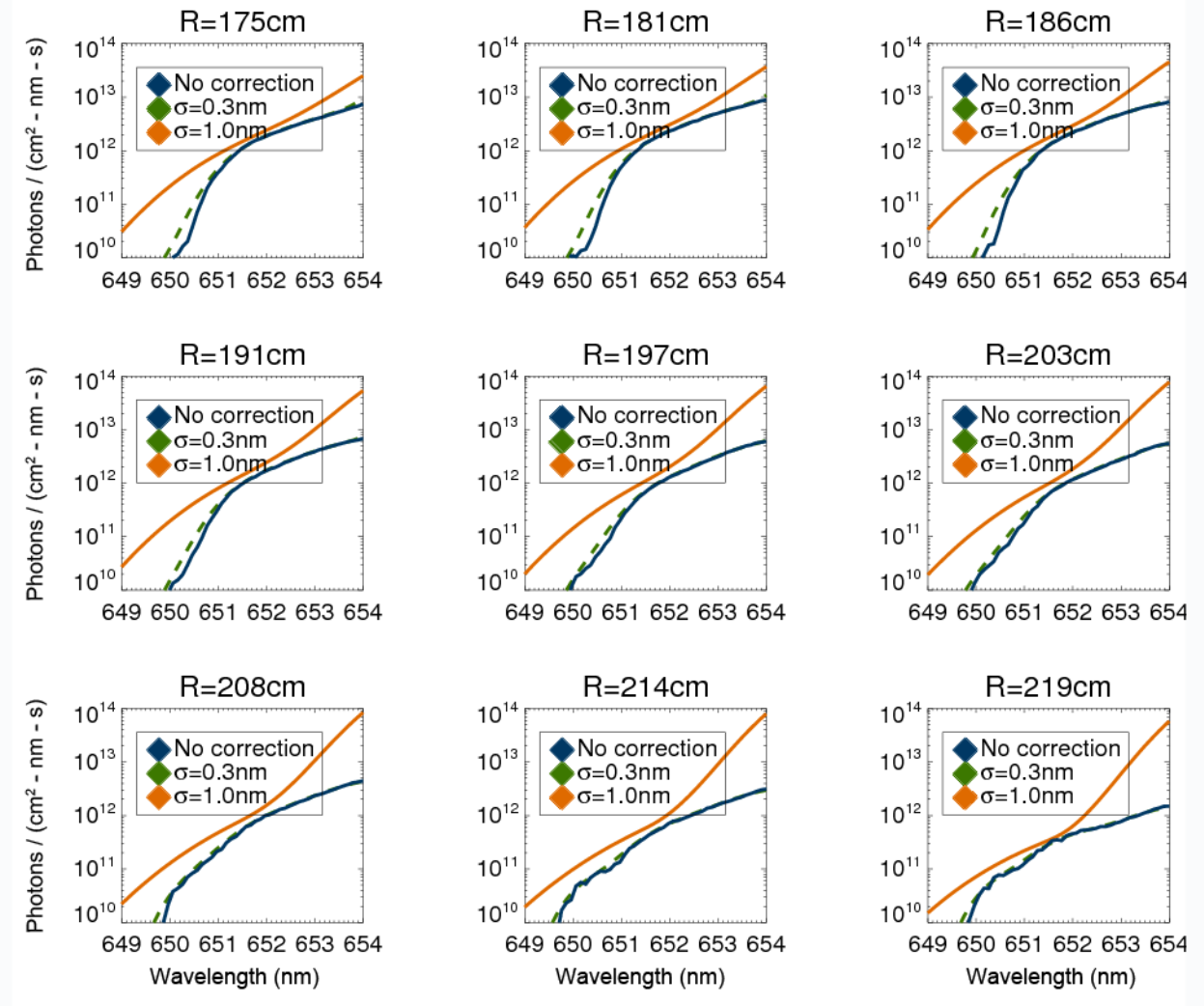

Figure 1.15.

spot size of the oblique sightlines at the midplane. Recall that each radial channel consists of 3 viewing chords; to guide the eye, the 3 chords corresponding to the R=191cm channel are connected by a line. The emissivity varies only slightly over the extent of a spot; the ratio of the standard deviation to the mean of the emissivity over a typical spot at the midplane is less than 15%. Again, it should be noted that this analysis is case specific; if the neutral deposition or fast-ion profile changes, the emissivity profile will change. In general, integration over a finite volume produces a reduced signal compared to the line integration technique since the density of the neutral beam is greatest at its axis and falls off transversely. The line integration technique is

performed along the axial trajectory of a sightline, which is designed to intersect the axis of the beam. A finite-volume sightline thus averages a smaller signal since it integrates a larger region around the axis of the beam.

The second point mentioned above (modeling the point-spread function of the detector) requires consideration of the instrumental broadening effect. Although spectral emission lines from cold sources are theoretically very peaked and narrow, a measurement can significantly broaden the spectral line due to imperfections in the instrumentation and limiting optical elements such as finite slit width. A detector has associated with it a point-spread function (PSF) and, when convolved with some impulse function (e.g. the actual spectral emission line), yields a smeared-out measurement. Theoretically, an optical system consisting of a single lens produces an Airy disc PSF of a point source. An experimental determination of the PSF for our FIDA spectrometers can be performed with simple Ne lamps. Since the temperature of the gas in the Ne lamp only reaches tens of eV, the thermal broadening of the spectral lines is negligible. Therefore, the shape of the Ne spectral lines measured by the spectrometers is an excellent proxy to the detector's PSF. Gaussian fits to the Ne spectral lines provide a very good approximation; in fact a cross-section through an Airy disc and a Gaussian curve scaled in amplitude and in volume produce very similar curves; their standard deviations differ by less than 5%. The standard deviation of the Gaussian curves fitted to the Ne spectral lines are ~0.3nm and a full-width half-max (FWHM) of ~0.7nm. For a true comparison between the experimental and simulated FIDA spectra, this Gaussian instrument response function should be applied to the predicted spectra. The effect of instrumental broadening is shown in figure 1.15. In general, a Gaussian instrument function tends to broaden the spectrum. However, as seen in figure 1.15, with a standard deviation of $\sigma = 0.3$nm, the instrument function negligibly modifies the original spectra. Larger

(unrealistic) values of σ produce more pronounced effects. The FIDAsim spectra and emissivity profiles presented in the remainder of this thesis will include the aforementioned instrumental corrections.

Section 1.4.e. Comparison between FIDA measurement and synthetic diagnostic

Next, a comparison of the measured spectra from the oblique FIDA system and the spectra predicted by the synthetic diagnostic will be presented for shot 146088. As discussed earlier, the first 1.6s provides a MHD-quiescent ELM-free period with low line-averaged density ($<3\times10^{19}m^{-3}$) and low neutral beam power (1.5MW). The fast-ion population is generated through the injection of one co-source firing continually at an injection voltage of 60kV. Three other sources are blipped on for 10ms each at 10%, 5%, and 5% duty cycle for FIDA and diagnostic purposes. With a time sequence of user-supplied EFIT equilibrium reconstructions and spline fits to plasma profiles, TRANSP evolves the plasma state (with instabilities and anomalous diffusion turned off) over the time range of interest. For our purposes, we set up TRANSP to predict the beam-ion distribution function at time t=1385ms, corresponding to a diagnostic neutral beam blip for the oblique FIDA system. The distribution function, averaged over the spatial extent of the plasma, is displayed in figure 1.16. The oblique FIDA spectra predicted by FIDAsim using the distribution function calculated by TRANSP along with the measured spectra are plotted together in figure 1.16. The experimental and simulated spectra can be directly compared only after absolute radiometric calibrations are applied to the measured spectra. The interested reader is referred to appendix A for details on the calibration procedure. Errors on the experimental FIDA spectra are determined from the standard deviations about the mean of the active and passive spectra as discussed earlier. Except for the core-most channel

(R=170cm), the agreement between the amplitudes of the simulation and experiment is rather poor. On the other hand, normalization of the simulated spectra to the experimental ones (dashed orange in figure 1.17) yield excellent agreement between the shapes of the spectra. Features and gradients in the distribution function largely dictate the shapes of the spectra, and the spectral shape has a weak dependence on the plasma parameters. It is instructive to compare the experimental and predicted FIDA emission profiles to help make an inference on the source of the discrepancy.

Recall eq. (1.3); the active FIDA emission depends on the reactivity $<\sigma v>$ and the product of the injected neutral density and the fast-ion density, $n_0 n_f$. Miscalculations of any of these quantities can lead to inaccuracies in the predicted FIDA emission. Emission profiles are generated by integrating the spectrum within some bandwidth. Figure 1.18 shows one such profile by integrating the spectra used to generate figure 1.17 over λ=651-653nm (E_λ=21-56keV). The measured profile (solid black, triangles) and simulated profile (solid orange, diamonds) disagree in magnitude by a factor of up to 2.2 at R=191cm. The reduced chi-square value calculated for the measured and simulated profile data is 6.9. It is possible to narrow the source of the error by analyzing the measured neutron rate compared to that predicted by TRANSP. According to TRANSP, the neutron rate during the time of interest is dominated by beam-plasma reactions (90% b-p, 9% b-b, 1% thermonuclear) and is proportional to the reactivity $<\sigma v>$ and the product of the fast-ion and plasma densities $n_f n_p$. TRANSP calculates the classical neutron rate taking measured plasma density profiles, measured electron temperature Te and ion temperature Ti profiles, and fast-ion distribution function calculated by NUBEAM. The agreement between the TRANSP model and an absolutely calibrated neutron measurement yields excellent agreement as seen in figure 1.19. The neutron agreement along with the spectral

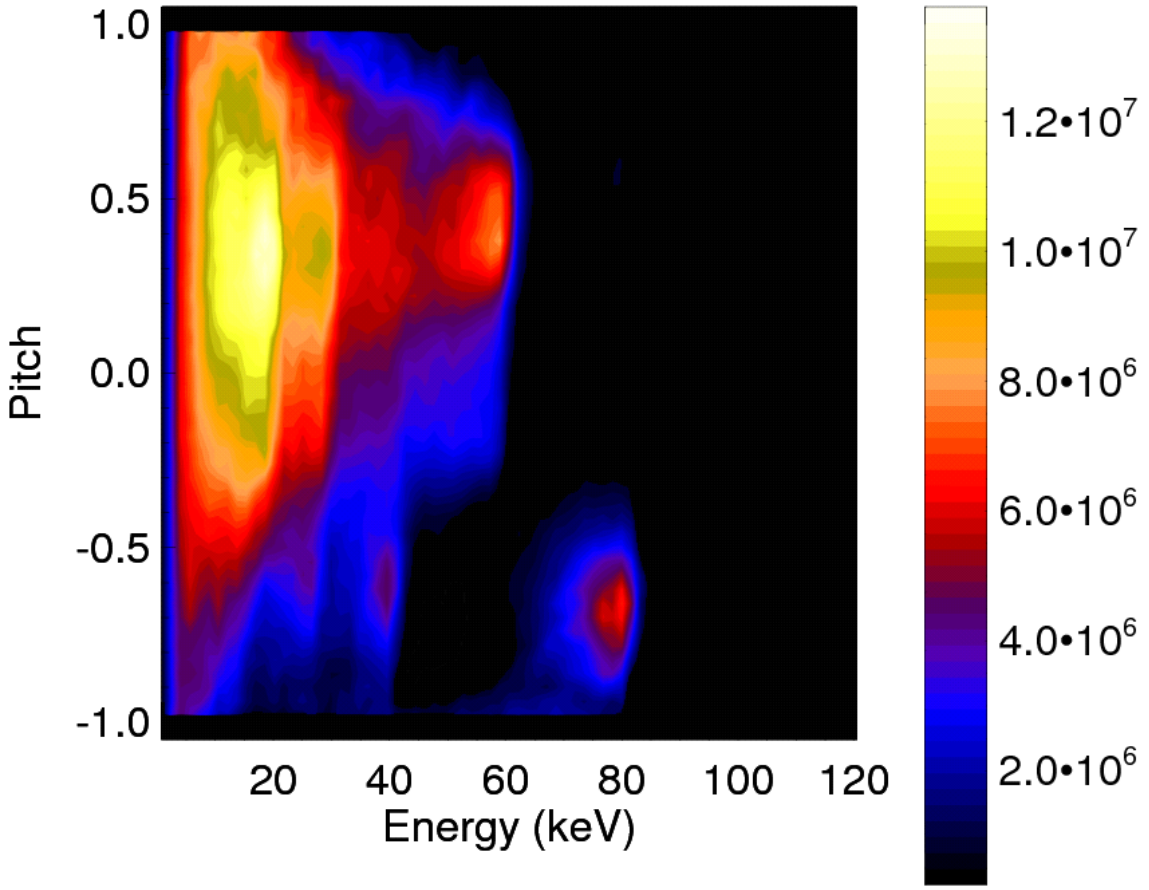

Figure 1.16.

shape agreement give us confidence that the measured plasma profiles and the NUBEAM fast-ion distribution function are consistent with the experimental profiles and neutron data.

Several other culprits could be the source of the discrepancy: mischaracterization of injected neutrals during the TRANSP/FIDAsim modeling, inaccurate model of oblique FIDA sightlines in FIDAsim, flawed radiometric intensity calibration of FIDA diagnostic. Possible mischaracterized injected neutral parameters include the geometry of the neutral beam, the species fraction of the full, half, and third energy components of the injected deuterons, and the reported injected power and/or voltage. Several variables characterize the geometry of the diagnostic neutral beam: injection angle, beam profile, divergence of the beam, location of the

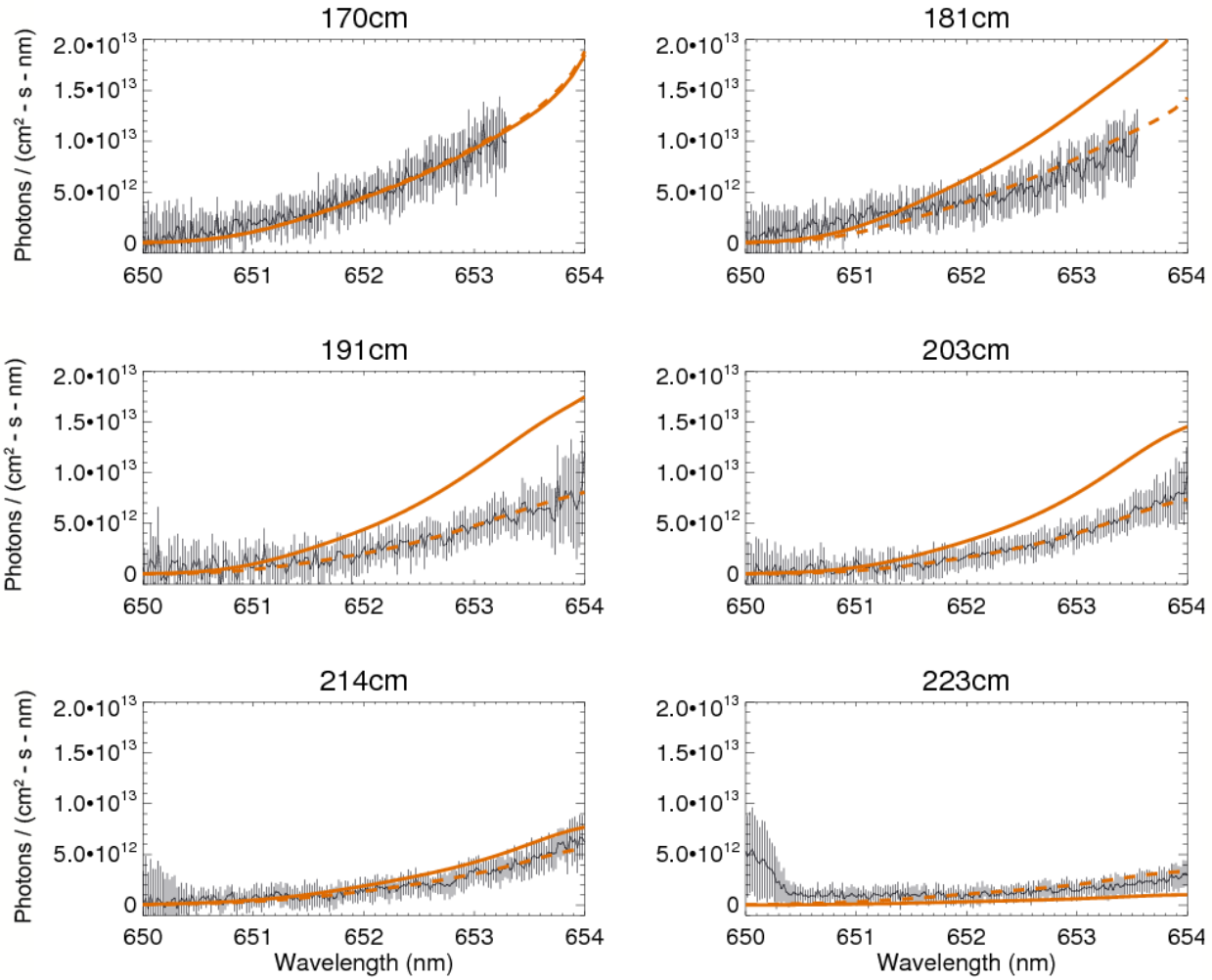

Figure 1.17.

ion source. Errors in the injection angle extrapolate to uncertainties in the velocity of the neutrals and in the spatial deposition of neutrals, affecting the neutral density profile and the charge-exchange reactivity. The beam profile governs the spatial volume from which FIDA integrates the active signal. Inaccuracies in the modeling of the beam profile would lead to errors in the predicted integrated emission. The neutral beam diverges as it travels through the plasma. Uncertainty in the beam divergence programmed into FIDAsim affects the modeled beam profile and the calculated neutral density. At the present time, measurements of the geometry of the DIII-D neutral beams have been performed for the 30 and 150 beamlines. The measurement

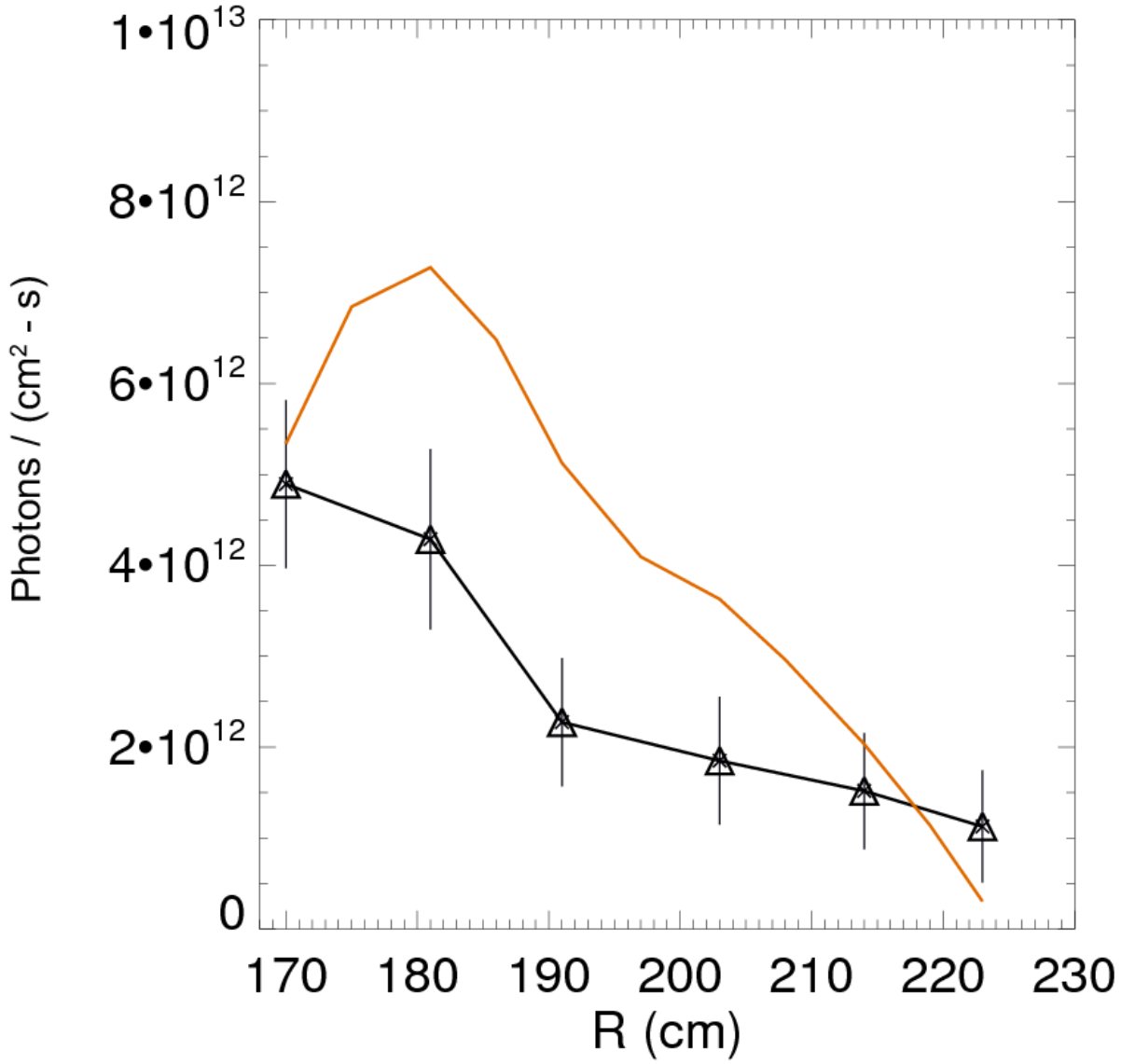

Figure 1.18.

involves a 2D imaging camera equipped with a bandpass filter to accept the Doppler-shifted beam emission [12]. Diagnostic port scarcity has delayed the measurement of the beam emission profile from the other two beamlines, 210 and 330, incidentally the beamlines utilized by the oblique and vertical FIDA systems, respectively. During the writing of this thesis, it was determined that location of the ion source within the 210 beamline (diagnostic beam used by the oblique system) programmed into FIDAsim was inaccurate [22]. To give an idea as to the

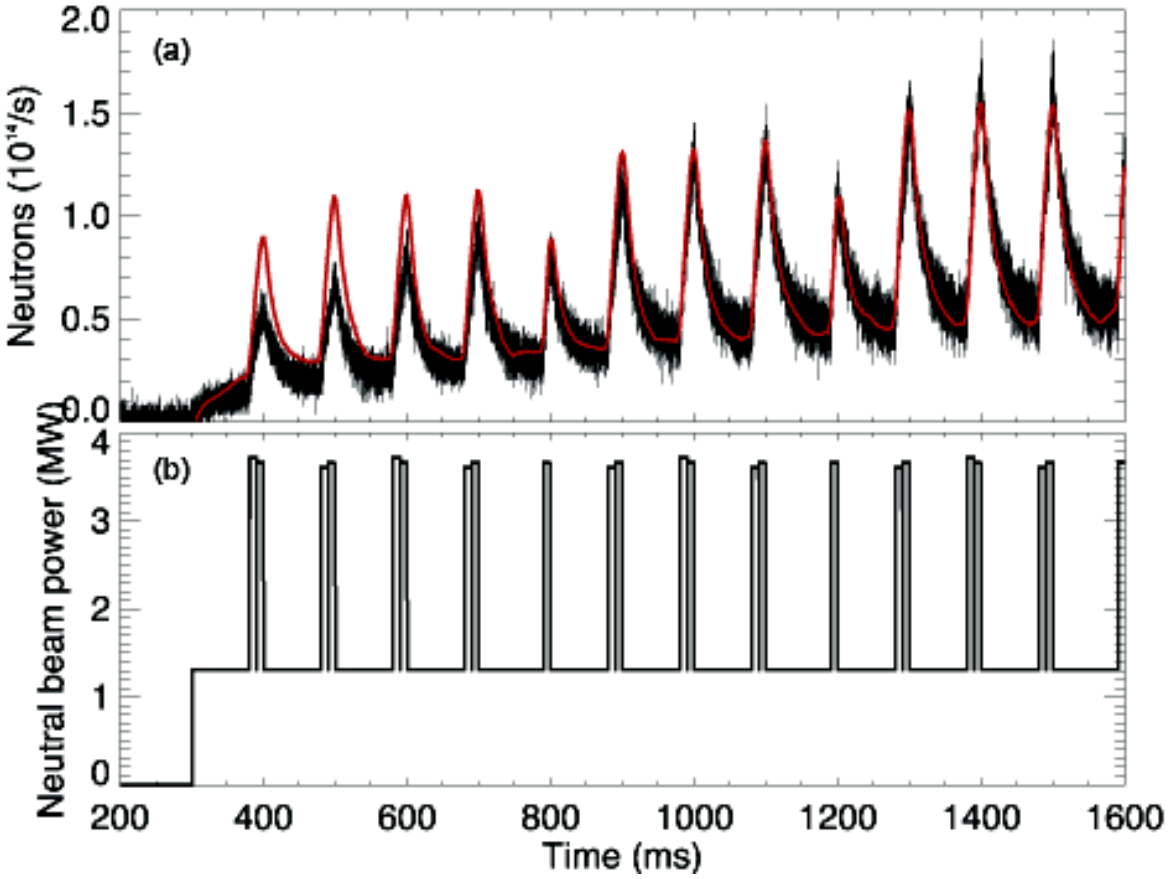

Figure 1.19.

sensitivity of the FIDA emission on this aspect of the beam geometry, a comparison of two FIDAsim runs is presented in figure 1.20. The difference in the runs is the location of the ion source within the beamline. The proximity of the ion source to the plasma determines how rarified the neutral gas is when it enters the plasma and thus affects the neutral deposition. For reference, the dashed black simulated profile is the same as the simulated profile presented in figure 1.18, and the profile in orange is generated by moving the ion source away from the plasma by 3.7m, consistent with its actual location [22]. The effect is significant, reducing the emission in a large fraction of the profile by 20%. The reduced chi-squared value between the new simulation and measured data lowers to 3.6, but the emission predicted by FIDAsim is still larger than most of the measured data by up to a factor of 1.9 at R=191cm.

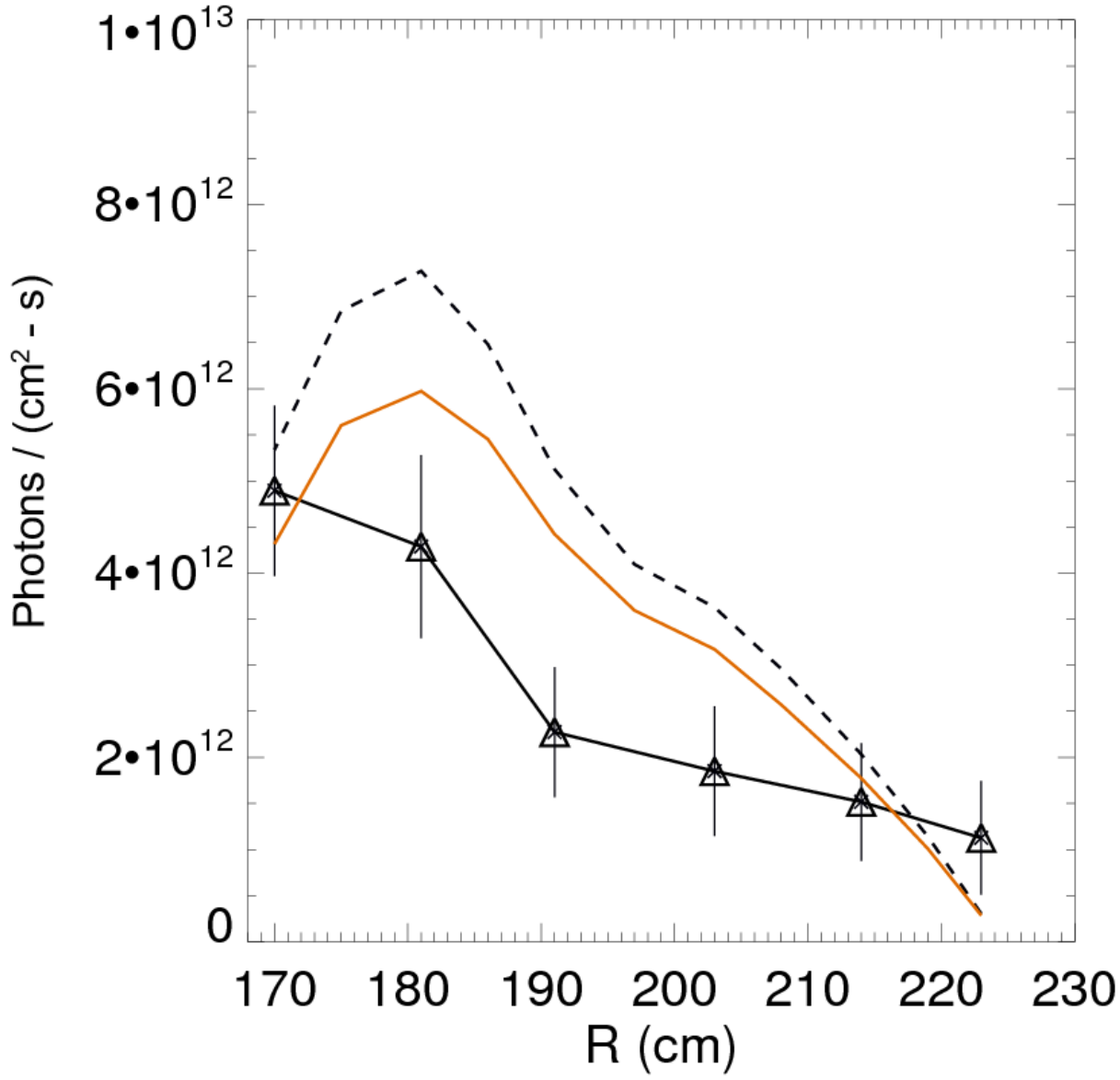

Figure 1.20.

Since the probability for charge-exchange depends on the relative velocity between the neutrals and the fast ions, erred species fractions introduce uncertainties in the fractional emission from each beam energy component. Additionally, inaccurate values for the injected power and voltage yield uncertainties in the number density and energy of injected neutrals. The implementation of the main ion CER diagnostic on DIII-D permits several key measurements of

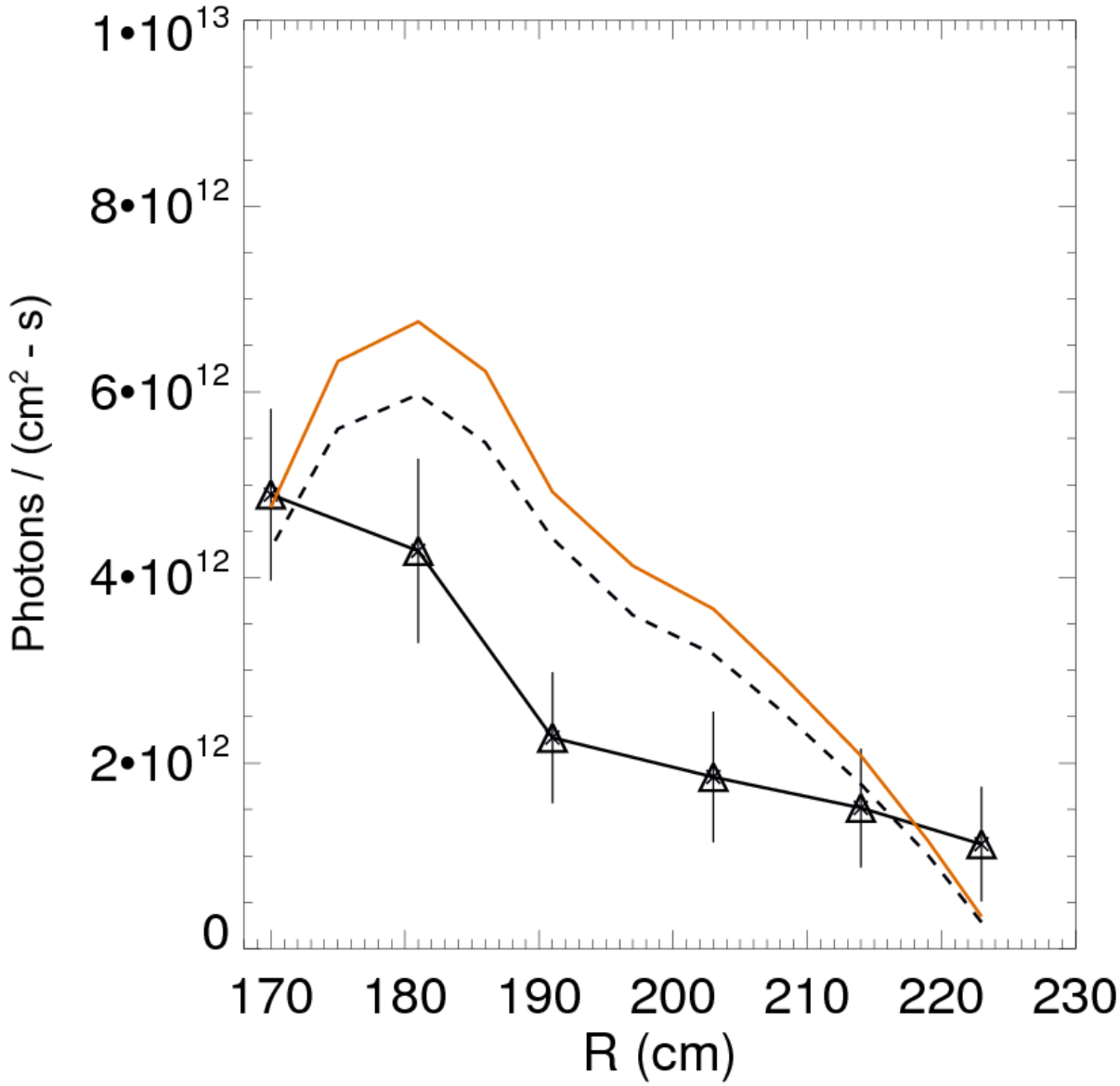

Figure 1.21.

the deuterium population through detection of the the full Dα spectrum [23]. Among them, analysis of the beam-emission component of the spectrum allows us to infer the species fractions, voltage, and power of the beam. The beam emission is light emitted by atomically excited injected neutrals. For a favorable viewing geometry, the light from beam emission is Doppler-shifted away from the cold edge neutral Dα emission and direct charge-exchange emission peaked at 656.1nm. The 3 energy components of the injected neutrals will possess

distinct Doppler shifts, resulting in wavelength-separated spectral features. The relative amplitude of the 3 spectral features is a direct measurement of the species fractions. In addition, the absolute amplitude of the beam-emission spectral components is proportional to the power of the injected neutrals. FIDAsim models the injected neutral process calculating the beam emission with user-supplied values of injected power, voltage, and species fractions, so the measured and predicted beam emissions can be compared to check the accuracy of the input values. If the value of the injected power inputted to FIDAsim does not match the actual experimental value, the measured and predicted spectral amplitudes will disagree. On shot 146088, it is found that, while the reported value for the injected power of the 210 FIDA diagnostic beam is acceptable, the calculated species fractions are not [22]. The species fractions inferred from the main ion CER system are (full, half, third = 0.55, 0.29, 0.16) while the calculated values are (full, half, third = 0.47, 0.29, 0.24). Recall that the oblique FIDA system views one of DIII-D's counter-Ip NBI sources, and it measures the blue wing of the Dα spectrum. Since the charge-exchange probability peaks for low relative velocity (between neutrals and fast ions), oblique FIDA is largely sensitive to co-Ip moving fast ions with moderate energy compared to the full injection energy. Therefore, a reduction in the full energy fraction of fast ions and an increase in either the half or third energy fractions would be expected to increase the emission measured by the oblique system. Comparative FIDAsim runs presented in Figure 1.21 confirms this is indeed the case, exacerbating our discrepancy. The measurements are the triangles plotted with error bars. The simulated profile with the original calculated species fractions is the dashed plot (for reference, the dashed profile in figure 1.21 is the same as the orange profile in figure 1.20). The profile with the species fractions inferred from main ion CER is the solid orange plot. The modification to the species fraction increases the reduced chi-square value between the

simulation and experiment to 5.8.

Despite our best efforts, agreement between the predictive synthetic diagnostic and measurements from the 2nd generation FIDA system have not yet been obtained. According to the charge-exchange proxy of eq. (1.3), the FIDA signal depends on 3 factors: the atomic radiative-collisional (charge-exchange cross-section and Dα emission) rates, the injected neutral density, and the fast-ion distribution function. Since these 3 factors depend on the plasma profiles, uncertainties in the profiles inputted to FIDAsim extrapolate to uncertainties in the predicted FIDA emission. A previous sensitivity study was performed (appendix of ref. [4]) where the dependence of the atomic rates, neutral density, and fast-ion density on plasma parameters such as electron temperature, electron density, and ion temperature profiles was investigated. It is found that variations in the electron density profile lead to compound effects on the FIDA emission; while the effect on the radiative-collisional rates is small, the neutral density and fast-ion density are strongly affected. An increase in the amplitude of the electron density profile by 20% reduces the FIDA emission in the core by approximately the same factor. The reason for the inverse relationship is because higher plasma density decreases the injected neutral deposition and decreases the fast-ion slowing-down time. Although variations in the electron temperature tend to affect the FIDA emission less than the electron density, the dependence is still significant; an increase in the electron temperature profile by 20% increases FIDA in the core by ~10%. The direct relationship results because an increase in the electron temperature increases the fast-ion slowing-down time. Variations in the ion temperature negligibly affect the FIDA emission; an increase of 20% in the ion temperature modify the atomic rates and neutral density by less than 5%. The sensitivity analysis did not explicitly study the dependence of the fast-ion density on the thermal ion temperature. However, since the fast-ion slowing-down time depends

very weakly on the thermal ion temperature, variations in the ion temperature should minimally affect the FIDA emission. The conclusion from these assessments is that the FIDA emission is most sensitive on the electron temperature and density profiles. DIII-D's electron cyclotron emission diagnostic is a quite robust measurement of the electron temperature profile even in the core. Our confidence in the measured Te profile is high; however, measurements of the electron density profile in the core have large uncertainties. Core measurements of n_e from the Thomson scattering system on DIII-D routinely leads to errors >20%. As stated earlier, variations in n_e approximately translate to direct inverse variations in the FIDA emission.

It is possible but unlikely that TRANSP modeled the fast-ion distribution function incorrectly. The absence of coherent MHD activity, the excellent agreement between the predicted and measured neutron rate, and the matching shapes of the measured and predicted FIDA spectra give us confidence that the model of a classical slowing-down distribution function is a realistic one. Although discrepancies exist in absolute comparisons between the synthetic diagnostic and the measurement, useful physics can still be derived. The shape of the FIDA spectrum dominantly depends on the velocity distribution of fast ions. Therefore, velocity-space diffusion of fast particles will reflect in the shape of the measured FIDA spectrum. Then, for example, one can compare the variations in the spectral shape over time to assess the evolution of the distribution function. Under certain conditions, it is reasonable to study relative changes in the FIDA emission amplitude to make assessments of the magnitude of the fast-ion density. If we have an acceptable estimate of the neutral density, we can divide the FIDA emission by it to obtain a quantity that is proportional to the fast-ion density. Assuming the atomic rates are reasonably constant at two times of interest (which is usually a good assumption since the rates are weakly sensitive on the plasma parameters), the change in the fast-ion density can be

compared relatively between the two times.

An assessment of relative changes to the fast-ion distribution function inferred from FIDA measurements are described in the following chapter. We are confident that the FIDA measurement captures a wealth of information on the distribution function, and in the following two chapters, FIDA data will be analyzed to gain an understanding of the fast-ion transport process during the sawtooth instability. Sawteeth strongly affect plasma confinement, so the instability is an optimal one to demonstrate the utility of the FIDA measurement.

CHAPTER 2. Velocity-space studies of fast-ion transport at a sawtooth crash in neutral-beam heated plasmas

Section 2.1. Introduction

Among the many internal instabilities inherent to tokamak plasmas, sawteeth are periodic core-localized MHD events occurring on large spatial scales (up to r/a = 0.5). The internal disruptive instability (more commonly referred to as the sawtooth instability) was first observed on the ST tokamak [24], where periodic collapsing of the soft x-ray signals coincided with the appearance of a q=1 magnetic surface. A theoretical explanation quickly emerged [25] associating the instability with a m/n = 1/1 internal kink mode. As the plasma current evolves, peaking on axis, the safety factor (q) on axis drops. During the existence of a q=1 surface, the plasma becomes unstable to the internal kink, and the region where q<1 experiences a rigid shift. Compression of the magnetic field lines near the q=1 surface occurs and reconnection between flux surfaces inside and outside the q=1 surface ensues until q>1 is restored on axis. The reconnection event redistributes the plasma, flattening the current profile, temperature profiles, and density profiles as a result. Calculations based on this theory over-predict measured collapse (crash) times of the sawtooth cycle by several orders of magnitude for large tokamaks. Numerous other theories have attempted to describe the collapse phase of the sawtooth instability, but none have been able to provide a unified picture for all devices and plasma conditions. Despite this, the experimental observations that are consistent across all tokamaks observing sawteeth are 1.) the coincident onset of sawtoothing behavior with the appearance of a

q=1 surface and 2.) comparable crash times O(10μs) despite machine size and plasma conditions. The interested reader is referred to ref. [1] for a concise overview of the sawtooth instability and the difficulties with its theoretical descriptions.

Not long after the first observations of the instability, various accounts of fast-ion redistribution during the sawtooth crash were reported. A sawtooth crash could apparently lead to internal redistribution of various species of fast ions: beam deuterium [26] [27], fusion-born proton and Helium-3 [28], and deuterium-tritium alphas [29] [30]. The velocity-space dependence of fast-ion transport by the sawtooth instability was studied previously on TFTR and TEXTOR. On TFTR, the Pellet Charge-eXchange (PCX) and alpha-CHarge Exchange Recombination Spectroscopy (α-CHERS) diagnostics obtained data on the redistribution of trapped and passing fast ions at a sawtooth crash [31]. A large depletion in the core passing-ion density was detected during a crash event with α-CHERS. The lack of core PCX data makes it difficult to assess the effect of sawteeth on the trapped energetic-ion population, but a broadening in the profile is observed. A more recent investigation on TEXTOR utilized a collective Thomson scattering (CTS) diagnostic during sawteeth to resolve the 1D fast ion distribution function for various angles with respect to the magnetic field [32]. It was determined that trapped energetic ions are less susceptible to sawtooth-induced transport than the passing population.

Differences between the effect of sawteeth on passing and trapped ions extends to the theoretical realm as well. Modeling of the redistribution of passing energetic ions invoking attachment to the evolving flux surfaces during the crash reproduces experimental results [29]. On the other hand, application of the flux-attached model to the trapped-ion population yields poor agreement with experiment [31]. To account for this difference, the theoretical works

invoke two distinct transport mechanisms: transport by flux-attachment [29] (dominant for passing particles) and transport by **E**×**B** drift [31] (dominant for trapped particles). However, it can be shown that mode-induced **E**×**B** drift and flux-attachment are cause and effect [33]; a particle experiencing **E**×**B** drift due to a time-varying magnetic field moves with the field on a fixed flux surface. Therefore, *any* particle closely situated near an evolving flux surface is prone to sawtooth-induced transport, but the frozen-in condition is broken by particles that experience strong toroidal drifts.

Motivation to study energetic-ion transport induced by the sawtooth instability on DIII-D is two-fold: 1) the FIDA diagnostic suite is well-equipped to resolve different regions of velocity space, making it possible to distinguish between trapped and passing particles, 2) performance and risk assessments of the operating conditions in future reactors (such as ITER) must be obtained; since sawteeth are well-known to cause transport of energetic particles, it is necessary to corroborate theoretical models with experimental measurements. In chapters 2 and 3, the ultimate goal is to motivate future work that will utilize the existing theories to forecast the effect of sawteeth on energetic particles in ITER discharges with $q<1$. In this chapter, experimental data of velocity-space resolved fast-ion signals during sawteeth on DIII-D is presented. Consistent with previous results, we observe stronger redistribution of passing fast ions compared to their trapped counterparts. A drift kinetic simulation is performed, and the results qualitatively agree with the observation that passing fast ions experience the greatest degree of redistribution. To remind the reader of the extensive theoretical work done in this subject, an abbreviated sketch of the important aspects of the theory will be presented. The theory associates the transport difference between passing and trapped fast ions to their magnitude of toroidal drift. A critical energy exists where toroidal drift plays an crucial role in the degree of transport. The

critical energy can be represented in velocity space, dictating a redistribution boundary. We show that changes in the measured energy spectrum of fast ions are consistent with a numerical calculation of the redistribution boundary. The chapter is organized as follows. In section 2.2 I present the experimental setup and FIDA data. Section 2.3 summarizes the results from two different simulations and includes an analytic sketch of particle drifts. Lastly, our concluding remarks can be found in section 2.4.

Section 2.2. Experimental setup and results

With its extensive suite of diagnostics, neutral beam injection system, plasma control system, and array of magnetic field shaping coils, the DIII-D tokamak [34] is a highly versatile and well-diagnosed machine. The focus of the first part of this section is an analysis of fast-ion data for similar DIII-D shots 141182 and 141195. Figure 2.1 is an elevation of the plasma cross-section for shot 141182 as calculated by the equilibrium reconstruction code EFIT [35]; the magnetic axis is R_{axis} = 1.72 m. The motional Stark effect (MSE) polarimeter [36] measures the pitch of the local magnetic field. MSE is utilized to constrain the safety factor (q) profile and equilibrium reconstruction. The dashed flux surface indicates the location of the q=1 surface (normalized toroidal flux $\rho \approx 0.3$) just before a crash. The plasma current Ip and toroidal field Bt are 1.3 MA and 1.9 T, respectively. In these discharges, Ip is directed counter-clockwise, and Bt is clockwise viewed from the top of the tokamak (so that the ion ∇B drift is downward). A time history of shot 141182 is shown in figure 2.2. The top trace is the electron temperature Te measured by the core-most electron cyclotron emission (ECE) [37] channel at the midplane. The middle trace is the neutron emission rate measured by a plastic scintillator [38] located about 30° above the midplane. The bottom trace is the fluctuations of the magnetic field measured by a Mirnov coil

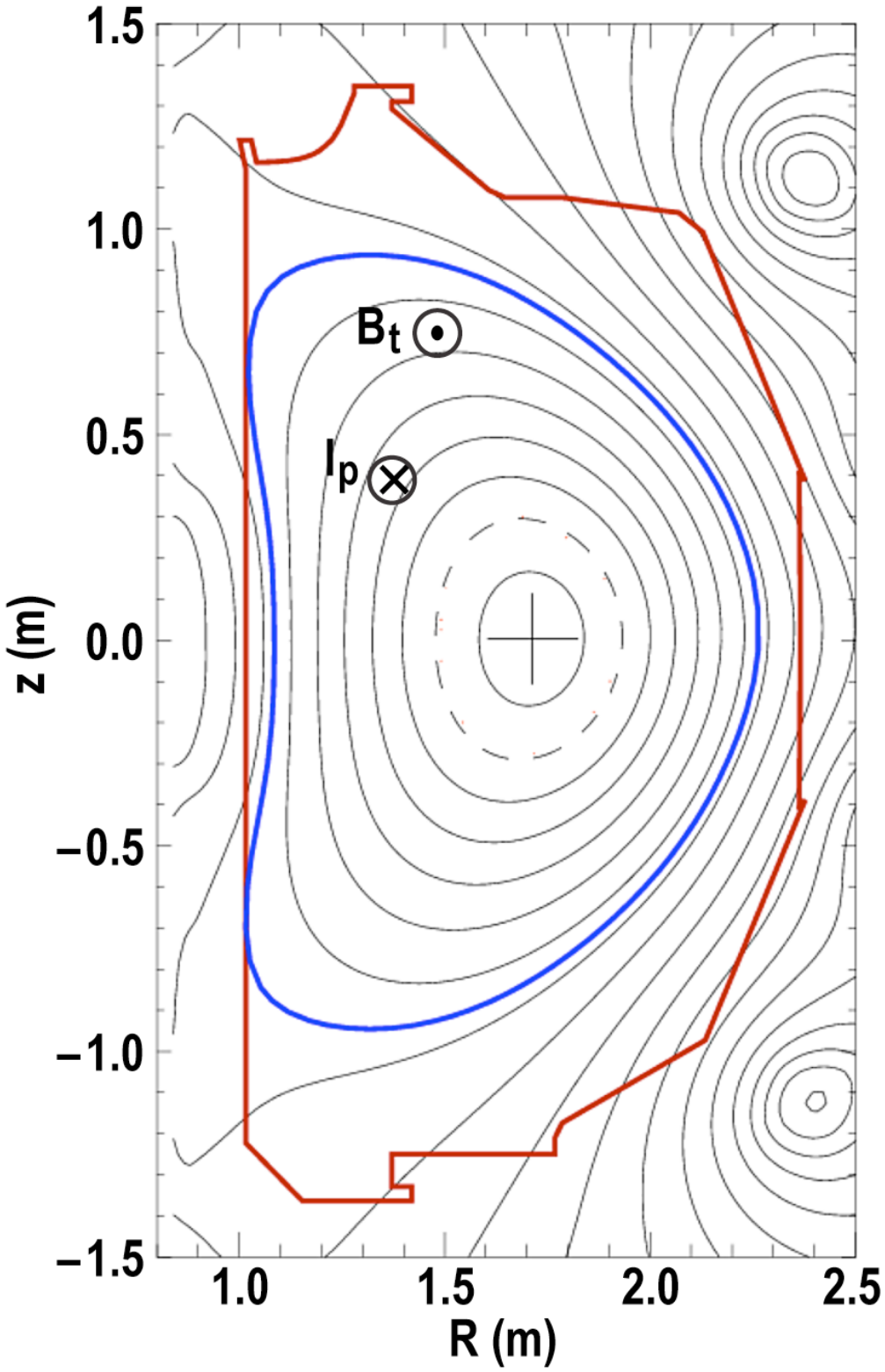

Figure 2.1

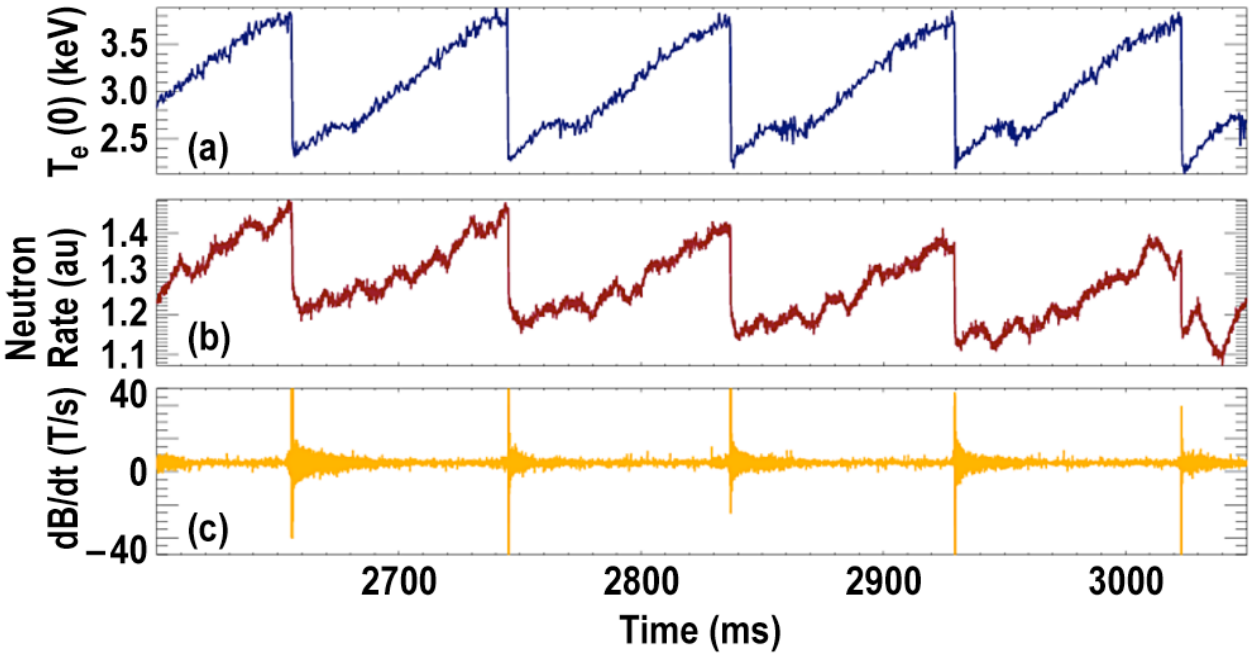

Figure 2.2.

[39] at the midplane. The average sawtooth period and amplitude (defined as $|\,Te^{postcrash} - Te^{precrash}\,| \,/\, Te^{precrash}$), and determined by the central ECE channel) are 85±5 ms and 0.35±0.02, respectively. Precrash and postcrash plasma profiles are plotted in figure 2.3. Ion temperature, toroidal rotation velocity, and main impurity (carbon) density are inferred from the charge-exchange recombination (CER) diagnostic [11]. The precrash and postcrash profiles are generated by averaging 10 ms before/after five consecutive sawtooth crashes. Random errors are calculated using the ensemble standard deviation. The fast-ion population is generated through deuteron neutral beam injection at an injection voltage of 75 kV. Four neutral beam sources are modulated on and off for diagnostic background subtraction and for the purpose of reducing the overall power to keep the discharge in L-mode. Sawtooth repeatability is necessary for fast-ion profile reconstruction prior to and following a crash. Long time domains (≈1 s) of uniform sawteeth are produced in order to obtain average precrash and postcrash profiles with sufficient statistics. During the sawtoothing portion of all discharges discussed here, no other MHD

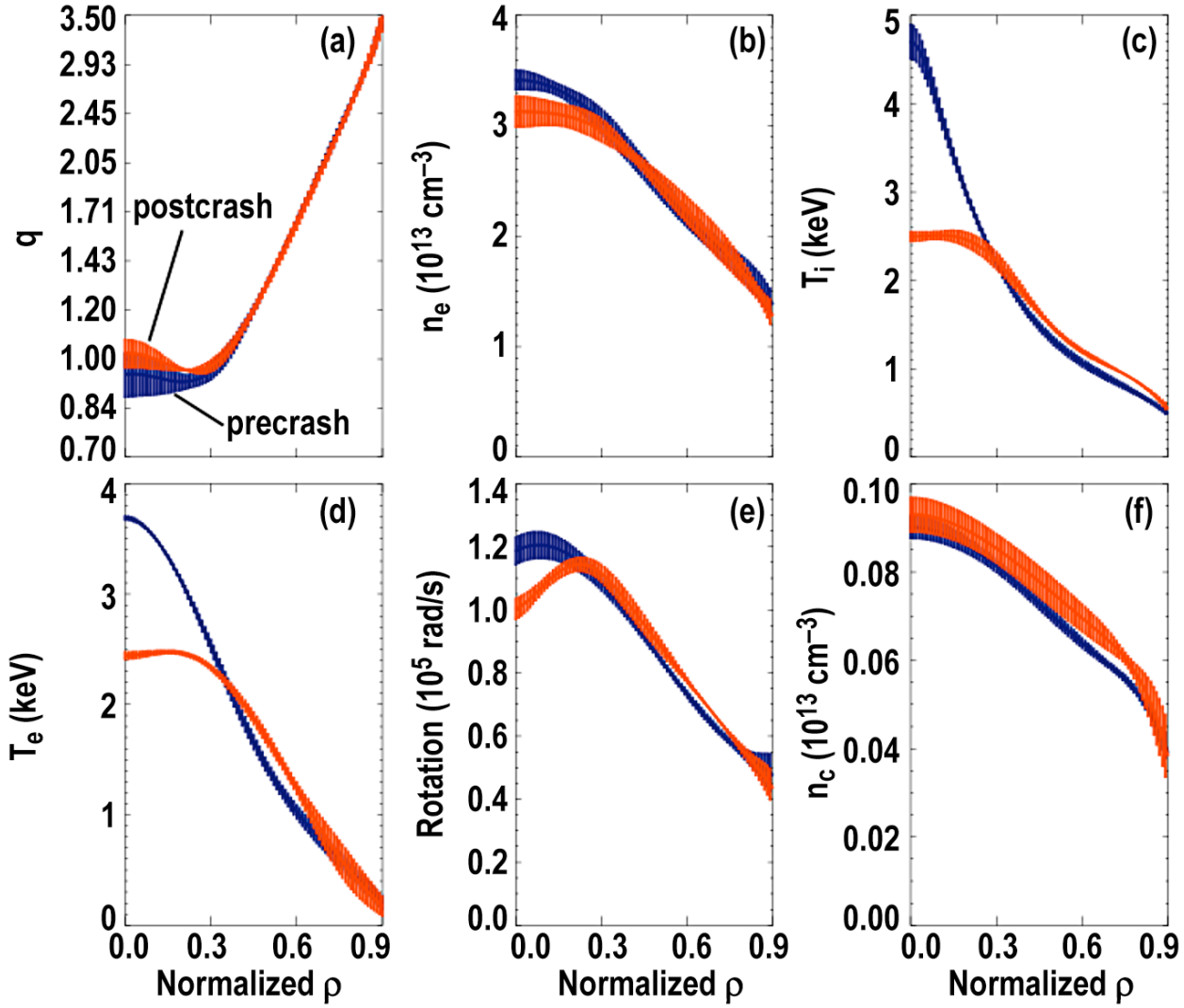

Figure 2.3.

activity such as Alfvén eigenmodes, fishbones, or tearing modes is detected.

DIII-D has an extensive fast-ion diagnostic suite that probes different regions of phase space. Fast-ion deuterium-alpha (FIDA) is the main diagnostic technique used in this chapter to measure the confined fast-ion profiles. Data from the vertical, oblique, and imaging systems will be presented here. Although FIDA integrates large regions of velocity space, the viewing geometries of the three systems skew the coverage differently. Figure 2.4 shows the weight functions that represent the contribution to the FIDA signal for the specified spectral integrations that will be used later to generate fast-ion profiles. Comparing the three, the weight function of

the vertical system is nearly symmetric about particle pitch of zero and strongly weighted about zero. The oblique system is heavily weighted toward large positive values of pitch, while 2D FIDA weights large negative values of pitch most heavily. The sign of the pitch indicates the direction of the particle parallel motion with respect to the Ip direction, where negative values indicate opposite direction to Ip. The overlaid dashed lines indicate fast ion trapped/passing boundaries that are calculated using a guiding-center orbit integration tool (see appendix of ref. [40]). These plots demonstrate the practicality of using the three systems to investigate the different dynamics of fast ions with varying orbit types.

In order to obtain high quality fast-ion signals, the discharges are chosen to be low-density L-mode deuterium plasmas. The signal-to-noise ratio of the FIDA signal is poor for line-averaged densities above $\sim 7\times10^{19}$ m^{-3}, and edge-localized modes (ELMs) introduce scattered light into the diagnostic, contaminating the spectra. In addition, simultaneous data acquisition during the same shot was desired for the two spectroscopic systems. Therefore, careful beam programming must be employed; otherwise, the vertical system's diagnostic beam can contaminate the oblique system's signal (and vice versa), inhibiting proper background subtraction. The beam programming on shot 141182 was set up so the beams were interleaved with intervals where both diagnostic beams are off for background subtraction. Average precrash and postcrash spectra are generated by averaging over many sawtooth cycles. For the vertical and oblique systems, spectra from various radial locations within the first and last 10% of each sawtooth cycle are chosen. Obtaining the desired FIDA spectra requires a background subtraction procedure described in ref. [5] and shown schematically in figure 2.5. An ensemble of total (beam on) spectra and background (beam off) spectra are collected for precrash and postcrash phases. The average precrash and postcrash FIDA spectra are calculated by subtracting

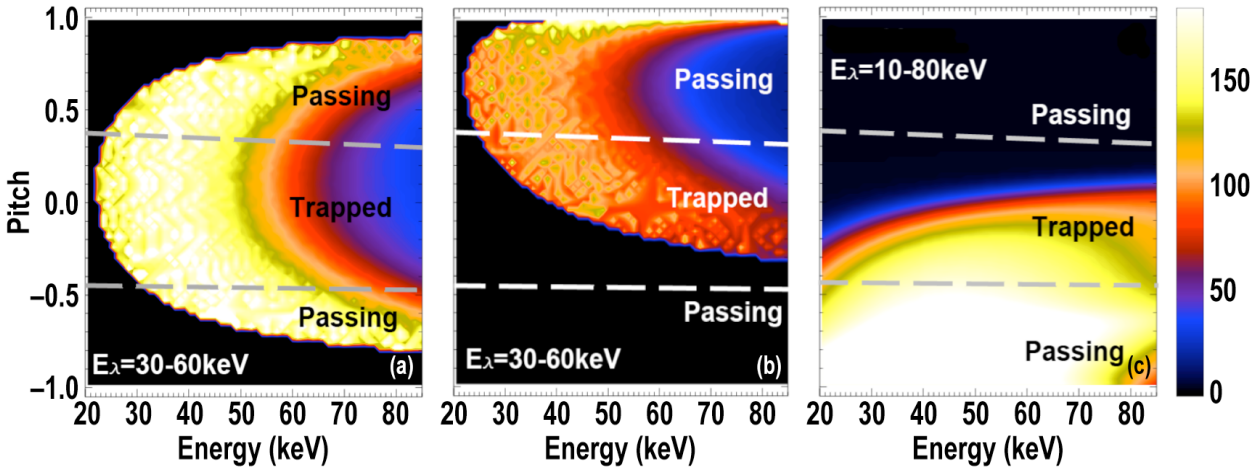

Figure 2.4.

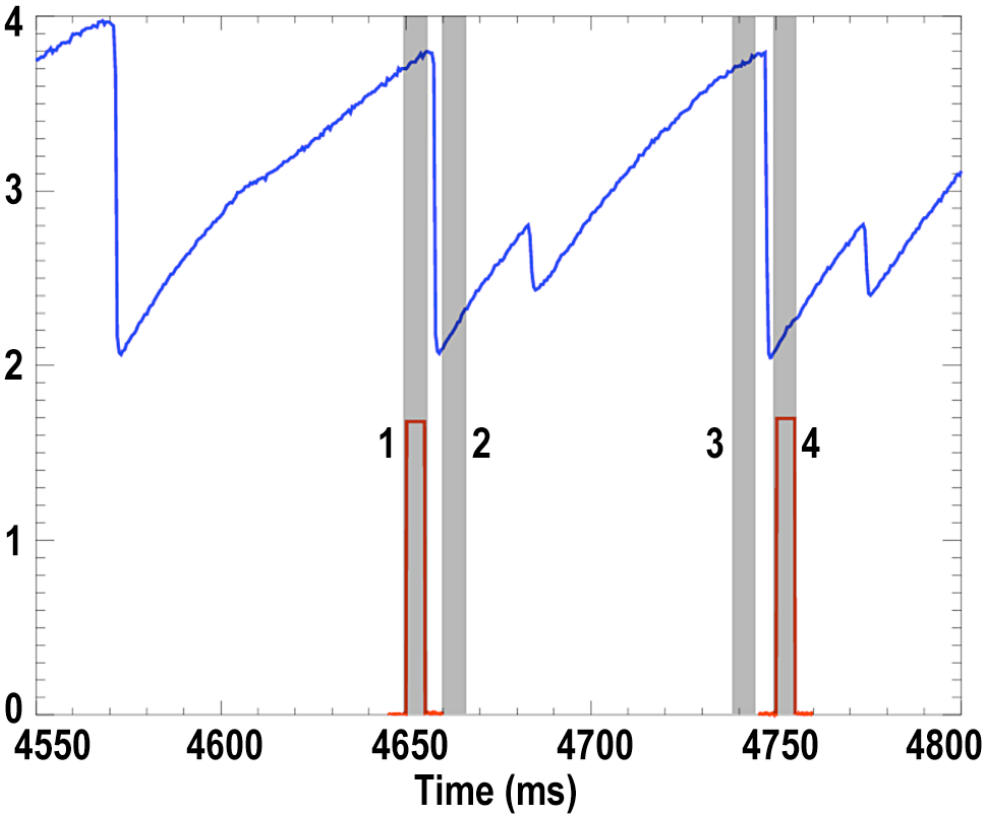

Figure 2.5.

the average background spectra from the average total spectra. This subtraction technique assumes the background $D\alpha$ signal is insensitive to the crash event. However, it has been observed that a sawtooth crash can cause changes in the background $D\alpha$ signal [5] . On shot 141182, a passive $D\alpha$ filterscope indicates that the background signal jumps less than 10%

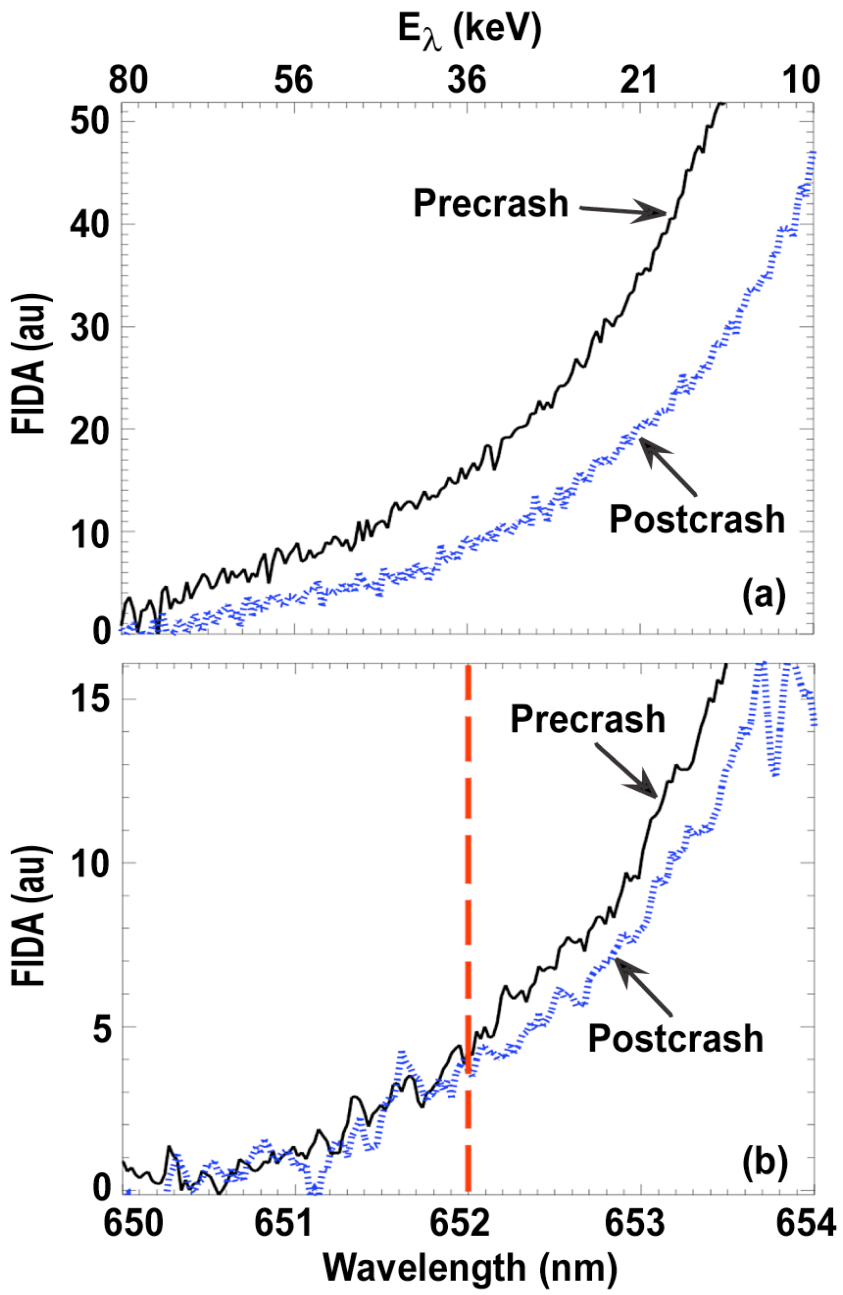

Figure 2.6.

following a crash. Spectra from the oblique and vertical systems for a radial chord intersecting the midplane at R=186 cm are shown in figure 2.6. Random errors are represented as the ensemble standard deviation from averaging. The average error in the vertical spectra is ~20% of the signal and ~10% in the oblique spectra. Evidently, data from the oblique FIDA system indicate that ions in the entire measured spectral range are redistributed, while there appears to

be an energy cutoff in the redistribution measured by the vertical system. The dashed vertical line (λ=652 nm, E_λ=36 keV) indicates the maximum Doppler shift where deviations between the precrash and postcrash spectra are observed by the vertical system.

Fast-ion profiles are generated by integrating the spectrum from each radial chord over a wavelength range corresponding to E_λ of 30–60 keV. The 2D imaging system was not configured for shot 141182, so a repeat shot 141195 was taken. For the imaging system, the bandpass filter provides *in situ* energy integration, and for shot 141195 the E_λ band is ~10–80 keV. An ensemble of integrated emission values at each radial location is generated during precrash and postcrash phases of several sawteeth. With the ensemble of integrated emission values at each spatial location, average values and standard deviations for the precrash and postcrash phases can be calculated. The ensemble of integrated emission points for the precrash and postcrash phases includes both beam-on and beam-off signals. The FIDA signal for one radial location is found by subtracting the average beam-off signal from the average beam-on signal, and this is done for both precrash and postcrash phases. An average precrash profile and an average postcrash profile are then generated, and these are used to assess the average redistribution induced by a crash. These values are then divided by the local neutral density to produce profiles which are approximately proportional to the fast-ion density. The neutral density calculation approximates the ionization cross-section given plasma density, plasma temperature, plasma toroidal rotation, and impurity density profiles. The profiles are spline fits to experimental measurements. In addition to the profiles, the neutral density calculation also requires values for the injected neutral beam power and the full, 1/2, and 1/3 energy species fractions. Errors in the profiles, reported injected power, and species mix propagate to errors in the calculated neutral density. The dependence of the neutral density uncertainty on the errors of the input parameters can be

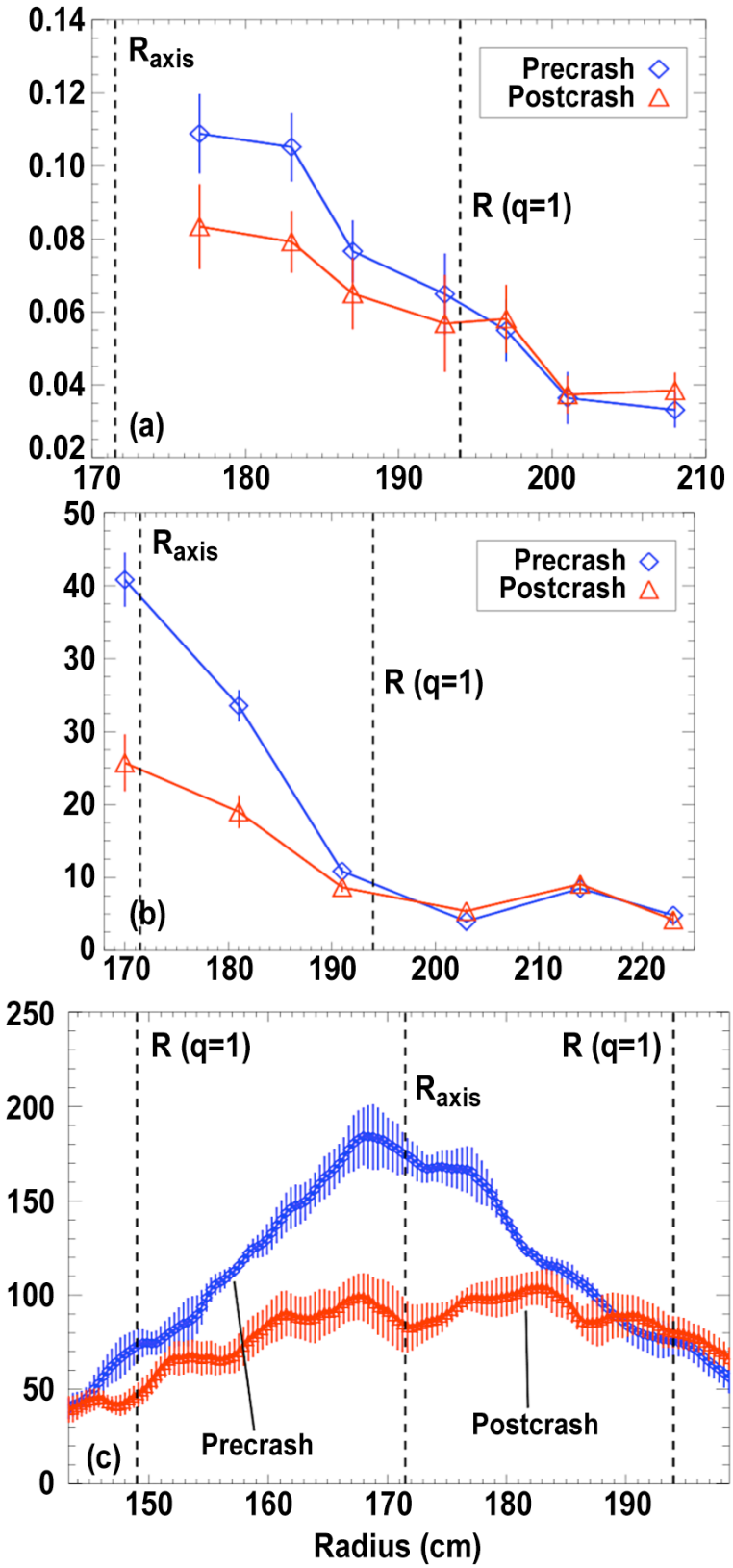
0.14
0.12
0.10
0.08
0.06
0.04
0.02
170
180
190
200
210
R_axis
R (q=1)
Precrash
Postcrash
(a)
50
40
30
30
20
10
0
170
180
190
200
210
220
R_axis
R (q=1)
Precrash
Postcrash
(b)
250
200
150
100
50
0
150
160
170
180
190
R (q=1)
R (q=1)
R_axis
Precrash
Postcrash
(c)
Radius (cm)

Figure 2.7.

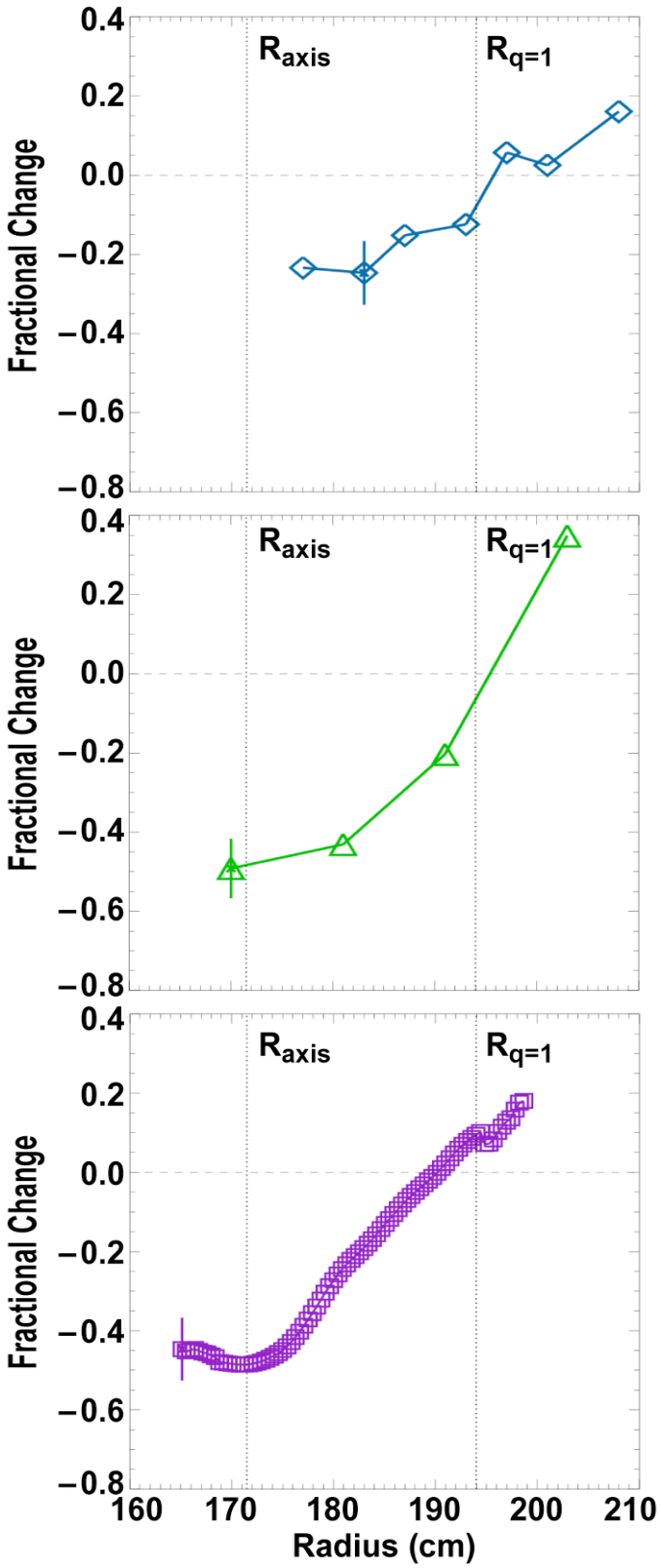
0.4
0.2
0.0
−0.2
−0.4
−0.6
−0.8
Fractional Change
R_axis
R_q=1
160
170
180
190
200
210
Radius (cm)

Figure 2.8.

determined by independently adjusting the parameter values. Out of all the plasma profiles, the neutral deposition is most sensitive on the plasma density profile. A reduction in the plasma density profile by 10% negligibly affects the neutral density at the edge but increases it in the core by 10%. Inaccurate plasma density profile modeling can lead to unsystematic uncertainties in the calculated neutral density. A reduction in the injected power by 10% reduces the neutral density by 10% uniformly across the beam trajectory. Fortunately, uncertainty in the reported injected power value is a systematic error which does not affect relative comparisons. A reduction in the full-energy species fraction by 10% negligibly reduces the neutral density by 5% uniformly across the beam trajectory. Therefore, uncertainties in the plasma density profile are likely the largest source of error. In the cases studied here, errors in the electron density profile are determined by a Monte Carlo method and yield values of less than 10% across the profile.

Figure 2.7 shows the average precrash and postcrash fast-ion profiles from the vertical, oblique, and 2D FIDA systems. It is clear from these plots that there is a large depletion in the core fast-ion density induced by a sawtooth crash. Atomic cross-sections and collisional rates complicate absolute comparisons of the fast-ion profiles among the different systems, so we resort to relative comparisons. A simple fractional change calculation is used to compare the levels of transport during a typical sawtooth crash. Here, the fractionnl change is defined as,

$$f \equiv (\,postcrash\ signal - precrash\ signal\,)/(\,precrash\ signal\,) \qquad (2.1)$$

Figure 2.8 is a plot of f versus major radius R for the three systems. Evidently, the magnitude of the redistribution is different depending on the type of fast-ion orbit detected. We see from figure 2.8 that a larger drop is experienced by the fast ions detected by the oblique and 2D

systems compared to those detected by the vertical system. 2D FIDA and the oblique array (sensitive to mostly counter-current passing and co-current passing ions, respectively) measure a similar percentage drop (~50%), which is significantly greater than the reduction (~25%) measured by the vertical system (sensitive largely to trapped ions).

Interpretation of changes in the FIDA spectra is complicated. FIDA radiation emitted by a volume in the plasma is approximately proportional to $n_f n_n <\sigma v_{rel}>$ where n_f is the local fast-ion density, n_n is the local neutral density, and $<\sigma v_{rel}>$ is the relevant average radiative-collisional rate (charge-exchange cross section and probability for $D\alpha$ emission). Since n_n and $<\sigma v_{rel}>$ depend on plasma parameters such as electron temperature Te, ion temperature Ti, electron density n_e, toroidal rotation velocity v_{rot}, and impurity density n_c, it is conceivable that any of these quantities can contribute to changes in the measured FIDA signal at a sawtooth crash. To estimate the contribution of changes in the plasma profiles on the measured FIDA signal during a sawtooth crash, we perform forward modeling with the FIDAsim code [21]. First we generate equilibrium reconstructions using EFIT just before and just after a typical sawtooth crash. Profiles are then fit to experimental data for Te, Ti, n_e, v_{rot}, and n_c. Next, we model the precrash and postcrash fast-ion distribution functions using the NUBEAM module [7] of TRANSP [8]. NUBEAM calculates the guiding-center drift orbit during the slowing-down process, handling various collisional and atomic physics. Among the outputs, the distribution function is calculated assuming toroidal axisymmetry. Although TRANSP includes the option to enable a generalized Kadomtsev sawtooth model (described later), for the following analysis, the model is not used. This is appropriate for this sensitivity analysis since we are only concerned with the effect of the plasma profiles on the FIDA signals. Finally, the equilibrium data, plasma profiles, and distribution functions are used as inputs to the

FIDAsim code. The simulation predicts a fractional change in $n_n \langle \sigma v_{rel} \rangle$ of $0 > f > -0.15$ in the core channels of the oblique and vertical FIDA profiles during a sawtooth crash assuming no fast ion loss. To estimate f of the fast-ion density, we assume the FIDA signal is exactly proportional to $n_f n_n \langle \sigma v_{rel} \rangle$ and the fractional change of $n_n \langle \sigma v_{rel} \rangle$ is –0.15. Under these assumptions, the fractional change of n_f measured by the oblique system is –0.41, and –0.12 measured by the vertical system. Similarly for 2D FIDA, modifications to the plasma profiles during the sawtooth crash can lead to observed changes in the measured FIDA profile. Furthermore, the average thermal ion temperature in the core just before a crash is 4.7 keV and follows a Maxwellian distribution function. Therefore, the low-energy cutoff of the bandpass filter (~10 keV) could allow 2D FIDA to pick up signal from particles in the wings of the thermal ion distribution function. In order to estimate the contribution of changes in the plasma profiles to the changes in the 2D FIDA signal, we utilize the same forward-modeling technique described above. The simulation predicts the fractional change of $n_n \langle \sigma v_{rel} \rangle$ to be $0 > f > -0.20$ in the core pixels of the 2D profile during a sawtooth crash. This suggests the fractional change of the counter-passing fast-ion density during the crash is –0.38.

Generalizing our previous single-shot analysis, we now turn to a database of shots documenting various different plasma conditions and cross-sectional shapes. All discharges in the database are L-mode plasmas. Bt and Ip range between 1.86–2.05 T and 1.16–1.34 MA, respectively. Average sawtooth periods and amplitudes span 48–108 ms and 0.21–0.37, respectively. Central precrash values of Te and n_e range between ~2.0–5.0 keV and ~2.0–4.0×10^{19} m^{-3}, respectively. Shots in the database include circular, bean-shaped, oval, and "D"-shaped plasmas. Shot data with good FIDA statistics are loaded into a database, and the fractional change f for the vertical and oblique systems is calculated for each condition. The

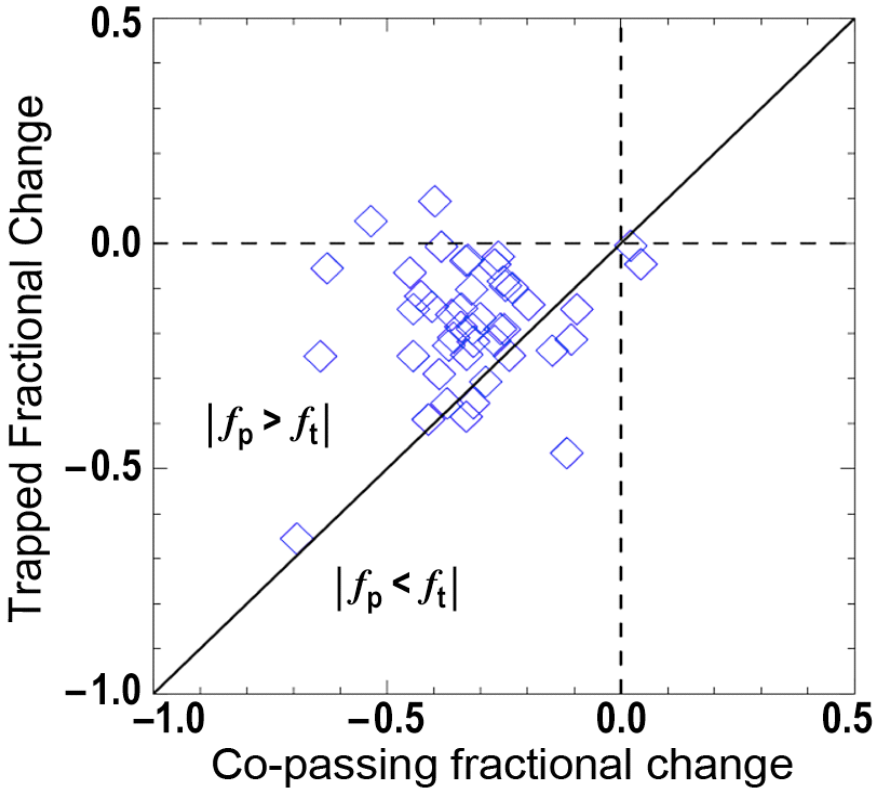

Figure 2.9.

results are presented in figure 2.9 as a scatter plot of $f_{trapped}$ vs $f_{\text{co-passing}}$ for the radial chord closest to the magnetic axis (R=175 cm). The diagonal line plot denotes $f_{trapped} = f_{\text{co-passing}}$. The region of the plot where $|f_{\text{co-passing}}| > |f_{trapped}|$ (bounded by the abscissa and diagonal line) is far more populated than $|f_{\text{co-passing}}| < |f_{trapped}|$; average values of $f_{\text{co-passing}}$ and $f_{trapped}$ are –0.32 and –0.17, respectively. We conclude that, under the conditions studied here, the observation of stronger transport of passing fast ions compared to trapped fast ions generally holds. The interested reader is referred to appendix C for more details on this sawtooth database.

Section 2.3. Modeling and theoretical discussion

Simulations to predict transport levels on DIII-D were carried out for shot 141182 using the theory described in reference [41]. Since fast-ion collision times O(100 ms) calculated in the precrash equilibrium state are much longer than the crash duration O(10μs), collisions are assumed to be a negligible contribution to modifications of the fast-ion distribution function during the crash. Under this assumption, the energetic ion dynamics can be described by their bounce-averaged (or average over poloidal transit in the case of passing particles) drift orbits through a collisionless drift-kinetic equation. The OFSEF (Orbit Following in Sawtooth Electromagnetic Fields) simulation code based on the numerical procedure outlined in reference [41] solves the bounce-averaged Fokker-Planck equation. The code requires information characterizing the precrash state of the plasma. It then evolves the plasma state during a sawtooth crash according to the conventional Kadomtsev model [25]. OFSEF is supplied with precrash data from experimental measurements: the fast-ion density profiles from FIDA, the q-profile and plasma shape from MSE-constrained EFIT reconstructions, and plasma pressure profile from spline-fitted n_e , Ti, and Te measurements. The simulation follows a distribution of fast particles with specified values of total energy E and magnetic moment μ. Due to input constraints in the simulation code, for the case studied here, only 4 different combinations of E and μ for passing particles and 4 different combinations of E and μ for trapped particles were simulated. The goal simply is to demonstrate qualitatively the sawtooth-induced transport dependence on these variables. TRANSP simulations using the full distribution function (including synthetic FIDA diagnostic results) to predict sawtooth-induced transport will be described later. Figure 2.10 shows OFSEF simulation results for the supplied precrash trapped and passing fast-ion profiles. Postcrash profiles are plotted for select values of $\Lambda \equiv \mu B_o / E$

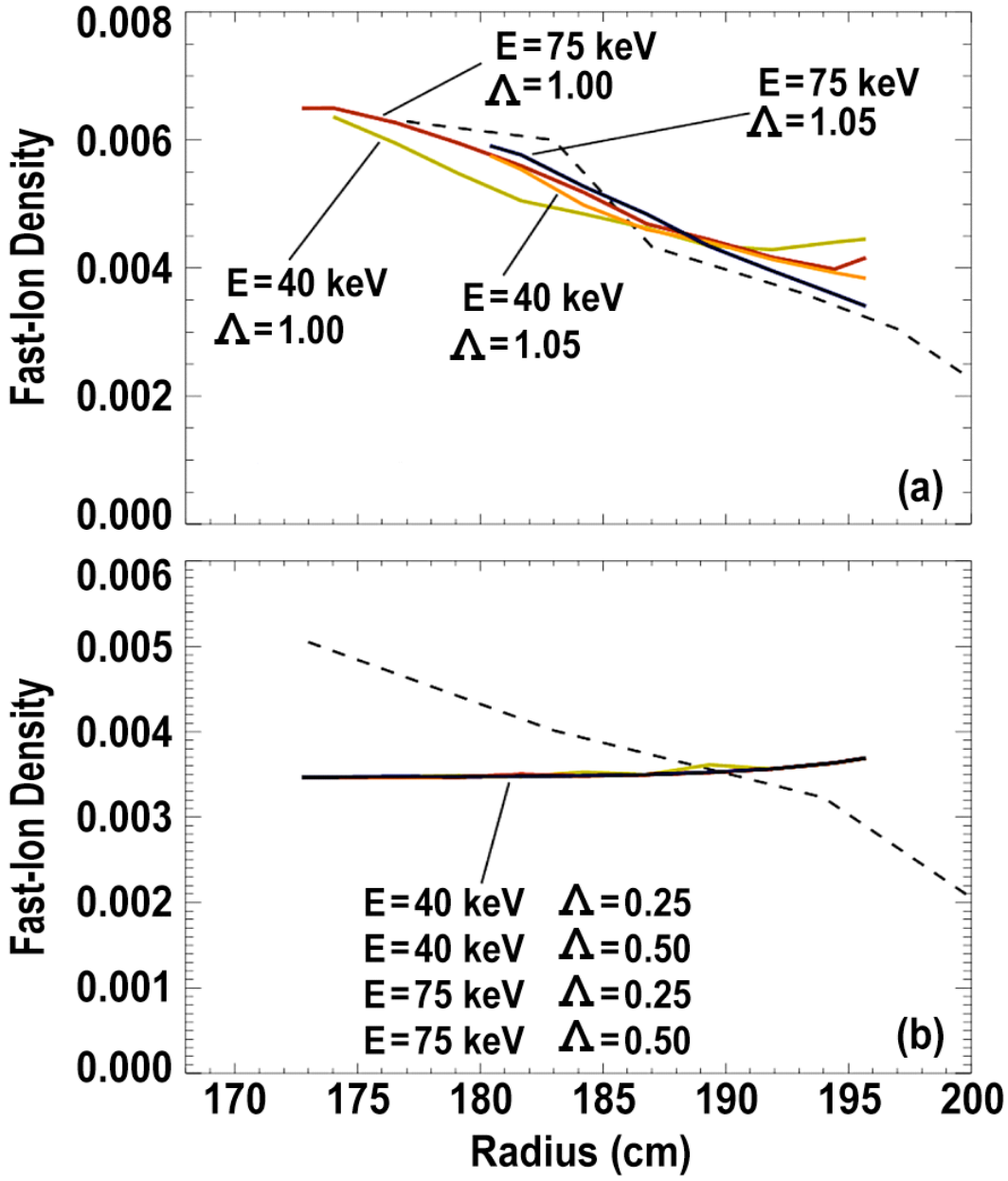

Figure 2.10.

and E (Bo is the magnetic field on axis). The parameter Λ can be thought of as the normalized perpendicular energy, but instead of taking the field at the particle location, the field on axis is used so that is Λ a constant of motion. The simulation reproduces the characteristic that all core passing fast ions experience strong redistribution regardless of E and Λ . However for the trapped particles, their postcrash profile depends sensitively on E and Λ ; small values of E and

Λ produce the flattest postcrash profiles. Evidently, the redistribution boundary of the simulated trapped particles lies in a lower energy range than the simulated passing particles.

Results from figure 2.10 suggest that the severity of sawtooth-induced transport depends on the orbit characteristics of a fast ion. Due to the design of the OFSEF code referred to in the previous paragraph, it is difficult to perform simulations over the entire distribution function. For these purposes, we employ TRANSP which includes an option to turn-on plasma and fast-ion redistribution by sawteeth. The TRANSP simulation is performed for shot 141182 over a period of time that includes 8 relatively uniform sawteeth, each one with a period of approximately 80 ms. TRANSP is provided with EFIT equilibrium reconstructions and spline fits to experimental plasma profiles; the input data is chosen at equally spaced intervals of 15 ms, but TRANSP interpolates the input data between the user-supplied times on a 1 ms time interval. Sawtooth events are explicitly assigned (according to experimental crash times measured by ECE), and TRANSP uses these times to apply the Kadomtsev sawtooth mixing model. One major caveat with the TRANSP sawtooth mixing model is that kinetic effects are not considered. All fast ions are treated thermally and redistributed according to the rearrangement of flux surfaces. The NUBEAM module is called to calculate the beam-ion distribution function 5 ms before and 5 ms after each sawtooth event. As a qualitative check that the TRANSP sawtooth model redistributes fast ions, the average distributions (averaged over fast-ion energies E>20 keV) before and after a crash are compared. Figure 2.11 is the spatial distribution of fast ions predicted by TRANSP before and after a crash event. Precrash and postcrash distribution functions from TRANSP are used as input to the synthetic diagnostic FIDAsim code to predict changes to the FIDA signal during a sawtooth crash. The results are shown in figures 2.12(a) and (b) for the vertical and oblique FIDA systems. It is clear that the simplified sawtooth model in

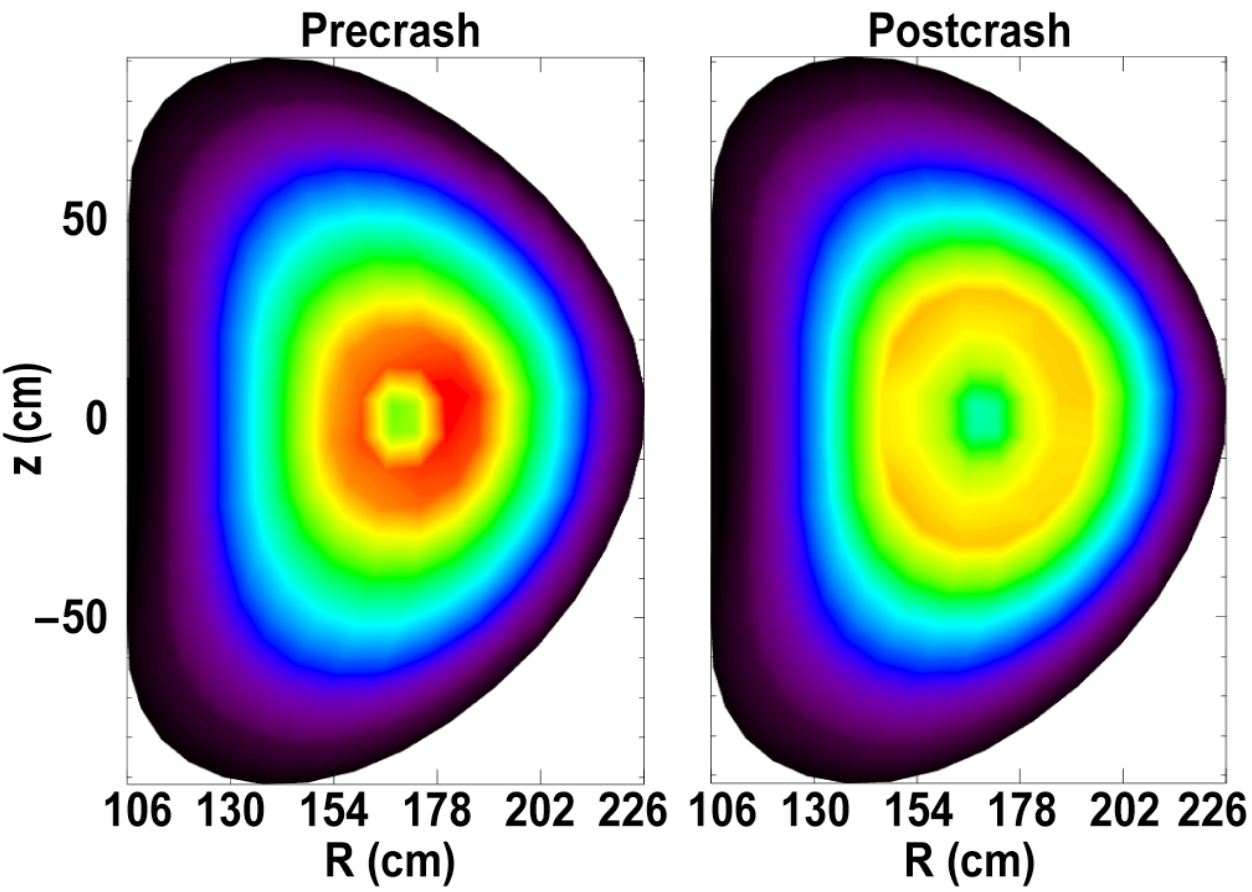

Figure 2.11.

TRANSP underestimates the magnitude of the change in density. The sawtooth crash in TRANSP is modeled after the conventional Kadmotsev theory; surfaces with like-valued helical flux inside and outside q=1 reconnect and form a new unified surface. This process continues until q on-axis is restored greater than or equal to one, flattening the q, density, and temperature profiles inside the mixing radius (largest minor radius at which reconnection occurs). If, in reality, the magnetic surface rearrangement during the crash differs substantially from the Kadomtsev process, there is no reason to believe the effect on particle mixing should be the same. However, although there is a discrepancy in the magnitude of the change in the FIDA signal predicted by the TRANSP Kadomtsev model and the experimental FIDA data, the shapes of the redistribution profiles (the fractional change profiles) agree well. Compare the shapes of

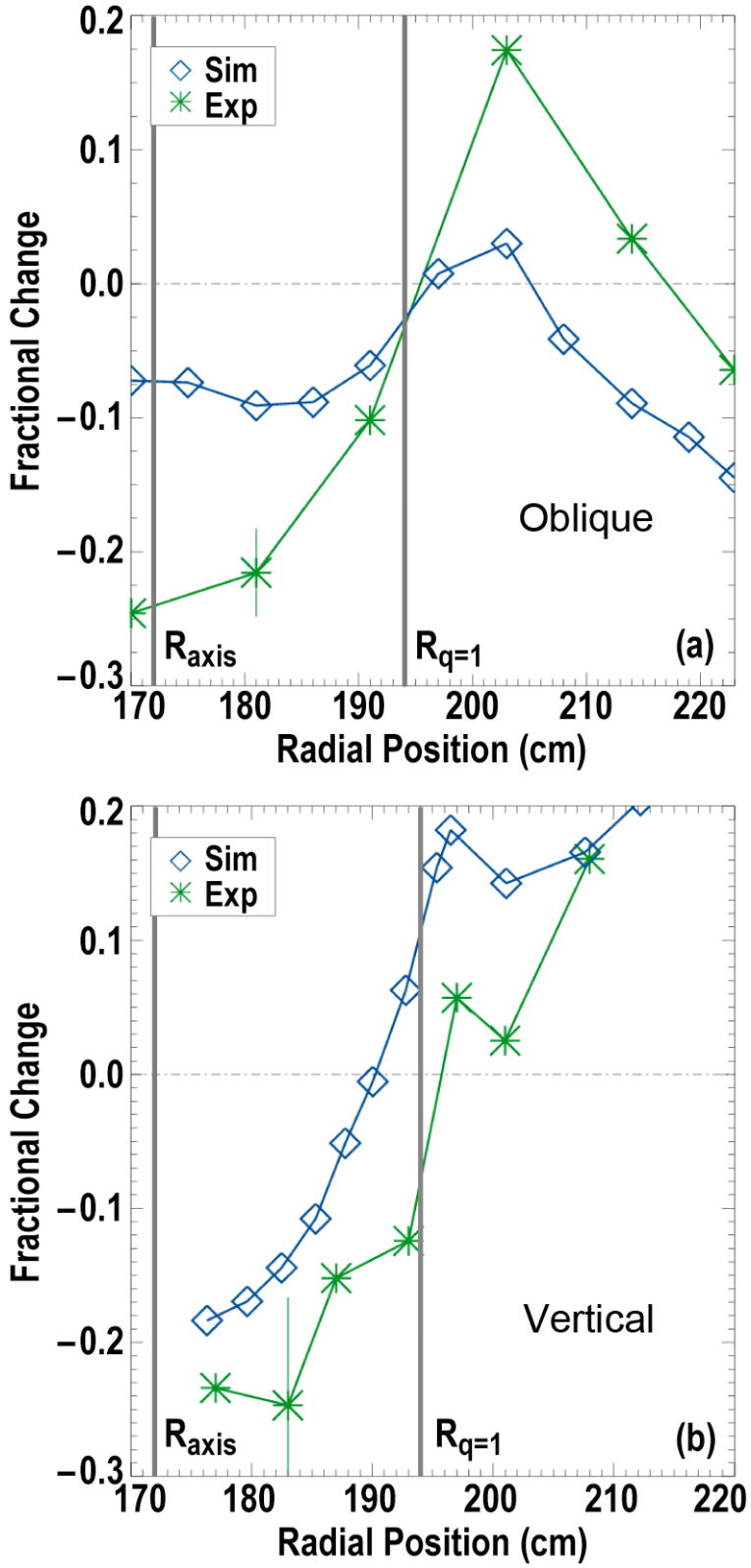
Sim
Exp
Fractional Change
0.2
0.1
0.0
−0.1
−0.2
−0.3
Oblique
R_{axis}
$R_{q=1}$
(a)
170
180
190
200
210
220
Radial Position (cm)
Sim
Exp
Fractional Change
Vertical
R_{axis}
$R_{q=1}$
(b)
Radial Position (cm)

Figure 2.12.

the fractional change profiles between simulation and experiment for the oblique FIDA system in figure 2.12(a). The inversion radius (inner most zero crossing, R=195 cm) and the positive peak in the density change (R=203 cm) are consistent. Also compare the results from the vertical FIDA system in figure 2.12(b). The profiles are monotonically increasing from the axis to R=196 cm where a small dip in the profile occurs, resolved both synthetically and in experiment. The relative consistency between the simulation and experiment suggests that the TRANSP model is accurately redistributing particles spatially, but it does not redistribute the correct number of particles. Therefore, Kadomtsev reconnection appears to be an accurate representation of the observed redistribution. Instead, the discrepancy in the absolute magnitude of changes in the density arises due to kinetic effects of the energetic particles. In the TRANSP simulation, all beam ions inside the mixing radius participate in redistribution during the crash. However from the experimental data and the OFSEF kinetic simulations, we see that this is not realistic; in general, redistribution of trapped particles is less severe than passing particles. Furthermore, fast-ion orbits are not distributed uniformly in space. Typically, the passing/trapped fraction is larger near the axis and decreases with larger major radius. The guiding-center orbit code mentioned earlier is used to map orbit boundaries for full-energy (75 keV) beam ions. Figure 2.13 shows orbit boundaries for full-energy beam ions just before a crash for shot 141182. Indeed, passing particles dominate in the core, and the passing/trapped fraction decreases quickly with increasing R. It becomes clear that a simulation that disregards kinetic effects and that isotropically distributes particle orbits will underestimate the drop in fast-ion density in the core. In reality, the crash will interact mainly with the passing particles, kicking them from the core to larger R. In the meanwhile, according to the Kadomtsev model, particles near the q=1 surface will be kicked inward toward the core. However, the majority of particles near the q=1 surface are those on

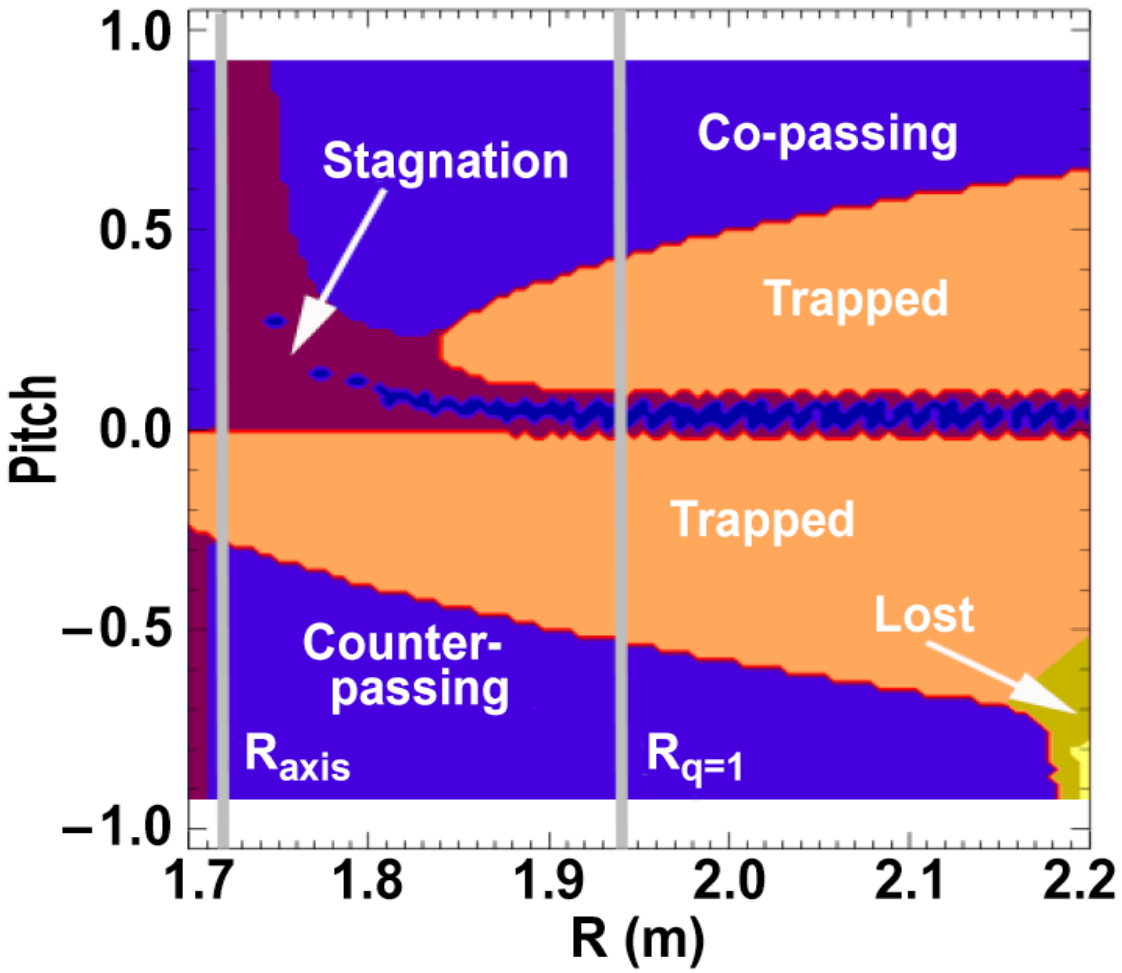

Figure 2.13.

trapped orbits and thus interact weakly with the instability. The net effect is a large drop in the core passing fast-ion density and less so in the trapped fast-ion density, as observed by FIDA. In the following, we discuss the particular aspects of fast-ion kinetic effects that differentiate the behavior of trapped and passing particles.

It is important to understand the dynamics which cause the difference in transport between ions of different orbit classifications. According to the theory in reference [41], the main drive for energetic-ion transport at a sawtooth crash is the **E**×**B** drift associated with the mode-induced electric field. In the ideal MHD framework (except for a thin layer about the reconnection surface), an electric field arises due to the bulk plasma motion during the crash

event. The mode-particle interaction manifests as an **E**×**B** drift past the equilibrium (unperturbed) flux surfaces as the mode evolves. It is this **E**×**B** drift that tends to attach the particle to an evolving flux surface, preserving the magnetic flux linked by the particle. However, aspects of an ion's orbit can modify the effects of the **E**×**B** drift. Firstly, the relative size of a particle's orbit width Δr_b with respect to the sawtooth mixing radius r_{mix} affects the amount of time the particle spends in regions where the mode amplitude is strong; if Δr_b is comparable to or larger than r_{mix} the effect of the **E**×**B** drift on the particle orbit is weakened. Secondly, resonances between the characteristic frequency of the fundamental 1/1 mode and characteristic ion orbit frequencies can cause enhanced transport. The mechanism for the enhanced transport in this case can also be identified as the **E**×**B** drift. Thirdly, finite field curvature and field gradient drifts (collectively leading to toroidal drift) weaken particle attachment to evolving flux surfaces, lessening the effect of the **E**×**B** drift on the particle orbit. Although these three actions occur simultaneously, it is instructive to consider them independently. When $\Delta r_b > r_{mix}$, the particle orbit-averages more time spent in regions where the perturbation is weak compared to $\Delta r_b < r_{mix}$. Thus an ion with $\Delta r_b > r_{mix}$ experiences reduced **E**×**B** drift associated with the mode-induced electric field compared to spending all or most of its time inside the mixing radius. On the other hand, a large orbit-width trapped ion may experience *enhanced* sawtooth-induced redistribution if its energy is sufficiently high to satisfy $s\omega_b + n\omega_{pr} = \omega$ (where s is an integer, ω_b is a trapped (passing) ion's bounce (poloidal transit) frequency, n is the toroidal mode number of the perturbation, and ω_{pr} is the frequency of the bounce/transit-averaged toroidal motion i.e. drift or precession frequency). In the case of sawteeth, a resonance can occur between the helical m/n = 1/1 mode (including its higher n harmonics) and the particle orbit. However, during experiments on DIII-D

in which neutral beam injection is the only auxiliary heating method, the vast majority of fast ions have energies smaller than those required for resonances. Experimental evidence on DIII-D of the resonant interaction between the sawtooth instability and RF-accelerated beam ions will be investigated in chapter 3. When the energy of energetic ions is less than the energy relevant for resonances, the dominant mechanism differentiating passing and trapped particle transport is the toroidal drift due to field curvature and inhomogeneity. Next, we present a brief recapitulation of reference [41], sketching the effect of toroidal drift on particle transport.

In an axisymmetric configuration, assuming conservation of the third adiabatic invariant (φ) and assuming the particle's Larmor radius is much smaller than the characteristic scale length of the field, the particle's orbit traces out a toroidal drift surface, coinciding with a flux surface. The particle's periodic motion along the drift surface can be perturbed due to breaking of the conservation of φ. Of the three adiabatic invariants, φ is the most fragile; it can be broken due to static toroidal asymmetries or temporal changes to the field on a timescale faster than the toroidal drift (precession) time of the particle. The influence of a sawtooth crash on a particle's orbit can be interpreted analytically using a timescale approach. For the purposes here, the guiding-center velocity of a particle can be separated into four terms {see equation (5) in [41]}: (1) particle velocity along the *unperturbed* field ($\boldsymbol{B}_{\boldsymbol{H}}$), $v_{||}^{0}$, (2) toroidal drift velocity, $v_D \sim \rho v/2R$ (where ρ is the Larmor radius, v is the particle velocity, and R is the major radius of the particle location), (3) particle velocity along the helically *perturbed* field ($\boldsymbol{B}^{*}$), $v_{||}^{1}$, and (4) mode-induced **E**×**B** drift velocity, v_E ; the total field is $\boldsymbol{B}=\boldsymbol{B}_{\boldsymbol{H}}+\boldsymbol{B}^{*}$. To determine the influence of a crash on a particle's dynamics, three characteristic times should be considered: the crash duration τ_{cr} (i.e. timescale of changes in the field), the toroidal precession time (bounce/transit-

averaged toroidal period) τ_{pr} associated with v_D, and, for passing particles, the timescale of longitudinal motion (period around a *perturbed* flux surface) τ_Ψ associated with $v_{||}^1$. Analytic formulas for τ_{pr} and τ_Ψ can be found in reference [41]. If the crash is sufficiently faster than a particle's toroidal drift period (i.e. $\tau_{cr} \ll \tau_{pr}$), the drift is too weak, the third adiabatic invariant φ is broken, and the **E**×**B** drift couples the particle to a perturbed flux surface; the particle is transported with the evolving mode across unperturbed flux surfaces. For a passing particle, even if its drift period is shorter than the crash duration, strong transport can occur provided its period about a perturbed flux surface is shorter than the drift period i.e. $\tau_\Psi \ll \tau_{pr}$. When this is the case, $v_{||}^1$ dominates over v_D and the passing particle streams along a constant field line, following the spatially evolving flux surface.

The previous timescale comparison can be mapped in terms of more tractable experimental quantities: total particle energy E and particle pitch χ. A recasting of the passing and trapped redistribution criteria in terms of E and χ will allow us to display redistribution boundaries in an intuitive representation of velocity space. Along with the FIDA weight functions, the redistribution boundaries will give a sense as to how much of the FIDA signal is expected to be affected by a sawtooth crash. Since FIDA collects signal from volumes at the outboard midplane, the following analysis is restricted to poloidal angle θ=0. We calculate the redistribution boundary in velocity-space starting with a precrash axisymmetric equilibrium. The redistribution boundaries ($\tau_{cr} = \tau_{pr}$ and $\tau_\Psi = \tau_{pr}$) can be rewritten in terms of E and χ. In other words, there exists a pitch-dependent energy $E_{crit}(\chi)$ such that particles with total energy E *much less than* this critical value are strongly transported at the crash. The potential for transport depends on τ_{cr}, and the value is determined here by the time it takes the hot Te core to

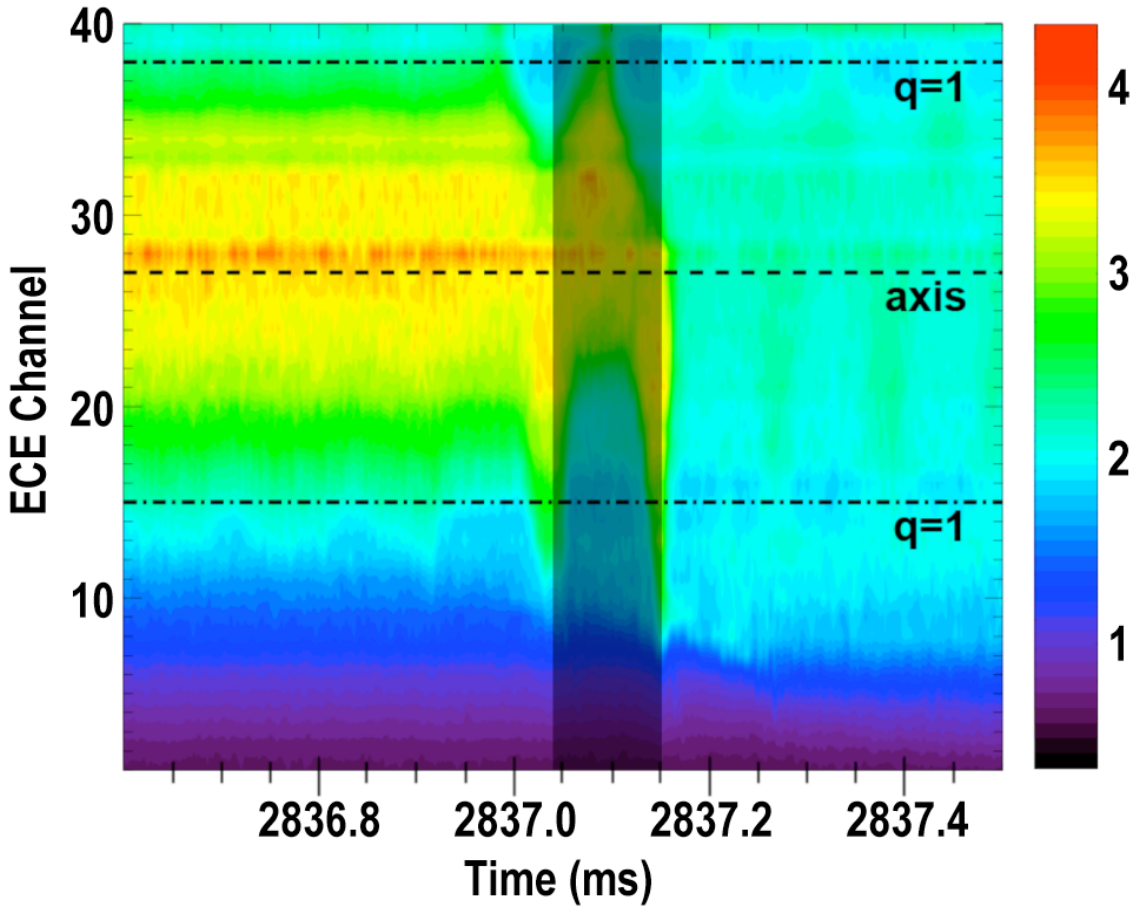

Figure 2.14.

be completely expelled to the periphery, as evidenced by ECE signals. Figure 2.14 is a contour plot of 40 midplane ECE channels during the last 600 μs of a typical sawtooth cycle for shot 141182. The mode becomes unstable around t =2837.00 ms and the helical perturbation, evidenced by the precursor oscillation, grows until the hot core dissipates, and heat is ejected outside the q=1 surface. The shaded region is presumably the crash phase initiating around 2837.05 ms where the helical displacement begins expelling heat outside q=1. The core quickly cools, and after about t=2837.15 ms, the crash has completed, flattening the Te profile inside q=1. Using this definition for the crash phase of several sawtooth crashes, the average τ_{cr} for shot 141182 is about 100 μs.

In order to calculate E_{crit}, τ_{pr} for passing and trapped and τ_{ψ} for passing must be

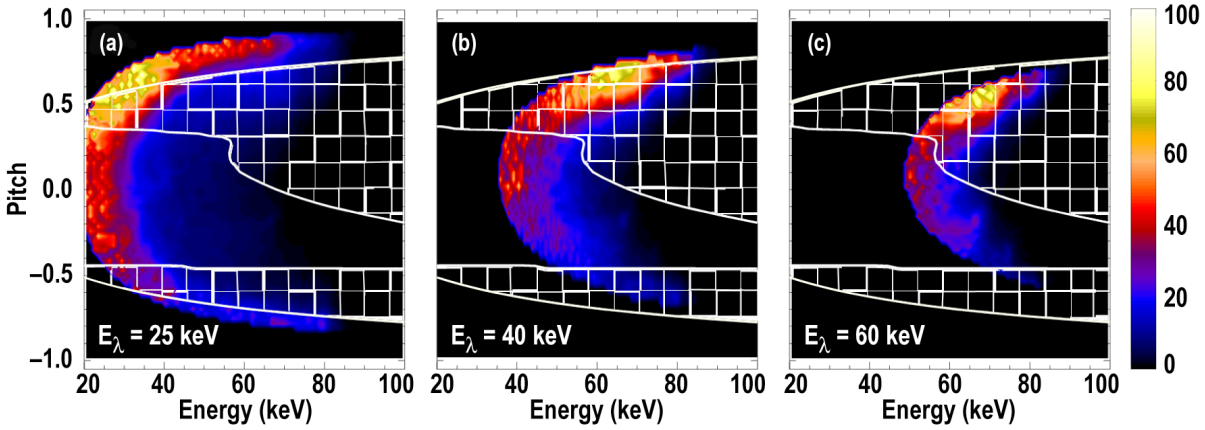

Figure 2.15.

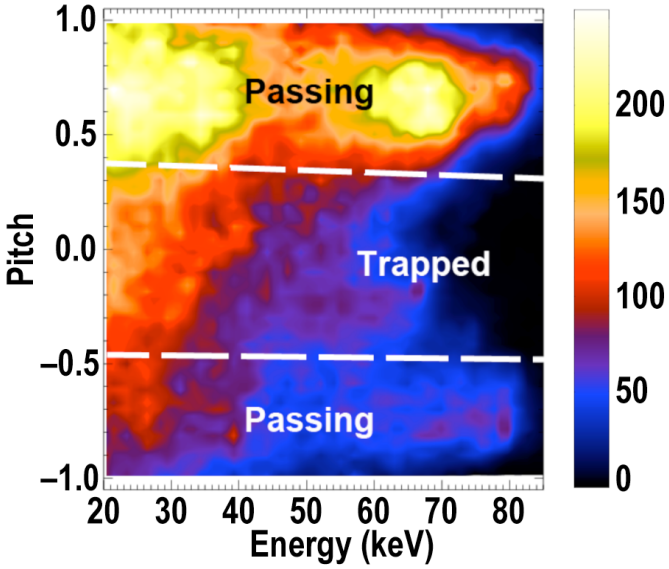

Figure 2.16.

determined. The toroidal precession time τ_{pr} is calculated in an axisymmetric equilibrium by a guiding center code that utilizes the adiabatic invariants of energy, magnetic moment, and canonical toroidal momentum to constrain the particle motion; see appendix in reference [40]. For passing particles an analytic approximation for τ_Ψ is obtained from eq. (10) in reference [41]. The expressions $\tau_{pr} = \tau_{cr}$ and $\tau_{pr} = \tau_\Psi$ (i.e. $E = E_{crit}$) are rewritten in terms of E and χ and plotted in Figure 2.15 along with the weight functions of the vertical FIDA signal for spectral energies E_λ of 25, 40, and 60 keV. These velocity-space plots are generated by taking the

convolution of the weight functions (recall figure 2.4) with a precrash fast-ion distribution function calculated by TRANSP. A contour plot of the distribution function at the midplane and major radius R =182 cm is shown in figure 2.16. These weight functions represent the contribution from velocity space to the measured spectrum at the particular spectral energy indicated. Recall the observation from figure 2.6 that the threshold in spectral energy for redistribution measured by the vertical system is E_λ=40 keV. Therefore, it would be expected that the majority of the weight function corresponding to E_λ=40 keV lies in the no-transport (hatched) region $E > E_{crit}$. Figure 2.15(b) suggests this is the case; only 40% of the signal at E_λ=40 keV is in the transport $E < E_{crit}$ region. Another observation from figure 2.6 is that the spectrum is relatively unchanged by the sawtooth crash for Doppler shifts higher than E_λ=40 keV. Figure 2.15(b) is the weight function for E_λ=60 keV, and only 28% of the signal lies in the transport region $E < E_{crit}$. Conversely, portions of the spectrum with Doppler shifts smaller than E_λ=40 keV are observed to be strongly affected. Figure 2.15(a) is the weight function for E_λ=25 keV, and 65% of the signal is less than E_{crit} , consistent with the significant drop in the spectrum at that Doppler shift. We apply this same interrogation to each of the 3 FIDA diagnostics to demonstrate the measured differences in transport reported earlier in figure 2.8. Figure 2.17 shows the velocity space contribution to the FIDA signal for the three systems on shot 141182. The solid line denotes E_{crit} . Figure 2.17(a) is the phase-space contribution to an E_λ-integrated vertical signal (E_λ = 30–60 keV) for a core-localized viewing chord. Portions of the weight are lower than and greater than E_{crit} ; about 52% of the velocity-space contribution lies below E_{crit} . Figure 2.17(b) is the phase space contribution to an E_λ-integrated oblique

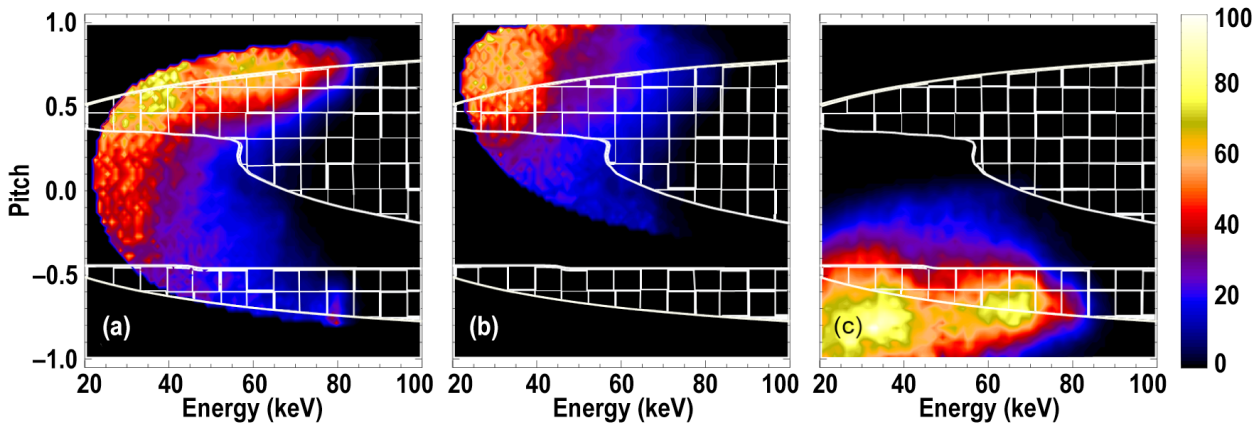

Figure 2.17.

signal (E_λ = 30–60 keV) for a viewing chord near the magnetic axis. About 77% of the weight lies below E_{crit} which is qualitatively consistent with the large core-density drop in the co-passing signal shown in figure 2.8. Similarly for the imaging system (see figure 2.17c), about 73% of the velocity-space contribution lies below E_{crit}, also qualitatively consistent with the large drop observed in the counter-passing FIDA profile. Relatively speaking, the E_{crit} calculations qualitatively reproduce the observed result that the co- and counter-passing particles experience the strongest redistribution. In terms of absolute numbers, the changes to the signals predicted based on the analytic E_{crit} criterion are larger than those observed. Certainly a major contribution to this discrepancy is due to the physical process of the redistribution. The instability does not only cause a removal of some particles from a volume in phase space, but it leads to a mixing action; for example, particles inside (outside) the q=1 surface before the crash are transported outside (inside) q=1 after the crash. The calculations above do not take the mixing into account; the percentages quoted are merely the fraction of the original population which satisfies the transport criteria. This analytic treatment of particle orbits reasonably predicts a critical energy at which toroidal drift becomes crucial for determining the magnitude of particle redistribution.

Section 2.4. Conclusions

The FIDA diagnostics at DIII-D have been utilized to study the phase-space dynamics of fast ions during a sawtooth crash. Spectral analysis indicates that trapped particles up to about 40 keV and all passing particles are redistributed during a sawtooth crash. The difference in transport is attributed to finite toroidal drift effects. While the **E**×**B** drift associated with the helical perturbation is responsible for driving transport (attaching particles to the evolving flux surfaces), an energetic ion decouples from the mode if its toroidal drift is strong enough. This naturally leads to the existence of a critical energy E_{crit} as a function of particle pitch angle. Particles with energy below E_{crit} are strongly redistributed by the sawtooth crash. Calculations of the critical energy are consistent with our observations of the 40 keV energy cutoff observed in the trapped particle energy spectrum.

Presumably, fast ions will behave differently in tokamaks with energetic ion populations above typical neutral-beam injection energies of ~100 keV. In ion-cyclotron-radio-frequency (ICRF) heated discharges on JET, sawteeth are observed to have a strong effect on Helium-3 minority ions with energies above the critical energy [42]. Although toroidal drift is strong for trapped and passing ions at very high temperatures (>>100 keV), effects due to resonances between ions with large orbit width and the underlying mode could become important [43]. Therefore, in tokamaks where the superthermal ion population is dominated by ~O(1 MeV) particles, sawteeth may coherently interact with the high energy resonant particles. A proxy of this regime is investigated in chapter 3 where a spatially-localized population of ICRF-accelerated beam ions in DIII-D is suppressed following a sawtooth crash. In addition, during the ICRF-heating phase, fast-ion losses concurrent with a sawtooth crash are observed. Although sawtooth-induced loss signals observed on DIII-D are small, the mere observation suggests this

issue could be of concern for ITER. The radius of the q=1 surface in baseline discharges of ITER will be a significant fraction of the plasma (r/a ~ 0.5) leading to potentially very large sawteeth which may interact with the alpha population. If large numbers of alphas are redistributed into loss cones, energy fluxes to the wall could be problematic. As the ions thermalize (<100 keV), fewer particles satisfy the resonance conditions.

A decrease in energy narrows their orbit width and decreases their toroidal drift. In this regime, passing particles are dominantly transported, as studied in this chapter. The transport of beam ions (E<100keV) at a sawtooth crash on DIII-D is relatively benign; although their internal redistribution manifests as a 20% reduction in the fusion rate, no losses are observed. However, the potential for loss is strongly dependent on the equilibrium (which dictates the loss boundaries in phase space) and the relative size of the sawtooth mixing radius to minor radius of the tokamak. Therefore, the possibility of energetic-ion losses at a sawtooth crash on ITER should not be completely ruled out. This is a relatively unexplored aspect of ITER that deserves some attention.

Thermalization of the fast ions to energies <<100 keV makes the ions indistinguishable from the thermal population; ions with typical thermal energies (~10keV) have negligible orbit width and weak toroidal drift. Passing and trapped thermal particles alike are well situated near flux surfaces and both experience redistribution at a sawtooth crash according to the rearrangement of the flux surfaces.

CHAPTER 3. Measurements of fast-ion transport by mode-particle resonances on DIII-D

Section 3.1. Introduction to mode-particle resonances

Some of the most important interactions with energetic particles arise from macroscopic ($\rho \nabla \boldsymbol{B} / B \ll 1$ where ρ is the Larmor radius) magnetohydrodynamic (MHD) instabilities, many of which possess wave-like properties. Due to the periodic structure of the electromagnetic fields associated with such instabilities and the periodic motions associated with confined charged particles, coherent interactions over many orbital periods can occur; resonances between the particle's periodic orbital motions and the wave-like behavior of the mode can cause significant modifications to the orbit. A rigorous treatment of single particle interactions with the auxiliary electromagnetic field is tractable through the Hamiltonian formalism. A comprehensive introduction and useful examples pertaining to toroidal devices can be found in ref. [44]. In the Hamiltonian approach, mode-particle resonances occur when the phase between the mode and periodic particle motions is conserved. Resonant particles become trapped within the mode, and their motion is damped or accelerated by the auxiliary electromagnetic forces. In phase space, this interaction manifests as orbital islands; particles are displaced from their original positions in the unperturbed equilibrium state.

According to the Hamiltonian formalism, in toroidal geometry with ζ and θ as the toroidal and poloidal angular coordinates of the particle and n and m as the toroidal and poloidal mode numbers, exact resonance occurs when the phase change is zero,

$$n \ d\zeta/dt - m \ d\theta/dt - \omega = 0 \qquad (3.1)$$

For well-passing particles with small orbit width, it is possible to satisfy eq. (3.1) along their entire orbit; however, eq. (3.1) is not satisfied at all times for particles with finite orbit width; the drift contributions to the first two terms on the left side of eq. (3.1) become important. Instead, the resonance condition can be satisfied for finite-orbit width particles if the phase change is zero after one bounce period. In other words, particles can resonate with a Fourier decomposable mode if they satisfy the bounce-averaged version of eq. (3.1), the so-called bounce-precessional resonance,

$$n\omega_{pr} - s\,\omega_b - \omega = 0 \qquad (3.2)$$

where ω_{pr} is the toroidal drift (precession) frequency, ω_b is the bounce frequency, and s is an integer. Theoretically, any coherent MHD instability with real-value frequency and characterized by toroidal and poloidal mode numbers can resonantly affect a fast-ion population, where the intensity of the interaction depends linearly on the mode amplitude.

Alignment in phase space of the mode structure and peaked regions of the energetic-ion distribution function can lead to substantial flattening of the distribution function, reducing the fusion reactivity. In some cases, the velocity-space redistribution of resonant particles is enough to move them across loss boundaries, expelling them from the plasma. A classic example comes from the PDX tokamak. Measurements of large beam-ion losses concurrent with bursts of MHD activity dubbed “fishbones” [45] spurred theoretical investigations as to the cause of the large losses. The traditional fishbone instability appears in high-beta plasmas with a q=1 surface where

a sufficiently large trapped particle population destabilizes the m/n = 1/1 internal kink mode [46]. The observed ejection of beam ions during the fishbone activity occurs at a fixed phase relative to the mode, so beam ions are lost in a beacon-like fashion; this is explained by the "particle pumping" theory, where the mode frequency matches the toroidal precession frequency of trapped beam ions [47] {the n=1, s=0 solution to eq. (3.2)}. Since the PDX observations, innumerable accounts of resonance-induced fast-particle transport by a variety of instabilities have been reported. In the following sections, experimental work regarding mode-particle resonances on DIII-D is presented. Section 3.2 extends the material in chapter 2 regarding fast-ion transport by the sawtooth instability. In this section, experimental data suggests that ICRF-heated beam ions are accelerated above the critical energy (redistribution boundary) described in chapter 2. Despite their sufficiently high energies making them impervious to redistribution by flux attachment, the ICRF-accelerated ion population is diminished after a sawtooth crash. The possibility of transport by mode-particle resonances is elucidated. In section 3.3, a cursory description of mode-particle interactions by other instabilities on DIII-D (off-axis fishbones and Alfvén eigenmodes) will be presented. Finally, summarizing comments can be found in Section 3.4.

Section 3.2. Mode-particle resonances by the sawtooth instability

Low-n modes such as the 1/1 internal kink associated with the sawtooth instability typically have large radially-extended mode structures ($\delta r/a \sim 0.3$) and large mode amplitudes ($\delta B/B \sim 10^{-3}$ measured outside the plasma). Although not conventionally thought to interact resonantly with energetic particles, the sawtooth instability has been observed to redistribute ion-cyclotron resonance frequency (ICRF) heated helium-3 minority ions [42] with energies greater

than the critical value for flux attachment. The conventional theory of transport by flux attachment [41] (summarized in chapter 2) cannot explain the observed redistribution of the highly-energetic helium ions. One theory details a possible alternative explanation, attributing the transport to resonant matching of the mode frequency to the characteristic orbital bounce and precession frequencies [48] [49]. As with any mode-particle resonance, energy is exchanged between the particle and mode where energy gain/loss is associated with radial excursions inward/outward. While the instantaneous energy exchange can be nonzero, the orbit-averaged change in energy of the resonant fast ions at the sawtooth crash is approximately zero when the mode frequency is much less than the bounce and precession frequencies [49]; in this case, the perturbation potential is approximately steady state and the particle's Hamiltonian is independent of time. The resonant interaction instead modifies the canonical toroidal momentum and thus the pitch distribution of resonant particles.

Experiments on DIII-D show evidence of mode-particle resonances at a sawtooth crash. The plasma shot of interest is #141196, an L-mode discharge with both NBI and ICRF heating at the tail-end of the discharge. Before the ICRF is turned on, during NBI only, the line-averaged electron density is $2.3\times10^{19}m^{-3}$ and central electron temperature is 2.8keV. When 2.5MW of high-harmonic ICRF is included (1.1MW at 60MHz and 1.4MW at 90MHz corresponding to the 4^{th} and 6^{th} harmonics of the deuterium ion gyro-frequency), the line-averaged density increases to $3.3\times10^{19}m^{-3}$, central electron temperature rises to 5.3keV, and the neutron rate increases by a factor of 2. The rise in the neutron rate suggests that beam ions are accelerated by the fast wave through the high-harmonic ICRF heating. In addition, a small radially-localized group of beam ions couple to the FW, evidenced by the appearance of an off-axis peak in the fast-ion density profile measured by FIDA; see figure 3.1. The off-axis peak on the midplane is centered at

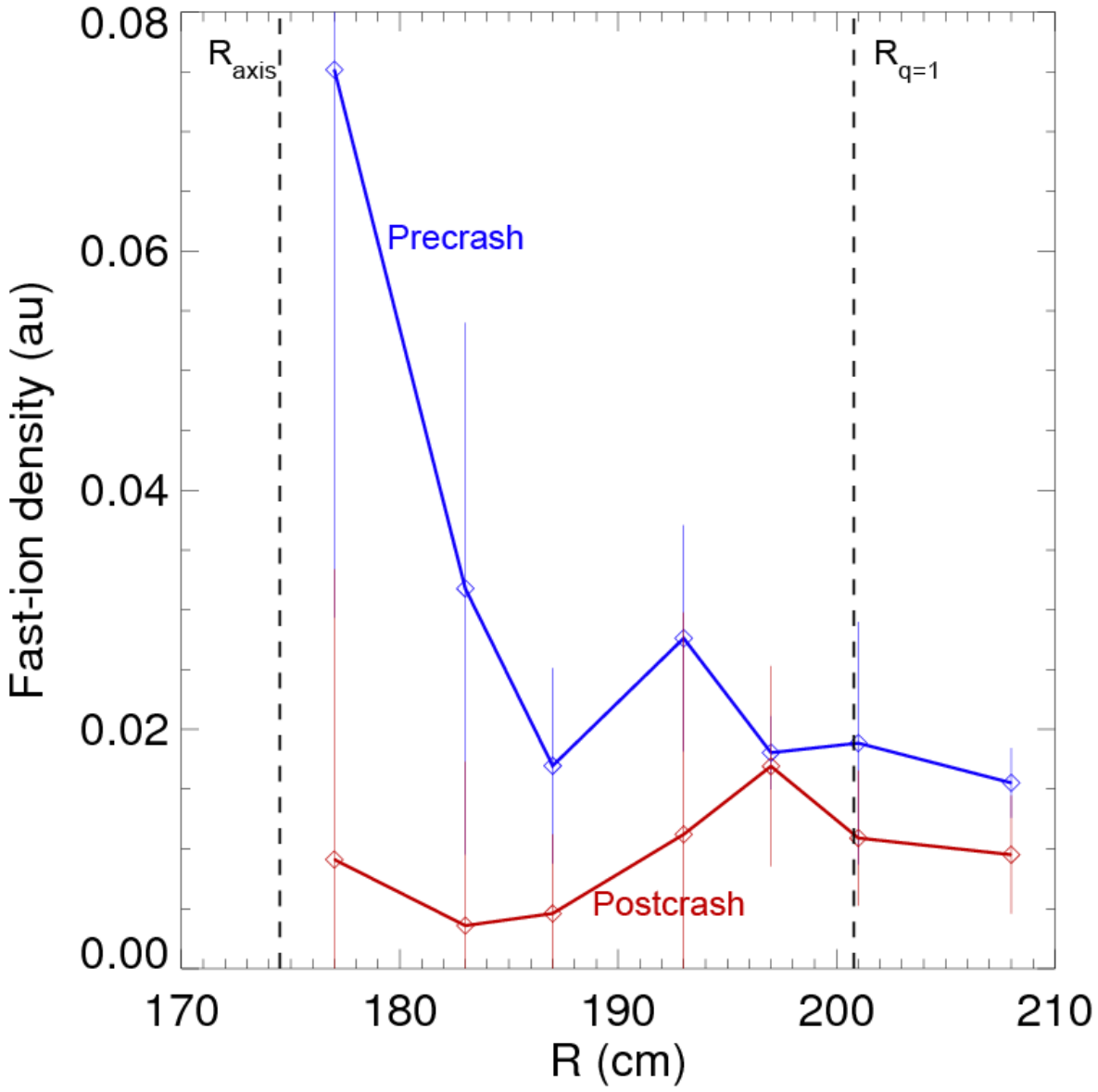

Figure 3.1.

R=193cm, in a region of the plasma where q<1. Similar observations have been reported in earlier DIII-D experiments during 4th and 5th harmonic ICRF heating [9]; the off-axis peak is attributed to the finite-width orbits of trapped ions that couple to the resonance layer (nearly coinciding with the major radius of the magnetic axis) at their banana tips. At a sawtooth crash, the central and off-axis peaks in the fast-ion density profile are flattened. Furthermore, enhanced signals from a Faraday cup fast-ion loss detector [50] concurrent with a sawtooth crash only

appear when the ICRF heating is on; the signal is absent during the NBI-only phase. See figure 3.2. Figure 3.2a is a time slice of the electron temperature signal measured by the core-most channel of the electron-cyclotron emission (ECE) diagnostic. The sawtooth characteristic is readily seen; the large drops correspond to the sawtooth crashes while the intermediate lower-amplitude drops between crashes correspond to relaxation events [51]. Also plotted in figure 3.2a, the power coupled to the plasma injected by the fast-wave antennae is shown. The plasma is heated by NBI alone until t=4350ms when the 60MHz fast-wave system is initiated. Then at t=4700ms, the 90MHz fast-wave antenna is energized and further heating is achieved, evidenced by the increasing amplitude of the Te signal. The fast-ion loss signal in figure 3.2b arises from ions with energy greater than 10keV striking the detector on the outer wall at the midplane. Enhancements in the loss signal occur at a sawtooth crash only when the ICRF is on, and the enhancements are more pronounced during the 60+90MHz ICRF phase compared to the 60MHz-only phase. These observations suggest the radially-localized RF-accelerated beam ions strongly couple to the MHD mode at the sawtooth crash, despite their high energy. Assessment of the transport requires knowledge of 1) the regions of velocity space affected by the sawtooth instability and 2) the velocity-space distribution of fast ions just before a crash.

To determine the regions of velocity space affected by the sawtooth crash, the resonance conditions {eqs. (3.1) & (3.2)} are evaluated. Because diagnostic constraints on bandwidth make it impossible to resolve the mode frequency during the crash, ω is determined by the residual magnetic fluctuations that occur before (precursors) or after (postcursors) the crash. Signal from a single external magnetic probe is plotted in figure 3.2c. The crash events are accompanied by large magnetic bursts ($\delta B/B \sim 10^{-3}$ measured at the edge) as well as lower amplitude fluctuations ($\delta B/B \sim 10^{-4}$ at the edge) corresponding to magnetic postcursors. The magnetic signals are

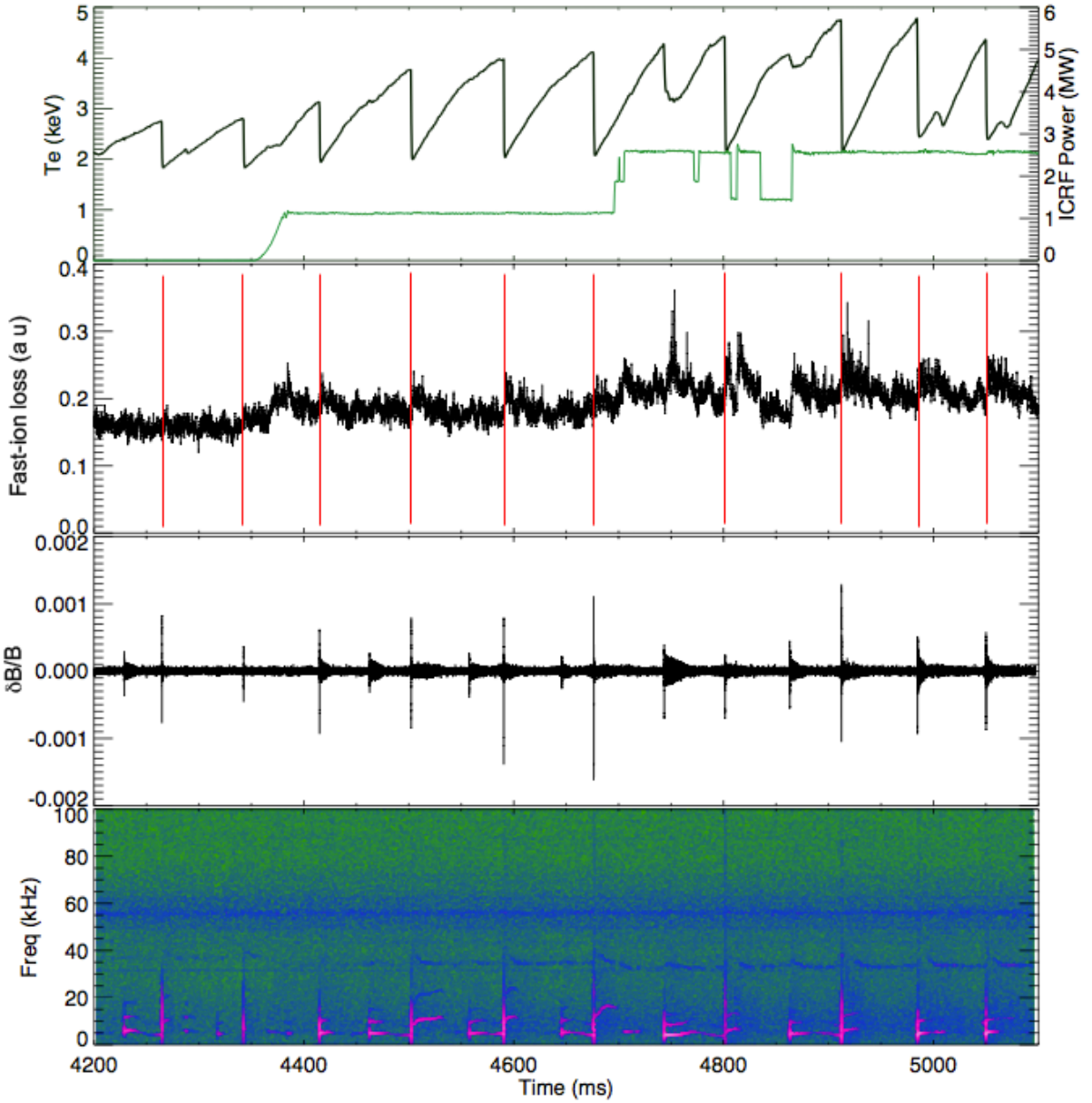

Figure 3.2.

Fourier analyzed, and a spectrogram of the crosspower between two toroidally separated external magnetic probes is shown in figure 3.2d. While the crash events themselves possess a broadband spectral feature, the postcursors have a well-defined frequency spectrum, and the mode frequency can be inferred from the postcursor oscillations. The frequency of the fundamental n=1 harmonic is ~6kHz which matches the plasma toroidal rotation determined by CER

measurements. Higher harmonics (n=2 and sometimes n=3) are also present. The *observed* mode frequency ω' can be represented as the superposition of the toroidal rotation ω_{rot} and the natural mode frequency ω, i.e.,

$$\omega' = \omega + \omega_{rot} \qquad (3.3)$$

Since experimentally $\omega' \approx \omega_{rot}$, this implies that $\omega \approx 0$ and eq. (3.2) can be simplified to,

$$n\,\omega_{pr} - s\,\omega_b = 0 \qquad (3.4)$$

The bounce and precession frequencies are calculated numerically by a guiding-center code in a precrash axisymmetric equilibrium determined by EFIT [35]. The relevant resonance curves (solid curves) along with the critical energy boundary (dashed curve) and a preliminary estimate of the fast-ion distribution function (color contour) are plotted in figure 3.3 as a function of fast-ion energy and pitch. The spatial location of the velocity-space map corresponds to the radial position at the midplane where the largest drop in fast-ion density is observed (R=193cm). The distribution function during the NBI+ICRF heating phase of #141196 is modeled with the quasilinear Fokker-Planck code CQL3D [52] coupled to the ray tracing code GENRAY [53]. The effect of the ICRF heating on the beam-ion distribution is readily seen. The full-energy components of the the co- and counter-current injecting neutral beams correspond to the peaks in the distribution function at E=75keV and pitch values of about +/-0.6 for the co/counter-sources. The CQL3D simulation shows clear acceleration by ICRF heating of beam ions above the neutral beam injection energy. The resonance curves in figure 3.3 are surrounded by a shaded region indicating the resonance width. The width represents the extent to which particles that resonate

with the mode can spread out in velocity space. The width is estimated for particles with $\Delta r_b \ll r$ by the prescription described in ref. [48]; for particles with $\Delta r_b \sim r$ this calculation of the resonance width is an underestimate. The particle's Hamiltonian is first constructed considering a first order electrostatic perturbation.

$$H = H_o + e\Phi_1(P_T)\cos[X - X_o(P_T)] \tag{3.5}$$

where P_T and Ω play the role of the momentum and spatial canonical variables. Taylor-expansion around the resonance and retaining terms up to 2nd order yields,

$$H = H_o(P_{Tr}) + 1/2\ \partial \dot{X}/\partial P_{Tr}\ (P_T - P_{Tr})^2 + e\Phi_1(P_{Tr})\cos[X - X_o(P_{Tr})] \tag{3.6}$$

where the subscript r denotes evaluation at the resonance. Manipulating eq. (3.6), one finds that the change in the canonical momentum variable,

$$\Delta P_T = 4\,|e\Phi_1\ /\ \partial \dot{X}/\partial P_T|_r^{1/2} \tag{3.7}$$

An estimate for Φ_1 is obtained by assuming its existence through the **E**×**B** flow of the bulk plasma motion during the crash; $-\nabla\Phi = \boldsymbol{E} \rightarrow |\Phi| \sim E\, r_{mix} \sim v_{\mathbf{E}\times\mathbf{B}} B\, r_{mix} \sim B\, r_{mix}^2/\tau_{cr}$. Eq. (3.7) is mapped to (R, z, E, $v_{||}$/v) and plotted in figure 3.3. Theoretically, since the orbit-averaged change in energy of the resonant particles is approximately zero, the interaction modifies the canonical toroidal momentum and thus the pitch angle distribution of the resonant particles.

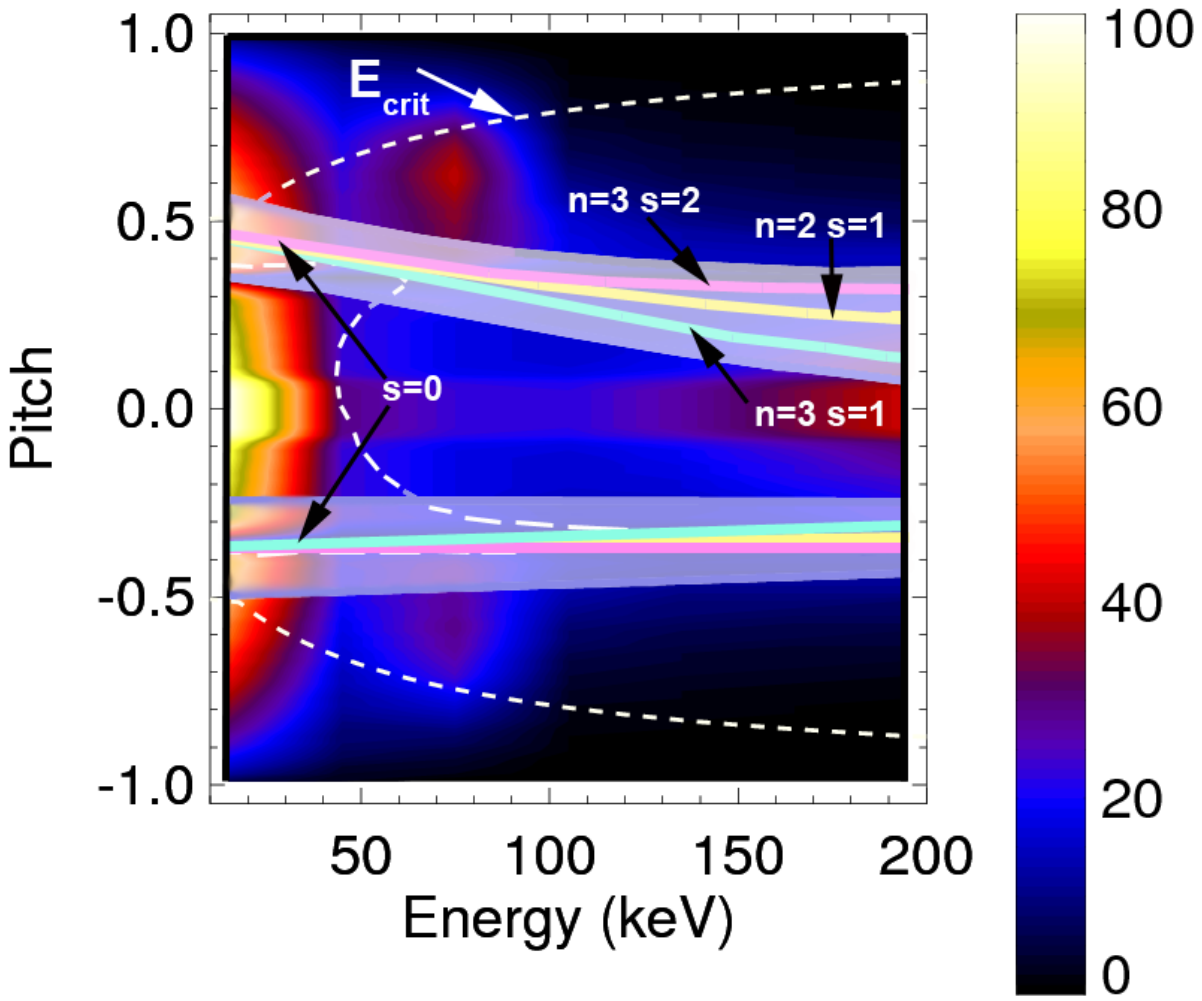

Figure 3.3.

At the spatial location of the off-axis peak in the fast-ion density, a sawtooth crash causes changes in the FIDA spectrum up to the highest resolvable Doppler shifts (~80keV). The fast-ion profiles in figure 3.1 are generated by integrating over a wavelength band of the FIDA spectrum corresponding to fast ions with energy >50keV. In figure 3.1, the fast ions contributing to the profile at the ICRF-induced peak (R~193cm) are mainly from the portion of velocity space to the right of the E_{crit} curve ($E > E_{crit}$) and $|\chi| < 0.5$. The fast ions in this region of velocity correspond mainly to those accelerated by ICRF, according to CQL3D. It is then likely that these fast ions exceeding E_{crit} and overlapping the resonant regions of velocity space are

contributing to the observed loss and redistribution signals.

Unfortunately, the shot shown in figure 3.2 is unique; over the course of the experiment, the plasma shape was swapped between oval and bean-like, and the ICRF power was increased over the course of the experiment. The shot analyzed here was the final one of the experiment, having a bean-shaped plasma with the largest injected ICRF power. Since signal-to-noise levels with FIDA are low and the Faraday-cup loss signals integrate all incident ions with energy >10keV, there is significant uncertainty regarding the particular fast-ion orbits participating in the mode-particle interaction. The data are consistent with the hypothesis that RF-accelerated ions are displaced through resonances with the mode, but we cannot totally exclude transport by flux-attachment or other possible mechanisms (such as stochastic orbital motion due to ergodic magnetic fields). The results are inconclusive but intriguing, and various diagnostic improvements since the 2010 experiment make this a valuable research topic to revisit.

Section 3.3. Mode-particle resonances by other instabilities

Although the bulk of this thesis involves the investigation of the interaction between the sawtooth instability and energetic ions, research efforts also went into various other studies of transport phenomena*. The two that pertain to the theme of this chapter are transport by off-axis fishbones and Alfvén eigenmodes.

Off-axis fishbones

Bursts, similar to traditional q=1 fishbones, are observed on DIII-D in high-beta plasmas with q>1 and heated by neutral beam injection [54] [55]. Dubbed "off-axis fisbones," they have a

* The work on sawteeth, off-axis fishbones, and Alfvén eigenmodes was presented on behalf of the DIII-D group at the 12th IAEA Technical Meeting on Energetic Particles in Magnetic Confinement Systems. My contributions to the fishbone and AE work were secondary, while the main focus of this thesis pertains to transport during the sawtooth instability.

fishbone-like magnetic signal and eigenfunction situated on the q=2 surface. The bursts, each lasting about 2ms and occurring periodically approximately every 20ms, possess a downward-chirping frequency spectrum. The characteristic magnetic signal of 3 off-axis fishbone bursts is presented in figure 3.4a for shot 141086 on DIII-D. The signal is obtained from a magnetic probe located in the plasma-facing wall at the outer midplane. The spectral crosspower between two magnetic probes separated toroidally at the midplane is shown in figure 3.4b. The spectral features of the burst near t=1640ms are well resolved and show multiple harmonics. The fundamental n=1 component has a frequency of about 6kHz. For fishbones characterized by n=1 and relatively low frequency {$\omega \sim O(10kHz)$}, since the bounce frequency ω_b of the bulk of energetic ions is much larger than ω , the n=1, s=0 solution to eq. (3.2) dominates,

$$\omega_{pr} - \omega = 0 \qquad (3.8)$$

Resonance with passing particles {eq. (3.1)} is also possible and occurs for mode frequencies well below the transit frequency. In general, however, resonances with passing particles are less important since the spatial range over which the resonance condition is satisfied is small [47]. The small magnetic perturbations produced during fishbone bursts by the n=1 mode lead to periodic and secular modifications to particle orbits. For a resonant particle, the secular motion dominates and, over the course of each bounce period, the particle gets kicked in the radial direction. Figure 3.5 depicts the resonance condition eq. (3.8) in velocity space near the q=2 surface during the fishbone burst around t=1640ms. Trapped particles near the neutral-beam injection energy (80keV) have the greatest potential for loss. Particles with orbits satisfying eq. (3.8) can lose energy and canonical toroidal momentum during the resonant

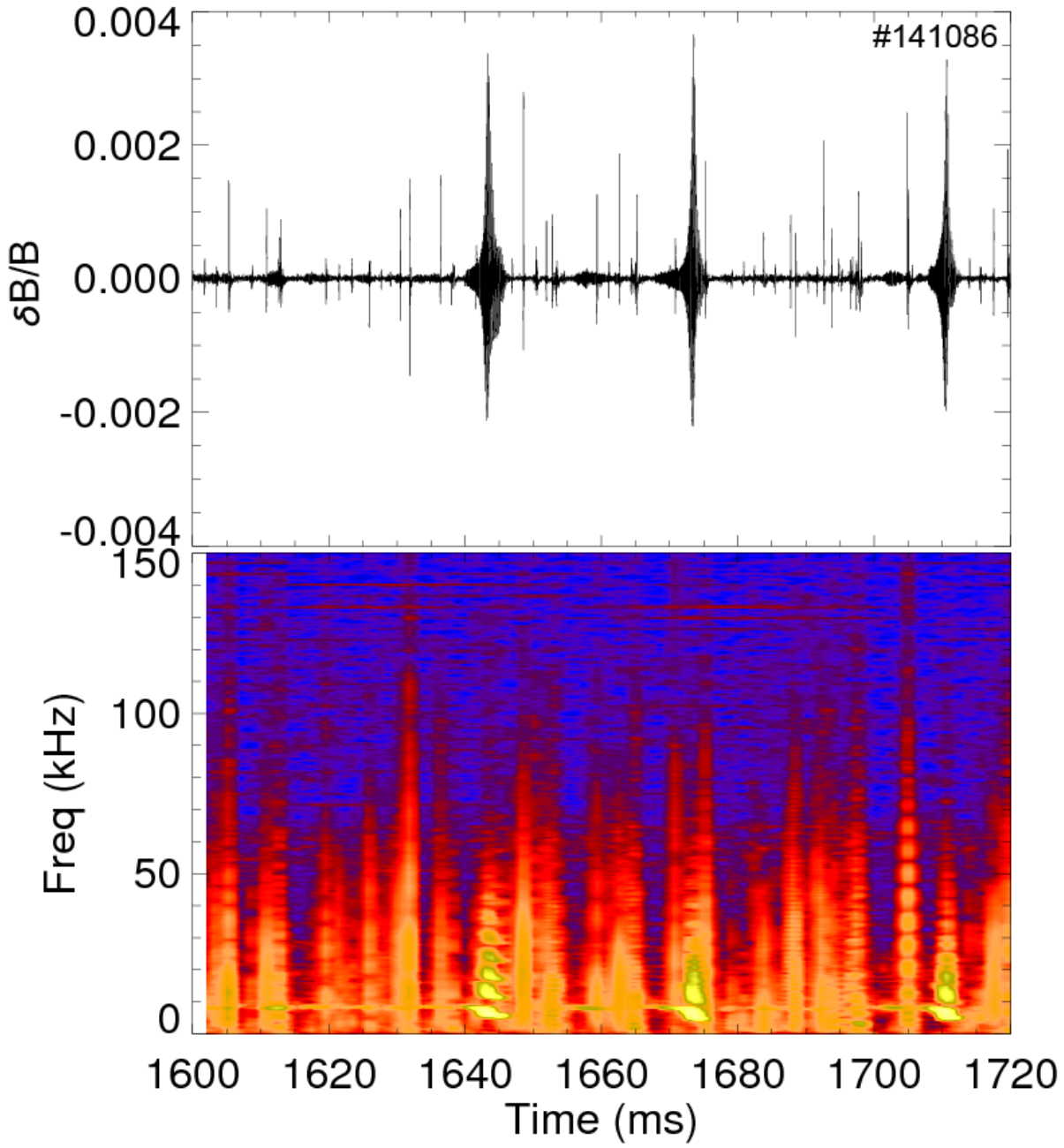

Figure 3.4.

interaction, leading to an orbit transformation into the lost region of velocity space.

Off-axis fishbone-induced losses of beam ions are observed in 7 independent detectors, including a novel implementation of DIII-D's FIDA and beam-emission spectroscopy (BES) systems [56]. The primary goal of the FIDA diagnostic is to measure the Doppler shift of photons emitted from

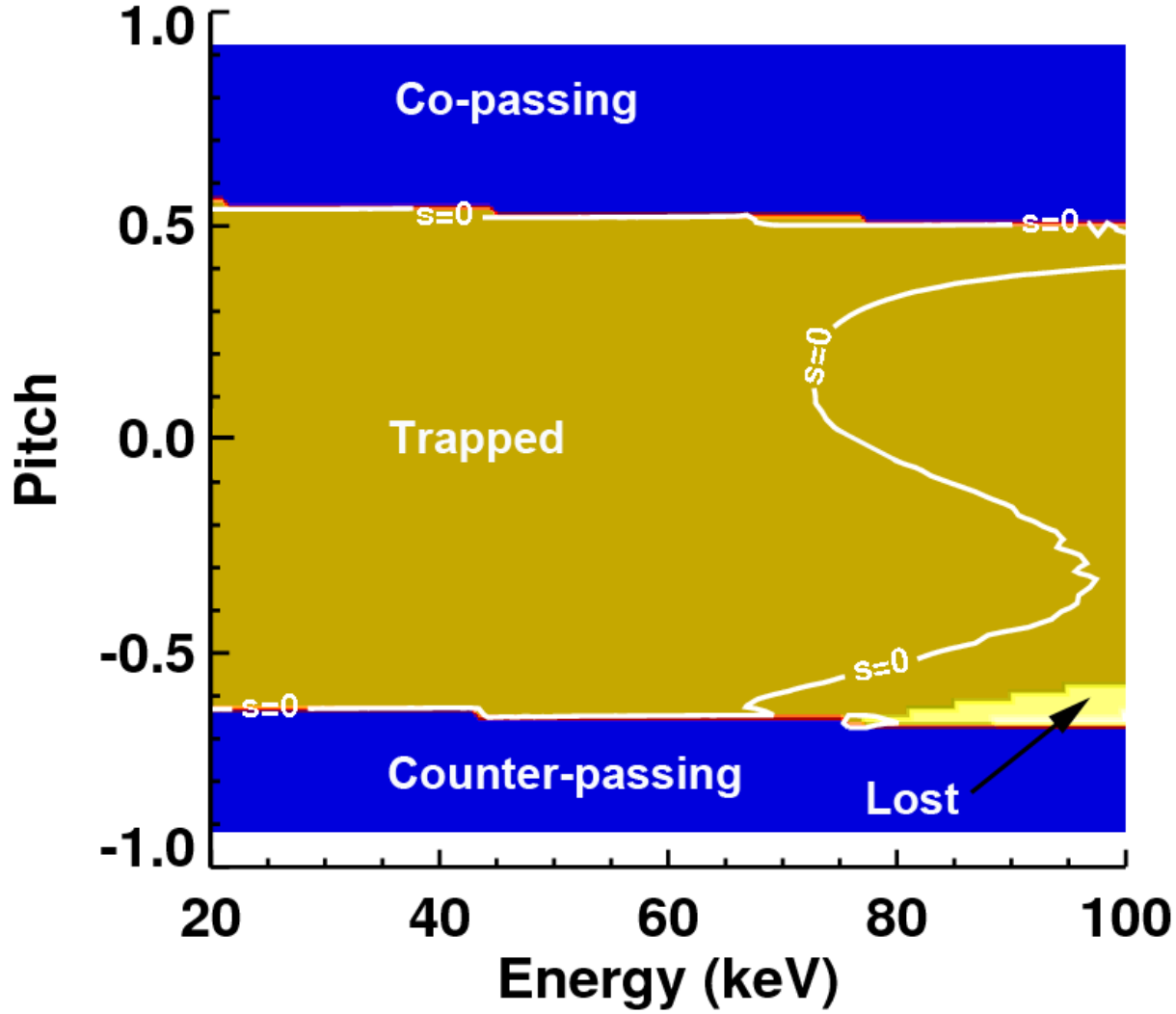

Figure 3.5.

atomically excited neutralized fast ions that undergo charge-exchange with injected beam neutrals. However, when used passively (the diagnostic neutral beam turned off), the FIDA diagnostic can detect lost fast ions that undergo charge-exchange with edge neutrals, assuming the efflux of fast ions and edge neutral density are large enough to produce sufficient light. The BES diagnostic measures density fluctuations through detection of the emitted light from injected neutrals excited by collisions with the bulk plasma [57]. The DIII-D BES system utilizes the Doppler-shifted components of the the Dα spectrum to measured the density fluctuations [58]. Therefore, in passive mode it too can pick-up FIDA light emitted from the edge. Data from

the 7 loss detectors provide corroborating evidence that losses are emitted in a beacon-like fashion with a fixed phase relative to the mode, just like the losses observed on PDX. Analysis of a database of 513 bursts with n=1 structure in q>1 plasmas was compiled. The beam-ion loss rate at each burst is assessed by the time derivative of the neutron rate. The mode amplitude at each burst is determined from dB/dt measured by an external magnetic probe. Similar to the losses on PDX during q=1 fishbone bursts, the beam-ion loss rate and the mode amplitude correlate well (correlation coefficient r = 0.81) during off-axis fishbone bursts. Theoretically, linear dependence of the loss rate on the mode amplitude indicates convective transport mechanism. Diffusive transport cannot be ruled-out, however, since the beam-ion loss rate also correlates well with the square of the mode amplitude. However, the coherence of the losses with the mode and the comparable nature of fast-ion losses observed in both types of fishbones on PDX and DIII-D suggests that the same resonance-induced convective loss mechanism applies. The interested reader is referred to ref. [56] for detailed characterization of off-axis fishbones and their interaction with energetic beam ions.

Alfvén eigenmodes

In DIII-D experiments with neutral-beam injection during the current ramp phase of the discharge, various types of Alfvén eigenmode (AE) activity are observed. In these discharges as the current profile evolves, the most common types of MHD activity reported are toroidicity-induced AEs (TAE) and reversed-shear AEs (RSAE). Figure 3.6a shows the signal from an external magnetic probe during the current-ramp phase of a discharge with strong AE activity where large beam ion losses are observed. Neutral-beam injection starts at t=300ms concurrent with the appearance of multiple mode activity, evidenced by the spectral crosspower of two external magnetic probes (figure 3.6b). Two main types of AEs are observed; TAEs are

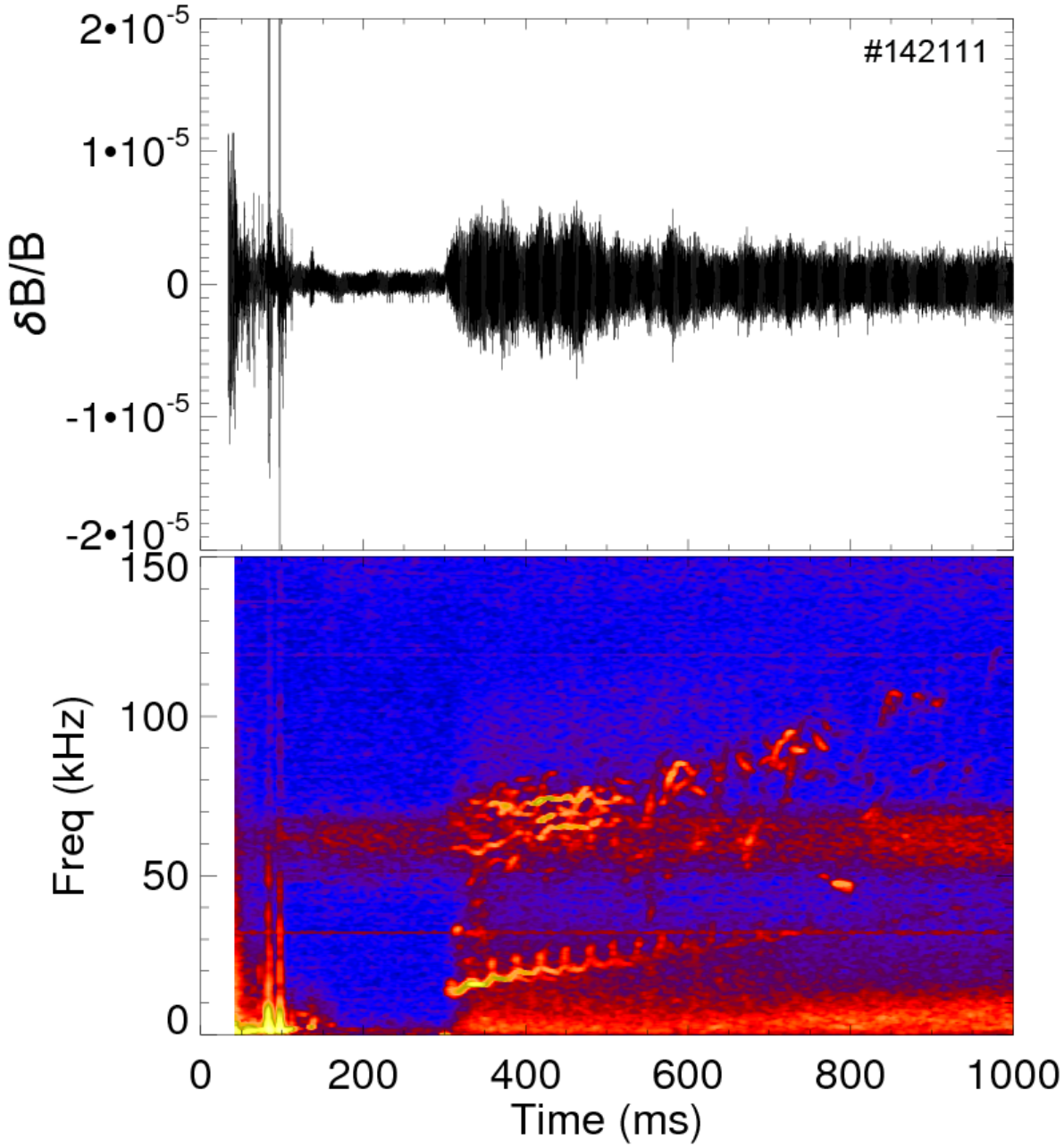

Figure 3.6.

identified as having relatively temporally constant frequency evolution while RSAEs have the characteristic of chirping frequency spectra. In this discharge, the AEs are observed at frequencies mainly above 50kHz; the lower frequency mode evolving from about 10kHz up to about 30kHz is a n=0 energetic particle-induced geodesic acoustic mode (EGAM) [59] and is not

associated with AE activity. However, EGAMs are observed to cause coherent beam-ion losses [60], a topic which will be discussed in future publications.

During strong TAE and RSAE activity, the neutron rate is suppressed up to 50% compared to classical predictions, implying strong transport of beam ions [40]. High-bandwidth fast-ion loss measurements indicate losses coherent with AE fluctuations. Analysis of pitch- and energy-resolved fast-ion loss measurements show that the losses are from nearly full-energy (~75keV) beam ions with pitch ($v_{||}/v$) about 0.7 [60]. Mode-induced loss of beam particles results from resonances with the modes, kicking particles into loss boundaries. Unlike fishbones and sawteeth, there are no general simplifications to eqs. (3.1) & (3.2) for AEs, since multiple-n modes exist at frequencies high compared to kink-like instabilities. Therefore, losses can be associated with a multitude of higher-order mode-particle resonances. Figure 3.7 represents a typical zoology of resonance curves in velocity space due to a single mode (n=2, f=70kHz at t=448ms) at the approximate radial location of the peak of its amplitude (ρ=0.3 where ρ is the square root of the normalized toroidal flux). While resonant losses of all classes of particles may be possible, the losses observed are likely due to counter-passing fast ions. We can see why from figure 3.7. Numerous resonances converge near the counter-passing/lost-particle boundary. Ions can undergo a change in their energy and canonical toroidal momentum when interacting resonantly with a mode. The magnitude of the change depends on the amplitude of the mode, and for small amplitude perturbations such as AEs, a single resonant interaction minimally changes the particle's constants of motion. However, a fast ion in a region of velocity space with closely spaced resonances can interact with the mode multiple times leading to a significant modification to its orbit.

Simulations of the DIII-D data confirm that the AE and particle undergo multiple

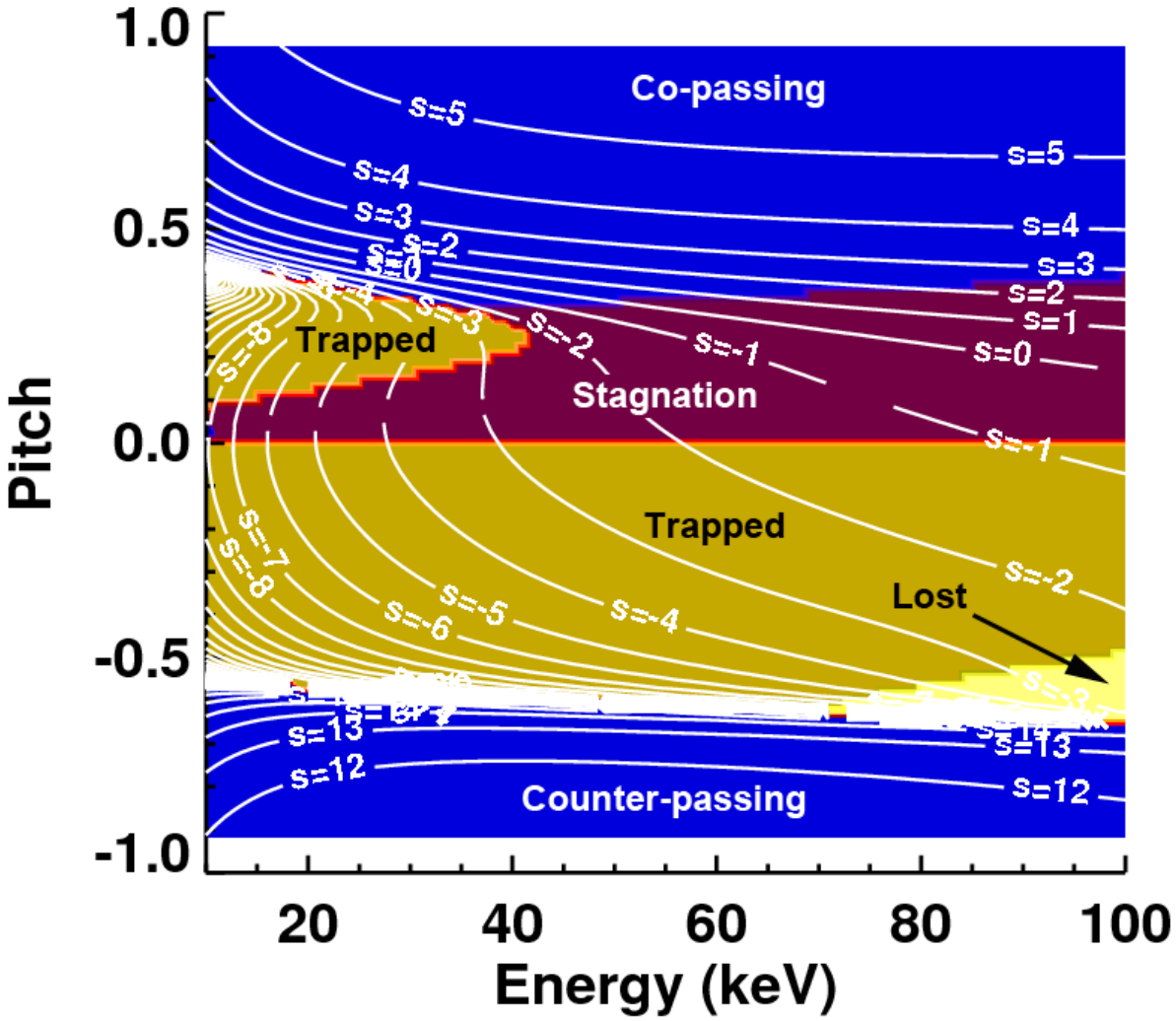

Figure 3.7.

interactions, reducing the canonical toroidal momentum of counter-passing ions, leading consequently to a reduction in $v_{||}$, and transforming them to lost trapped ions. The simulations model the observed losses and reproduce the pitch and energy distribution of lost beam ions. The simulation procedure involves several steps. First the linear eigenfunctions are calculated by the ideal MHD solver NOVA [61] [62] from supplied EFIT equilibrium and plasma profile data. The eigenfunctions are fit to those measured by the electron cyclotron emission (ECE) diagnostic [37] [63] and assigned amplitudes corresponding to the measured values. The Hamiltonian

guiding-center code ORBIT [64] is used to follow the particle distribution through the equilibrium fields perturbed by the NOVA-supplied wave fields. Particle orbits crossing the last-closed flux surface are traced by a second guiding-center code employing the constants of motion [40]. Particles that strike the position of the FILD detector are recorded. The simulation accurately predicts the energy distribution of lost fast ions and models the pitch angle distribution within 10% of the measurement. The interested reader is referred to references [60] and [40] for further details regarding DIII-D's measurements of fast-ion losses induced by Alfvén eigenmodes.

Section 3.4. Summary

Mode-particle resonances play a key role in many transport phenomena observed in magnetic confinement systems. Resonance occurs when the phase between the electromagnetic wave and a particle's periodic orbital motion remains constant. When this occurs, energy is exchanged between the particle and the wave, and a change in a particle's energy leads to radial excursions. Characteristics of the mode (such as its radial extent, mode numbers, and amplitude) determine which particles interact with the wave and the intensity of the interaction. We saw that low-n low-frequency modes (e.g. sawteeth and fishbones) interact with fast-ion velocity space through very few resonances, while higher-n higher-frequency modes (e.g. Alfvén eigenmodes) can possess a multitude of resonances. Although these instabilities represent opposite ends of the frequency spectrum, significant modifications to the fast-ion distribution function ensue. The magnitude of particle transport (whether it is convective or diffusive) depends on the mode amplitude. For large-amplitude modes, a single interaction between the mode and a particle can lead to large orbit perturbations, while smaller-amplitude modes are less effective at driving transport. The kink-like instabilities with their large amplitude magnetic perturbations can

strongly perturb orbits via single resonances, while the small amplitude AEs are effective at driving transport through a series of multiple resonances [65]. The subject of mode-particle resonances in magnetic confinement devices is a rich research area, one that requires collaborative efforts between experiment and theory, with the ultimate goal of predictive transport models for future reactors.

POSTFACE

Fast-ion measurements (e.g. FIDA) in magnetic confinement devices are essential for diagnosing the dynamic properties of the superthermal population. The FIDA suite on DIII-D, as of 2012, consists of 4 installations which are capable of resolving different fast-ion orbits. When employed together, data from the 4 systems provide full coverage of the relevant portions of velocity space, making it possible to construct a reasonably comprehensive description of the energetic deuterium population. One drawback is that the spectrometers of the vertical system are shared with the CER diagnostic which measures the plasma poloidal rotation, and this is the default configuration on all experiments unless otherwise specified. Future experiments would greatly benefit from an additional dedicated vertical FIDA system (fibers and spectrometer) that would make measurements on all shots without sacrificing the poloidal rotation measurement.

One lesson learned during the implementation of the oblique system is that, while multiple collection fibers per radial channel do increase the signal-to-noise level, only the highest Doppler-shift spectral regions benefit the greatest. It might be thought that increasing the number of collection fibers per radial channel would correspondingly reduce the random error by the same factor. However, random errors measured by FIDA do not directly scale inversely with the number of fibers; random errors measured by the vertical system (consisting of 1 fiber per radial channel and a typical random error of ~20% in quiet plasmas) compared to those measured by the oblique system (consisting of 3 fibers per radial channel and a typical random error of ~10%) do not directly scale with the number of fibers. Therefore, the investment in multi-fiber radial channels is only practical for a system in which high Doppler shifts (beam injection energy or

higher) are of interest. Unless ICRF is planned as a routine heating scheme or the injection voltage of the neutral beams is increased above 80keV, single-fiber channels for future systems are likely sufficient.

An outstanding issue with FIDA that remains to be unresolved since its 1st generation predecessor is the discrepancy between the absolute radiance measured and predicted by FIDAsim. While the spectral shapes are in excellent agreement (suggesting the distribution function is being accurately modeled), the magnitude of the photon flux predicted by the synthetic diagnostic almost always over-estimates the measurement (by as much as a factor of 2). The highly suspected culprit is mischaracterization of the diagnostic neutral beams (210R for the oblique system and 330L for the vertical system); the injection geometry for these beams are mainly taken from design values and rough calorimetry measurements. Imaging of the 30L beam has made it possible to adjust its injection geometry in codes such as TRANSP and FIDAsim for more accurate modeling. Incidentally, FIDA data from the main ion CER system which views the 30L beam yields quite accurate agreement with FIDAsim in quiet plasmas. On the other hand, FIDA data from the main ion CER system which views the 210R beam and predictions from FIDAsim are discrepant even in quiet plasmas. It should be a priority of the DIII-D program to have accurate measurements of all of the neutral beams since many simulation codes and diagnostics depend on them.

The implementation of the main ion CER system emphasizes the necessity to monitor simultaneously the beam emission spectrum (BES) with FIDA. Described in chapter 1, the BES provides a wealth of information on the injected neutral population. Since the interpretation of the FIDA signal depends so strongly on the injected neutral population, a thorough measurement should include both FIDA and BES components. Previous installations avoided the bright cold

Dα and BES components because detector saturation was an issue; with the availability of higher-bit cameras, the entire Dα spectrum can be monitored with sufficient signal-to-noise even in the FIDA wings.

We saw in chapter 3 that mode-particle resonances can cause significant modifications to the fast-ion distribution function. The sawtooth instability, conventionally thought to redistribute particles by flux-attachment to the evolving mode, can theoretically interact with highly energetic particles through bounce-precessional resonances as well. Fast-ion data from DIII-D during sawteeth are consistent with the idea that above the threshold energy for flux-attachment, mode-particle resonances can strongly redistribute particles. Because the findings are incidental and the experiment from which the data is extracted was not designed to study mode-particle resonances, the conditions are not optimized for such an investigation. In the shot studied, during the injection of the fast wave, as a precaution to retain the plasma in L-mode, the NBI modulation duty cycle is decreased, effectively reducing the number of injected sources to 1/3. Because of this, the population of beam ions is low, which reduces the number of ions that couple to the ICRF resonance. Consequently, the signal-to-noise level of FIDA is low, especially at large Doppler shifts. Furthermore, the experiment was performed during the 2010 experimental campaign before the midplane fast-ion loss detector (FILD) was installed. FILD resolves fast-ion losses in pitch and energy, so such a diagnostic would greatly aid our understanding of the observed losses from the Faraday cup detector. In a future experiment, it is advisable to arrange the duty cycles of the diagnostic neutral beams so that the injected power remains relatively constant during the injection of the fast wave; this alone would greatly improve the signal-to-noise levels from FIDA. A future experiment on DIII-D that would attempt to reinvestigate mode-particle resonances between ICRF-accelerated beam ions and the sawtooth

instability would also provide the added benefit of more shots with high-harmonic ICRF heating. Theoretical and experimental collaborations have been underway for many years to try and understand the peculiarities about fast-wave coupling to beam ions, such as the role of finite-orbit width and synergistic effects of multiple high-harmonic resonances (e.g. 4^{th}+6^{th} harmonics). Code development has come a long way in the past few years, and new diagnostic capabilities make it a better time than ever to reconcile the discrepancies observed in plasmas heated by ICRF.

The investigation of mode-particle resonances should be extended to realms outside of the relatively well-studied regime of L-mode plasmas. Future reactor-relevant machines will operate in the H-mode regime and will be susceptible to tearing modes that could be deleterious to plasma confinement. Low-n tearing modes (e.g. the 2/1 and 3/2 modes) are particularly harmful as they can evolve into locked modes and eventually disrupt. Even quasi-stable tearing modes that do not mode convert into more detrimental ones can cause problems. Because of their potentially large mode amplitudes and radially-extended mode structure, low-n tearing modes can enhance fast-ion transport through resonant interactions. Through the creation of orbital sidebands, tearing modes can distort the otherwise peaked spatial distribution of energetic particles, reducing the heating efficiency and fusion reactivity.

Controlled nuclear fusion by way of magnetic confinement is one of the most promising concepts for future generation electrical power plants. The first tokamak developed in the 1950s has evolved a long way to its present-day form, gaining international acclaim among many nations. Since its conception, the tokamak has been challenged with numerous experimental and theoretical obstacles. Despite these setbacks, tokamak research is flourishing, and the efforts of innumerable scientists and engineers will come to fruition with the construction of ITER. ITER

is planned to be the ultimate experimental tokamak, after which DEMO is envisaged to supply power to the grid. There are still many outstanding scientific and engineering issues related to tokamaks, and this thesis attempts to tackle just a few of them, namely measurements of the superthermal ion population and instabilities that affect their confinement.

REFERENCES

[1] J. A. Wesson, Tokamaks, Oxford University Press, 2011.

[2] I. Hutchinson, Principles of Plasma Diagnostics, Cambridge University Press, 2002.

[3] W. W. Heidbrink, K. H. Burrell, Y. Luo, N. A. Pablant, and E. Ruskov, Plasma Physics and Controlled Fusion 46 (2004) 1855.

[4] Y. Luo, W. W. Heidbrink, K. H. Burrell, E. Ruskov, and W. M. Solomon, Physics of Plasmas 14 (2007) 112503.

[5] Y. Luo, W. W. Heidbrink, K. H. Burrell, D. H. Kaplan, and P. Gohil, Review of Scientific Instruments 78 (2007) 033505.

[6] W. W. Heidbrink, Review of Scientific Instruments 81 (2010) 10D727.

[7] A. Pankin, D. McCune, R. Andre, G. Bateman, and A. Kritz, Computer Physics Communications 159 (2004) 157-184.

[8] J. Ongena, M. Evrard, and D. McCune, Transactions of Fusion Technology 33 (1998) 181-191.

[9] W. W. Heidbrink, Y. Luo, K. H. Burrell, R. W. Harvey, R. I. Pinsker, and E. Ruskov, Plasma Physics and Controlled Fusion 49 (2007) 1457.

[10] M. Salewski, S. Nielsen, H. Bindslev, V. Furtula, N. N. Gorelenkov, S. Korsholm, F.

Leipold, F. Meo, P. Michelsen, D. Moseev, and M. Stejner, Nuclear Fusion 51 (2011) 083014.

[11] K. H. Burrell, D. H. Kaplan, P. Gohil, D. G. Nilson, R. J. Groebner, and D. M. Thomas, Review of Scientific Instruments 72 (2001) 1028.

[12] M. A. Van Zeeland, J. H. Yu, W. W. Heidbrink, N. H. Brooks, K. H. Burrell, M. S. Chu, A. W. Hyatt, C. Muscatello, R. Nazikian, N. A. Pablant, and others, Nuclear Fusion 50 (2010) 084002.

[13] W. W. Heidbrink, Y. Luo, C. M. Muscatello, Y. Zhu, and K. H. Burrell, Rev Sci Instrum 79 (2008) 10E520.

[14] M. Podesta, Review of Scientific Instruments 79 (2009) 10E521.

[15] Y. Luo, in Physics and Astronomy, University of California-Irvine, Irvine, 2007.

[16] Kaiser Optical Systems, Inc., Ann Arbor, MI, http://www.kosi.com.

[17] Newport Corporation, Irvine, CA, http://www.newport.com.

[18] R. E. Bell, Review of scientific instruments 75 (2004) 4158.

[19] Sarnoff Corporation, Princeton, NJ, http://www.sarnoff.com.

[20] Hamamatsu Photonics, Bridgewater, NJ, http://www.hamamatsu.com.

[21] W. W. Heidbrink, D. Liu, Y. Luo, E. Ruskov, and B. Geiger, Communications in Computational Physics 10 (2011) 716.

[22] Personal communication with B. A. Grierson, San Diego, CA, 2012.

[23] B. A. Grierson, K. Burrell, W. W. Heidbrink, M. J. Lanctot, N. A. Pablant, and W. M. Solomon, Phys Plasmas (2012).

[24] S. von Goeler, W. Stodiek, and N. Sauthoff, Phys. Rev. Lett. 33 (1974) 1201.

[25] B. B. Kadomtsev, Soviet Journal of Plasma Physics 1 (1975) 389.

[26] F. B. Marcus, J. M. Adams, A. D. Cheetham, S. Conroy, W. Core, O. N. Jarvis, M. J. Loughlin, M. Olsson, G. Sadler, P. Smeulders, and others, Plasma Physics and Controlled Fusion 33 (1991) 277.

[27] S. J. Zweben, Nuclear fusion 29 (1989) 825.

[28] G. Martin, O. N. Jarvis, J. Kallne, V. Merlo, G. Sadler, and P. van Belle, Physica Scripta T16 (1987) 171.

[29] B. C. Stratton, R. J. Ponck, G. R. McKee, R. V. Budny, Z. Chang, F. Wising, and A. Ödblom, Nuclear Fusion 36 (1996) 1586.

[30] M. P. Petrov, R. V. Budny, H. H. Duong, R. K. Fisher, N. N. Gorelenkov, J. M. McChesney, D. K. Mansfield, S. S. Medley, P. B. Parks, M. H. Redi, and others, Nuclear Fusion 35 (1995) 1437.

[31] M. P. Petrov, N. N. Gorelenkov, R. V. Budny, Z. Chang, D. D. S., H. H. Duong, R. K. Fisher, R. J. Fonck, H. W. Herrmann, G. R. McKee, S. S. Medley, A. Odblom, A. L. Roquemore, B. C. Stratton, F. Wising, R. B. White, and Y. Zhao, in IAEA Fusion Energy Conference, 1996.

[32] S. Nielsen, H. Bindslev, M. Salewski, A. Burger, E. Delabie, V. Furtula, M. Kantor, S. Korsholm, F. Leipold, F. Meo, P. Michelsen, D. Moseev, J. Oosterbeek, M. Stejner, E. Westerhof, and P. Woskov, Plasma Physics Controlled Fusion 52 (2010) 092001.

[33] Y. I. Kolesnichenko and Y. V. Yakovenko, Nuclear Fusion 36 (1996) 159.

[34] J. L. Luxon, Nuclear fusion 42 (2002) 614.

[35] L. L. Lao, H. St John, R. D. Stambaugh, A. G. Kellman, and W. Pfeiffer, Nuclear Fusion 25 (1985) 1611.

[36] B. W. Rice, K. H. Burrell, L. L. Lao, and Y. R. Lin-Liu, Physical Review Letters 79 (1997) 2694-2697.

[37] M. E. Austin and J. Lohr, Review of scientific instruments 74 (2003) 1457.

[38] W. W. Heidbrink, P. L. Taylor, and J. A. Phillips, Review of scientific instruments 68 (1997) 536-539.

[39] E. J. Strait, Rev. Sci. Instrum. 77 (2006) 023502.

[40] M. A. Van Zeeland, W. W. Heidbrink, R. K. Fisher, M. G. Mu noz, G. J. Kramer, D. C. Pace, R. B. White, S. Aekaeslompolo, M. E. Austin, J. E. Boom, and others, Physics of Plasmas 18 (2011) 056114.

[41] Y. I. Kolesnichenko, V. V. Lutsenko, Y. V. Yakovenko, and G. Kamelander, Physics of Plasmas 4 (1997) 2544.

[42] O. N. Jarvis, J. M. Adams, P. Howarth, F. B. Marcus, E. Righi, G. J. Sadler, D. Start, P.

V. Belle, C. D. Warrick, and N. Watkins, Nuclear fusion 36 (1996) 1513.

[43] Y. I. Kolesnichenko, V. V. Lutsenko, K. White, and Y. V. Yakovenko, Nucl. Fusion 40 (2000) 1325.

[44] R. B. White, The theory of toroidally confined plasmas, Imperial College Pr, 2006.

[45] K. McGuire, R. Goldston, M. Bell, M. Bitter, K. Bol, K. Brau, D. Buchenauer, T. Crowley, S. Davis, F. Dylla, and others, Physical Review Letters 50 (1983) 891-895.

[46] L. Chen, R. B. White, and M. N. Rosenbluth, Physical review letters 52 (1984) 1122-1125.

[47] R. B. White, R. J. Goldston, K. McGuire, A. H. Boozer, D. A. Monticello, and W. Park, Physics of Fluids 26 (1983) 2958.

[48] Y. I. Kolesnichenko, V. V. Lutsenko, and Y. V. Yakovenko, Physics of Plasmas 5 (1998) 729-734.

[49] Y. I. Kolesnichenko, V. V. Lutsenko, R. B. White, and Y. V. Yakovenko, Physics of Plasmas 5 (1998) 2963.

[50] L. D. Pickering, W. W. Heidbrink, and Y. Zhu, in American Physical Society Division of Plasma Physics, 2006.

[51] E. A. Lazarus, T. C. Luce, M. E. Austin, D. P. Brennan, K. H. Burrell, M. S. Chu, J. R. Ferron, A. W. Hyatt, R. J. Jayakumar, L. L. Lao, and others, Physics of plasmas 14 (2007) 055701.

[52] R. W. Harvey and M. G. McCoy, in IAEA TCM on Advances in Sim. and Modeling of Thermonuclear Plasmas, 1992, p. 527.

[53] A. P. Smirnov, R. W. Harvey, and K. Kupfer, Bull Amer. Phys. Soc. 39 (1994) 1626.

[54] M. Okabayashi, I. N. Bogatu, M. S. Chance, M. S. Chu, A. M. Garofalo, Y. In, G. L. Jackson, R. J. La Haye, M. J. Lanctot, J. Manickam, and others, Nuclear Fusion 49 (2009) 125003.

[55] M. Okabayashi, G. Matsunaga, W. W. Heidbrink, Y. In, Y. Q. Liu, H. Reimerdes, W. M. Solomon, E. J. Strait, M. Takechi, N. Asakura, and others, Physics of Plasmas 18 (2011) 056112.

[56] W. W. Heidbrink, M. E. Austin, R. K. Fisher, M. Garcia-Munoz, G. Matsunaga, G. R. McKee, R. A. Moyer, C. M. Muscatello, M. Okabayashi, D. C. Pace, K. Shinohara, W. M. Solomon, E. J. Strait, M. A. Van Zeeland, and Y. Zhu, Plasma Physics Controlled Fusion 53 (2011) 085028.

[57] R. J. Fonck, P. A. Duperrex, and S. F. Paul, Review of scientific instruments 61 (1990) 3487-3495.

[58] G. McKee, R. Ashley, R. Durst, R. Fonck, M. Jakubowski, K. Tritz, K. Burrell, C. Greenfield, and J. Robinson, Review of scientific instruments 70 (1999) 913.

[59] R. Nazikian, G. Y. Fu, M. E. Austin, H. L. Berk, R. V. Budny, N. N. Gorelenkov, W. W. Heidbrink, C. T. Holcomb, G. J. Kramer, G. R. McKee, and others, Physical review letters 101 (2008) 185001.

[60] D. C. Pace, R. K. Fisher, M. Garca-Mu noz, W. W. Heidbrink, and M. A. Van Zeeland, Plasma Physics and Controlled Fusion 53 (2011) 062001.

[61] C. Z. Cheng and M. S. Chance, J Comput Phys 71 (1987) 124.

[62] C. Z. Cheng, Phys Rep 211 (1992) 1.

[63] B. Tobias, C. Domier, T. Liang, X. Kong, L. Yu, G. Yun, H. Park, G. Classen, J. E. Boom, A. Donne, T. Munsat, R. Nazikian, M. A. Van Zeeland, R. L. Boivin, and N. Luhmann, Rev Sci Instrum 81 (2010) 10D928.

[64] R. B. White and M. S. Chance, Physics of Fluids 27 (1984) 2455.

[65] R. B. White, N. N. Gorelenkov, W. W. Heidbrink, and M. A. Van Zeeland, Phys Plasmas 17 (2010) 056107.

APPENDIX A. Radiometric calibrations of FIDA on DIII-D

For a direct comparison between measured and predicted light levels, one must compare signals with the same units. Our main FIDA measurement involves exposing light to a CCD chip, and the light intensity at each pixel is measured as an integer value of counts. For our 12-bit Sarnoff camera, there are $2^{12} = 4096$ possible recordable intensity levels. It is possible to associate CCD counts to a physical quantity that describes the amount of light it measures. For this, we perform a radiometric calibration with an integrating light sphere. The light sphere emits a known photon flux, so during the calibration, the recorded number of CCD counts can be associated with the photon flux to yield a calibration factor. The calibration factor is then later used during the analysis of the experimental data to convert CCD counts into a spectral radiance value.

First, there are some peculiarities about the s-FIDA system that must be considered during the calibration process. The optical fibers on the tokamak end of the system are stationary and never moved. However, as described in section I.4., the fibers are mounted to a patch panel in the diagnostic lab allowing a user to swap the placement of the radial channels on the CCD chip. The CCD accommodates 6 out of the 11 possible channels during a single shot. If the full profile is desired, the user must rearrange the patch panel for a subsequent shot to acquire data from the remaining channels. Changing the patch panel configuration changes the pairs of fibers through which the light travels to reach the CCD. Realistically, the fibers do not have identical attenuation, especially over many meters. Therefore, one must consider this caveat during the intensity calibration, so standardized patch panel configurations were designed for consistency between experiments and radiometric calibrations.

Because of the large spot sizes relative to the aperture of the light sphere, one fiber chord is calibrated at a time. Since 3 fibers comprise a radial channel, 3 independent calibrations must be performed for each channel. The calibration is prepared by backlighting the fiber in the diagnostic lab and locating its chord inside the tokamak vacuum chamber. The light sphere is set up in the tokamak and is arranged so the backlit chord shines through the aperture into the cavity of the light sphere. Once the chord and light sphere are aligned, the calibration shot is acquired. The radiance spectrum emitted by the light sphere is valid only for a particular supplied current to the sphere and for a particular integrated luminosity emitted by the sphere. Any value of the current other than the calibrated value specified by the manufacturer voids the calibrated radiance spectrum. Even modest modifications to the current change the color temperature and wavelength dependence of the spectral output. Changes to the luminosity are more forgiving; sometimes the CCD can become saturated, so the luminosity emitted by the light sphere must be lowered. The wavelength dependence of the spectral output is much weaker on the luminosity, even up to a factor of ~2. If the luminance on the light sphere is changed within a factor of ~2, the amplitude of the radiance spectrum can be scaled proportionally. Finally, after calibrating each patch panel configuration, a dark spectrum is taken with the light sphere turned off.

Processing the calibration data for a single radial channel:

The dark spectrum (D) is subtracted from the raw spectrum (R_i) of each of the 3 chords to yield the net spectrum (S_i) of the light emitted by the sphere measured by FIDA,

$$S_i \{\text{counts/ms}\} = R_i - D \qquad \text{(A.1)}$$

For s-FIDA, the data integration time is 1ms, so S_i has units of counts/ms. The subscript i denotes the chord index (where 3 toroidally-displaced chords comprise a radial channel). To obtain the calibration spectrum used to convert counts/ms to a photon flux, first the known spectral radiance from the light sphere (P) is adjusted according to the actual luminance value (L_i) used during the calibration. We scale P by L_i/L_0 where L_0 is the luminance at which P was obtained by the manufacturer. The product $L_i/L_0 \times P$ is then the radiance spectrum at the luminance value used in-vessel. For s-FIDA during typically usage, the spectra from the 3 radial chords are binned on the CCD to yield a single spectrum for that particular radial channel. This amounts to a summation of the spectra from the 3 chords. The total calibration spectrum for a radial channel is then also the summation over the 3 chords. To determined the calibration spectrum (C) for a radial channel, the sum of S_i over the 3 chords is divided by the sum of $L_i/L_0 \times P$ over the 3 chords to yield CCD counts per photon flux,

$$C\ \{\text{counts / photons/cm}^2\text{-nm-sr}\} = \Sigma S_i\ \{\text{counts/ms}\} \times 1000\text{ms/1s} \,/\, \Sigma\,(L_i/L_0 \times P\ \{\text{photons/cm}^2\text{-s-nm-sr}\}) \quad (A.2)$$

To apply the calibration to an experimental spectrum for direct comparison with a spectrum from FIDAsim, we simply divide the raw experimental spectrum (F_{raw}) by C and integrate over the 4π steradians of the light sphere,

$$F_{calibrated}\ \{photons/cm^2\text{-}s\text{-}nm\} =$$

$$4\pi \times F_{raw}\ \{counts/ms\} / C\ \{counts / photons/cm^2\text{-}nm\text{-}sr\} \times 1000ms/1s \qquad (A.3)$$

APPENDIX B. Sample f-FIDA data

Demonstration of the f-FIDA system is presented in figure B.1 showing sample data from an H-mode discharge with Ip ~0.8MA, Bt ~2T, and n_e ranging from $4\text{-}6\times10^{13}cm^{-3}$. The experiment required ~15MW of neutral beam power to strike low toroidal mode number neoclassical tearing modes (NTMs). Figure B.1a is a spectrogram of the crosspower between two magnetic probes separated toroidally by 33º. During this time window, presumably a 3/2 NTM persists until ~3.2s when it becomes dominantly a 2/1 mode. Figure B.1b is a spectrogram of the autopower of an active f-FIDA signal from ρ=0.15. There is an obvious coherence in the signal, following the same frequency evolution as the dominant mode; the passive view at the equivalent ρ lacks this feature. Evidently, fast ions interact coherently with the rotating island.

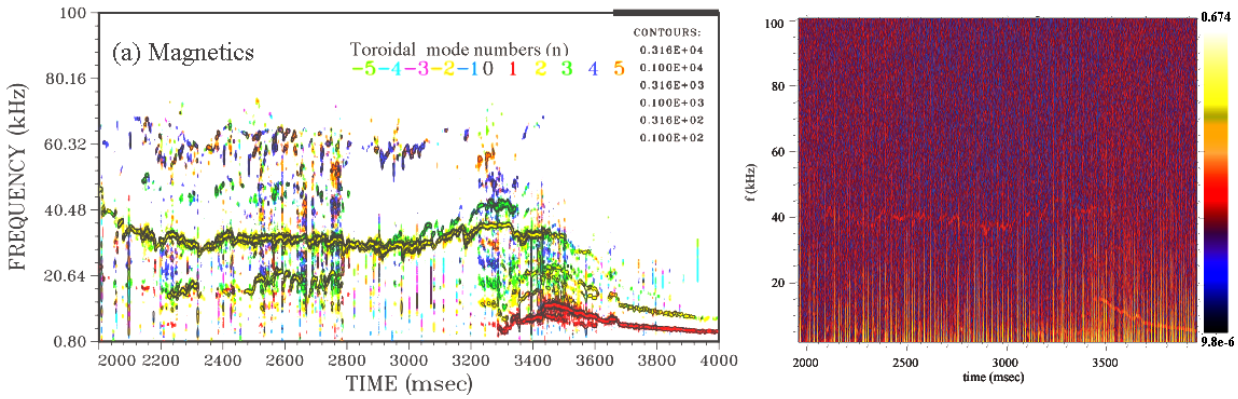

Figure B.1.

APPENDIX C. Sawtooth database

The database mentioned in chapter 2 is compiled for 30+ sawtoothing discharges on DIII-D in which neutral-beam injection was employed to generate the fast-ion population. Several of the discharges in question also included electron-cyclotron heating (ECH) and ion-cyclotron heating (ICH). In the discharges where ECH or ICH was launched at the tail-end of the discharge, only times prior to the wave heating were used. In discharges where ECH or ICH was launched at the beginning of the discharge, the shot was discarded. For the highest quality FIDA data, H-mode shots are discarded due to contaminating scattered Dα light from ELMs. Therefore, all discharges in the database are L-mode plasmas. As described in chapter 2, the fractional change of the FIDA signal at a sawtooth crash is calculated by conditional averaging over several uniform sawteeth (similar amplitudes and periods determined by ECE). Segments of each discharge in the database were hand-picked where the density, background Dα emission, and sawtooth feature were steady over at least 5 sawtooth cycles.

Values for Bt and Ip range between 1.86–2.05 T and 1.16–1.34 MA, respectively. Average sawtooth periods and amplitudes span 48–108 ms and 0.21–0.37, respectively. Central precrash values of Te and n_e range between ~2.0–5.0 keV and ~2.0–4.0×10^{19} m^{-3}, respectively. Shots in the database include circular, bean-shaped, oval, and "D"-shaped plasmas. Quantities that are loaded into the database include: neutral beam power and voltage, shape of the plasma, Bt, Ip, neutron rate, fractional change of core-most vertical and oblique FIDA signals, fractional change of core-most ECE signal (i.e. sawtooth amplitude), sawtooth period, average gradient of the Te profile inside q=1, q on axis (q_0), minimum q value (q_{min}), normalized

beta, poloidal beta, and mode amplitude (measured by external coils). Correlations amongst these quantities were sought and several examples are presented below. The correlation coefficient (r) is calculated for each case.

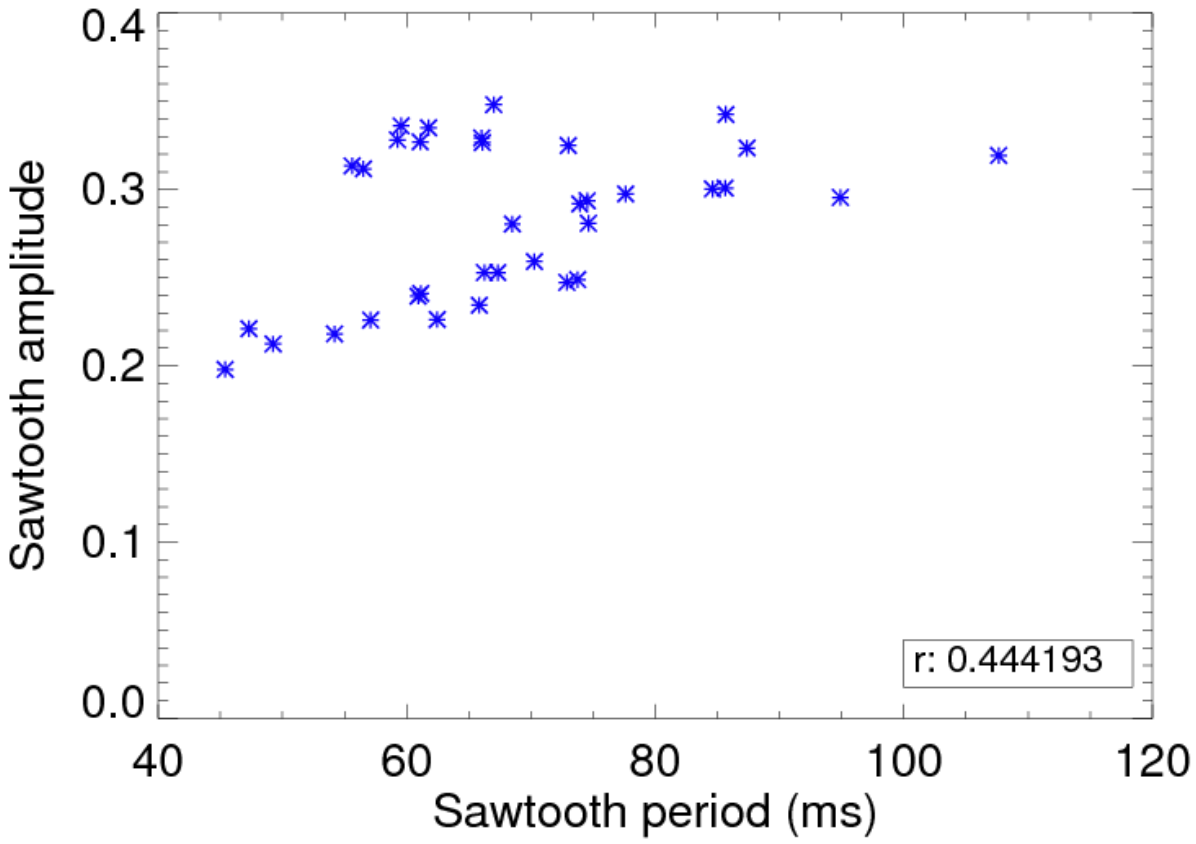

Figure C.1.

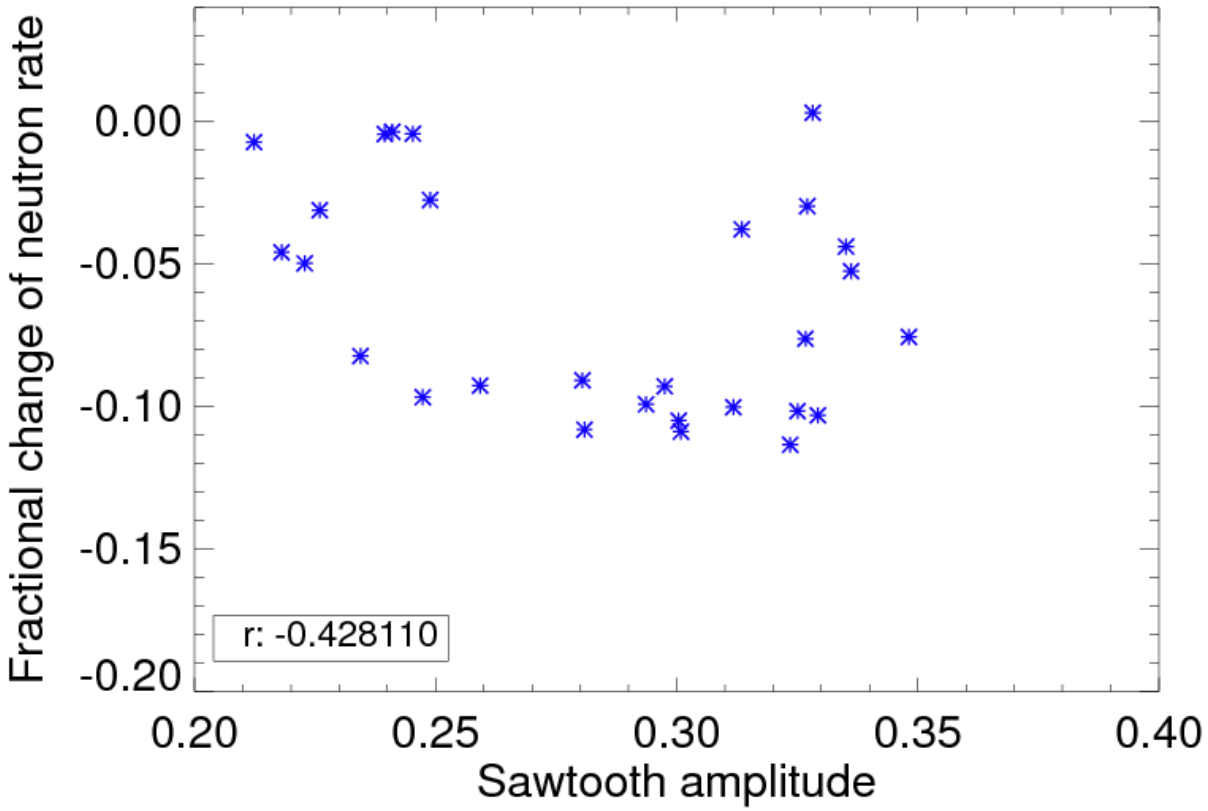
Fractional change of neutron rate
0.00
-0.05
-0.10
-0.15
-0.20
r: -0.428110
0.20
0.25
0.30
0.35
0.40
Sawtooth amplitude

Figure C.2.

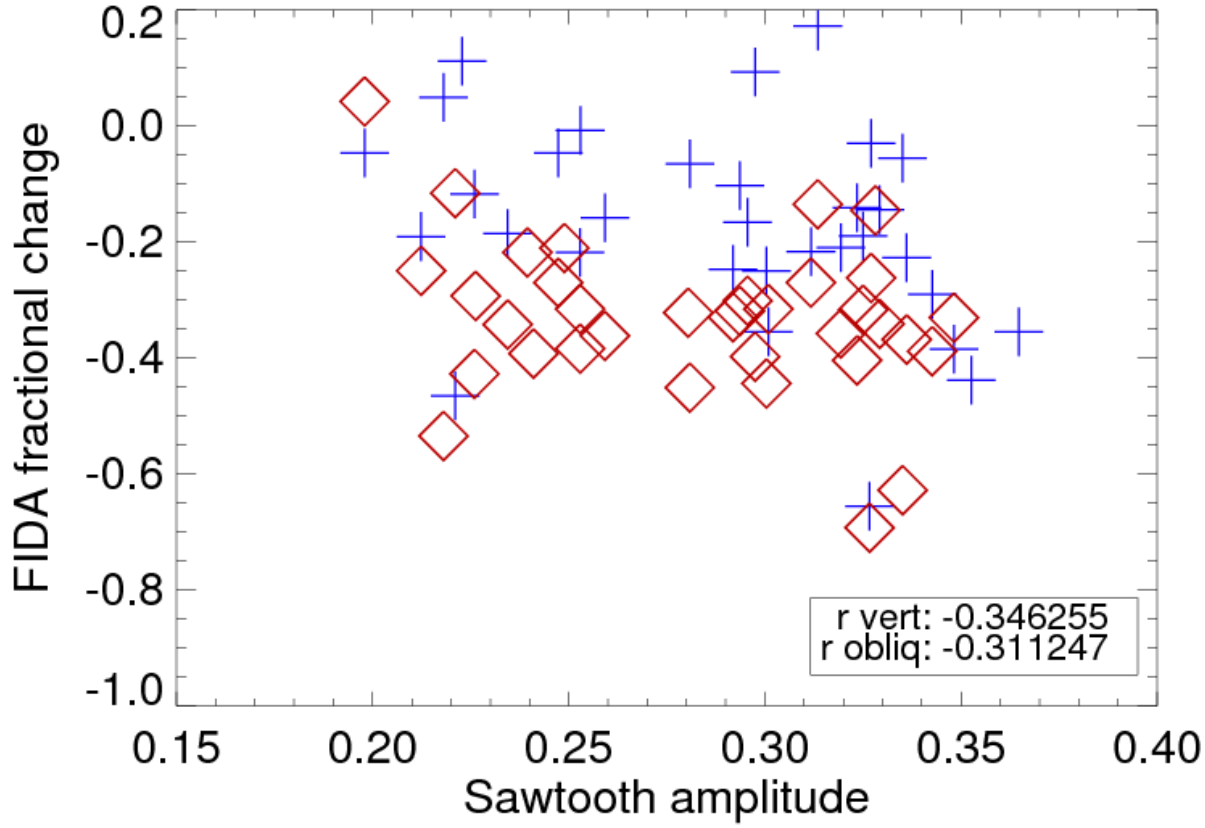
FIDA fractional change
Sawtooth amplitude
r vert: -0.346255
r obliq: -0.311247
0.2
0.0
-0.2
-0.4
-0.6
-0.8
-1.0
0.15
0.20
0.25
0.30
0.35
0.40

Figure C.3.

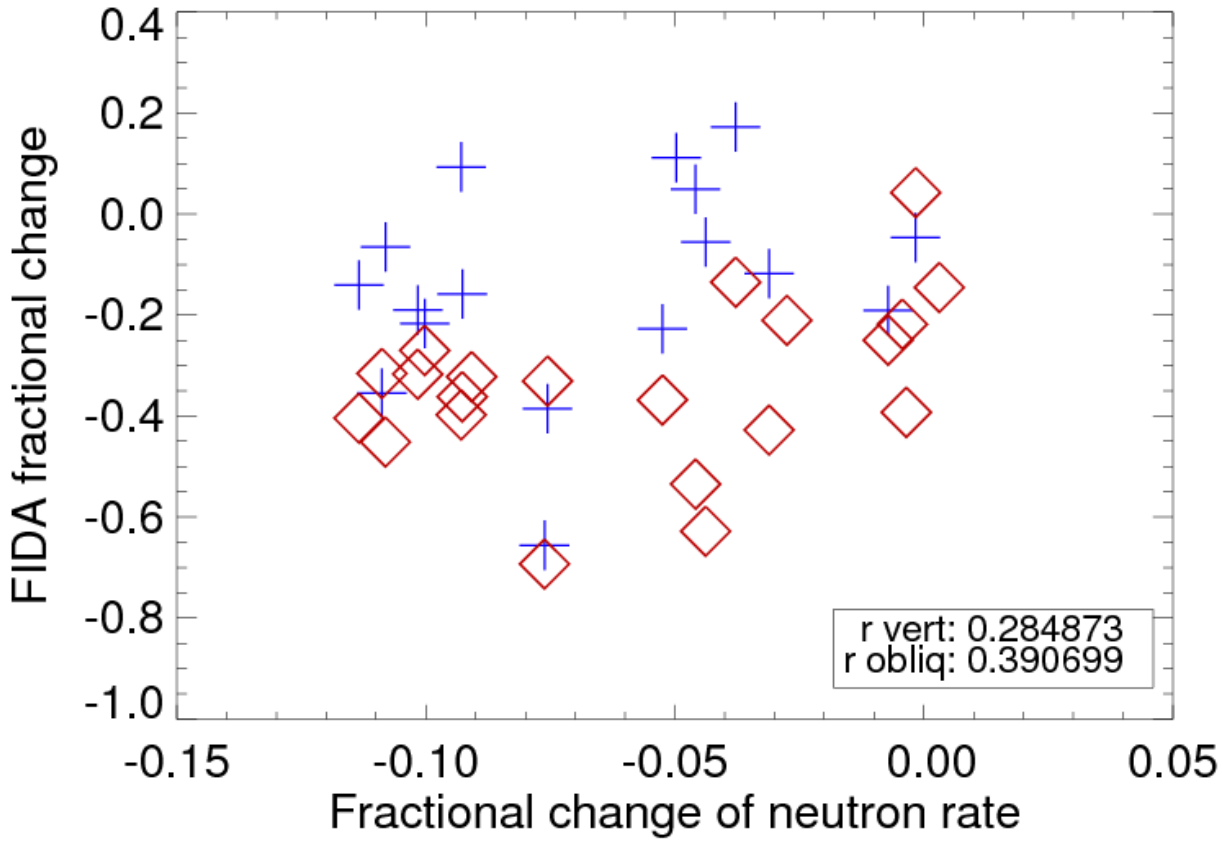
0.4
0.2
0.0
-0.2
-0.4
-0.6
-0.8
-1.0
FIDA fractional change
-0.15
-0.10
-0.05
0.00
0.05
Fractional change of neutron rate
r vert: 0.284873
r obliq: 0.390699

Figure C.4.

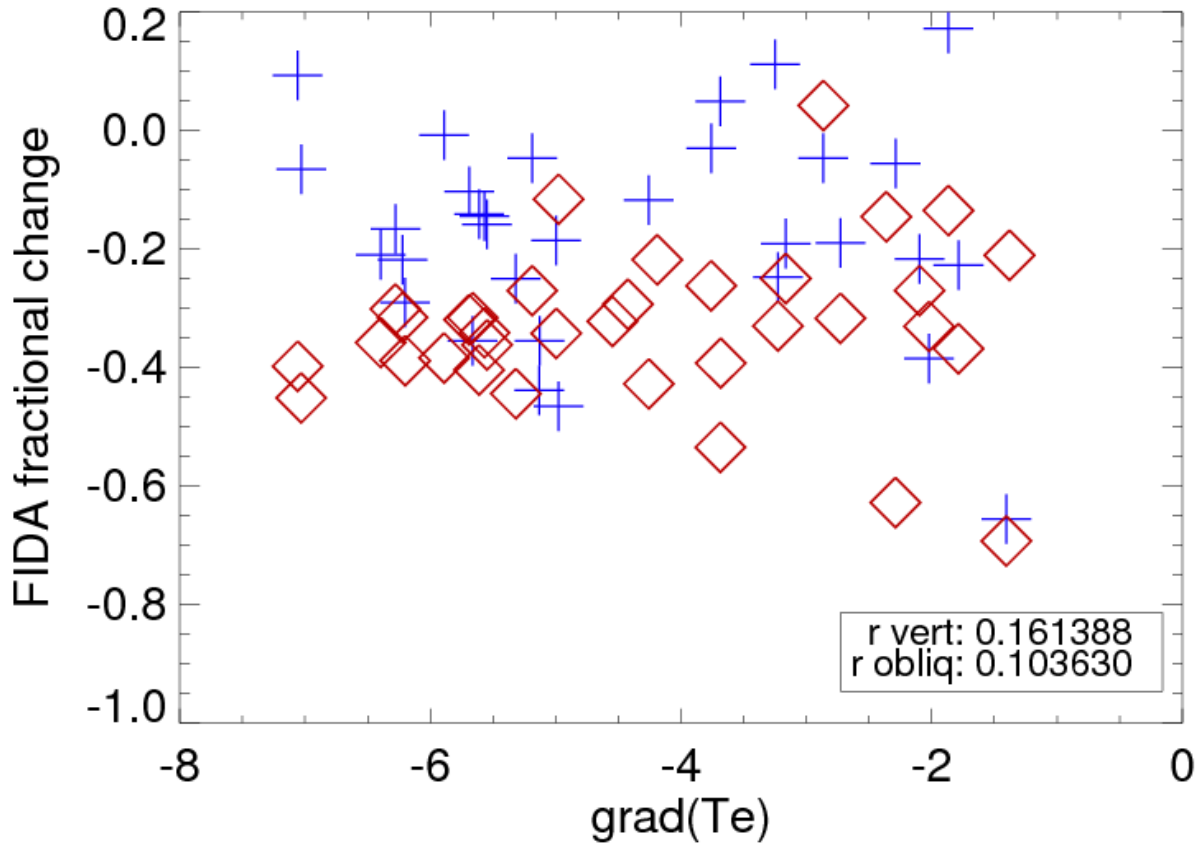
FIDA fractional change
0.2
0.0
-0.2
-0.4
-0.6
-0.8
-1.0
-8
-6
-4
-2
0
grad(Te)
r vert: 0.161388
r obliq: 0.103630

Figure C.5.

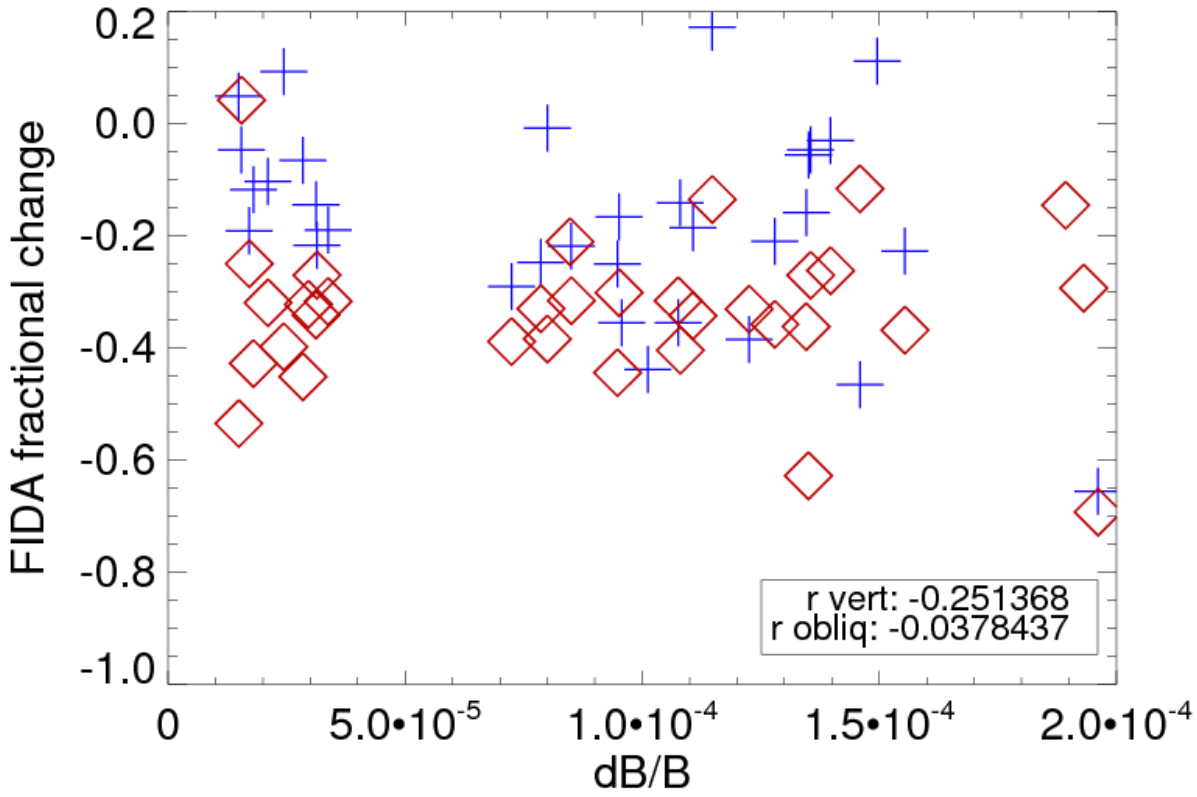
FIDA fractional change
0.2
0.0
-0.2
-0.4
-0.6
-0.8
-1.0
0
5.0•10-5
1.0•10-4
1.5•10-4
2.0•10-4
dB/B
r vert: -0.251368
r obliq: -0.0378437

Figure C.6.

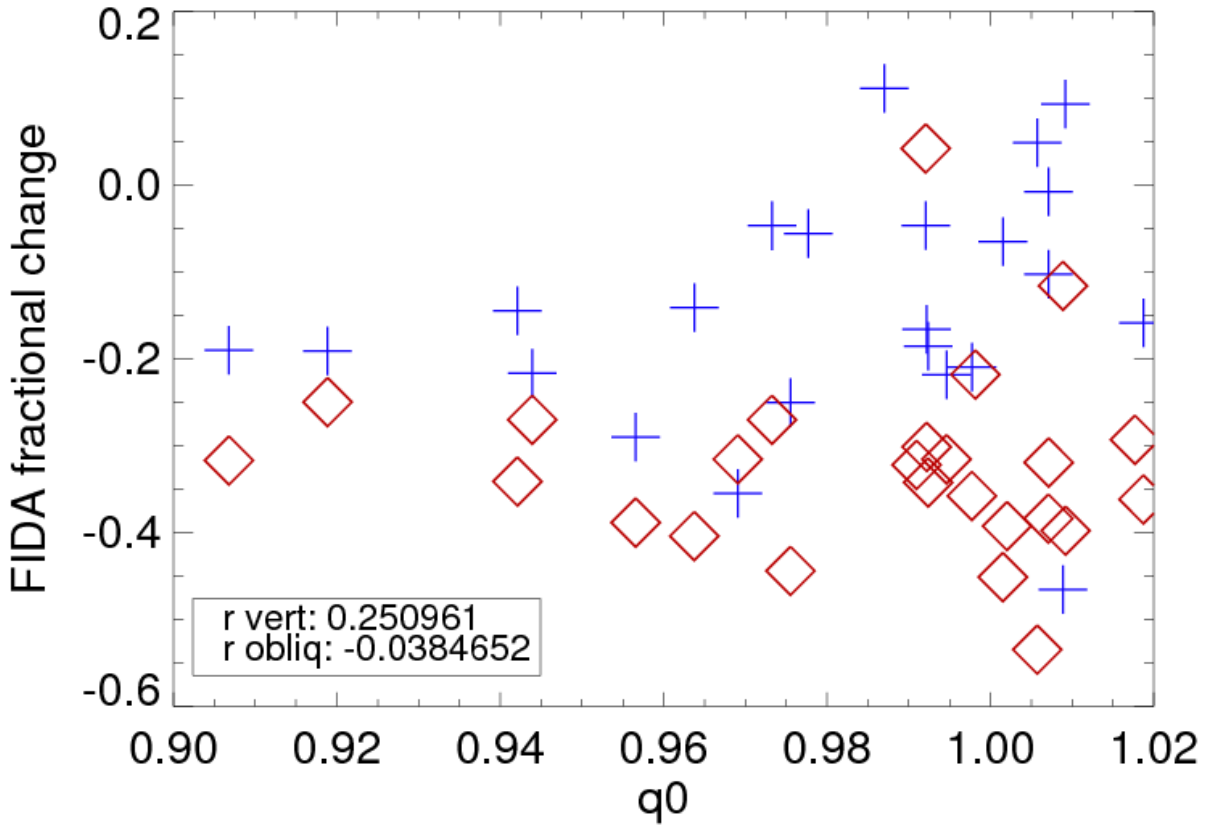
FIDA fractional change
0.2
0.0
-0.2
-0.4
-0.6
r vert: 0.250961
r obliq: -0.0384652
0.90
0.92
0.94
0.96
0.98
1.00
1.02
q0

Figure C.7.

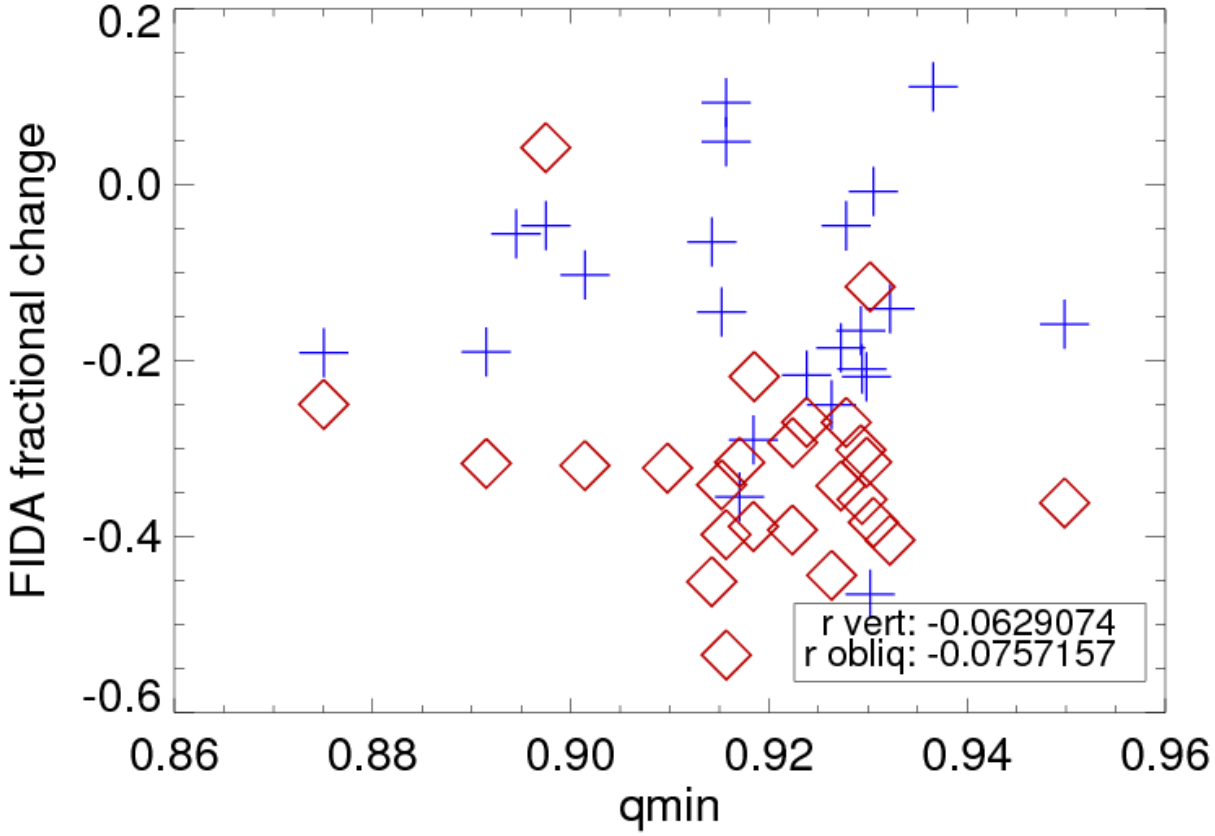
FIDA fractional change
0.2
0.0
-0.2
-0.4
-0.6
0.86
0.88
0.90
0.92
0.94
0.96
qmin
r vert: -0.0629074
r obliq: -0.0757157

Figure C.8.